Title	Electrochemical interface in fuel cell reactions
Author(s)	兒玉, 健作
Citation	北海道大学. 博士(環境科学) 乙第6967号
Issue Date	2015-09-25
DOI	10.14943/doctoral.r6967
Doc URL	http://hdl.handle.net/2115/63756
Type	theses (doctoral)
File Information	Kensaku_Kodama.pdf

Electrochemical interface in fuel cell reactions

Kensaku Kodama

Graduate School of Environmental Science, Hokkaido University

2015

Table of contents

Symbols ... iii
Abbreviations ... iv
Abstract ... v

Chapter 1 Introduction ... 1
- **1.1 Automobile application of PEFC** ... 2
- **1.2 Catalyst layer** ... 3
- **1.3 Challenges in PEFC development** ... 5
  - **1.3.1 Initial performance** ... 5
  - **1.3.2 Durability** ... 7
- **1.4 Role of spectator species** ... 8
- **1.5 Contents of this thesis** ... 8
- **1.6 References** ... 10

Chapter 2 Experimentals and fundamentals of analyses ... 13
- **2.1 Electrochemical cell** ... 14
- **2.2 Preparation of single crystal electrode** ... 15
- **2.3 Analysis of kinetics** ... 17
- **2.4 References** ... 18

Chapter 3 Kinetics of fundamental reactions on platinum electrode ... 19
- **3.1 Oxide formation** ... 20
  - **3.1.1 Experimental** ... 21
  - **3.1.2 Results** ... 22
  - **3.1.3 Discussion** ... 26
  - **3.1.4 Conclusions** ... 28
- **3.2 Oxygen reduction reaction** ... 30
  - **3.2.1 Experimental** ... 31
  - **3.2.2 Results** ... 33
  - **3.2.3 Discussion** ... 36
  - **3.2.4 Conclusions** ... 36
- **3.3 References** ... 37

Chapter 4 The role of non-covalent interactions in electrochemical reactions ... 39
- **4.1 Effects on fuel cell reactions** ... 40
  - **4.1.1 Experimental** ... 41
  - **4.1.2 Results** ... 41
  - **4.1.3 Discussion** ... 44
  - **4.1.4 Cation effect in acid** ... 45

4.1.5 Conclusions 45
4.2 Effects on bulk CO oxidation 47
4.2.1 Experimental 47
4.2.2 Results and discussion 48
4.2.3 Conclusions 54
4.3 References 56
Chapter 5 Pt/ionomer interface 59
5.1 Oxygen reduction reaction at Pt/ionomer interface 60
5.1.1 Experimental 61
5.1.2 Results and Discussion 62
5.1.3 Conclusions 64
5.2 Ionomer effect under dry conditions 65
5.2.1 Experimental 65
5.2.2 Results and Discussion 66
5.2.3 Conclusions 69
5.3 Catalyst poisoning property of sulfonimide acid ionomer 70
5.3.1 Experimental 71
5.3.2 Results and Discussion 71
5.3.3 Conclusions 74
5.4 Molecular-scale understanding (Future work) 75
5.4.1 Experimental 75
5.4.2 Results 76
5.4.3 Discussion (Assignments) 78
5.4.4 Analyses in liquid systems 80
5.4.5 Conclusions 84
5.5 References 85
Chapter 6 General conclusions and outlook 87

Appendix 93
A. Estimation of reaction order of ORR 94
B. Key points for forming the uniform ionomer film 98

Symbols

E	electrode potential
F	the Faraday constant; charge on one mole of electrons
G	Gibbs free energy
H	enthalpy
i	current density due to electrochemical reaction
i_0	exchange current density
i_d	diffusion-limiting current density
i'_d	diffusion-limiting current density in a standard bulk concentration of O_2
i_k	kinetics-limiting current density
n	stoichiometric number of electrons involved in an electrochemical reaction
R	gas constant
T	absolute temperature
α	symmetry factor
γ	reaction order
η	overpotential
θ_i (Θ_i)	coverage of species i on the electrode surface

Abbreviations

CE	counter electrode
CO_b	bulk CO
CV	cyclic voltammogram
DFT	density functional theory
EDS	energy-dispersive X-ray spectroscopy
EW	equivalent weight; the weight of polymer in the unit of gram per the amount of sulfonic acid group in the unit of mole
HM-RDE	hanging meniscus rotating disk electrode
HOR	hydrogen oxidation reaction
H_{upd}	underpotentially deposited hydrogen
IHP	inner Helmholtz plane
IR	infrared
LSV	linear sweep voltammetry
ML	monolayer
MOR	methanol oxidation reaction
NBC4	the name of a novel sulfonimide ionomer developed by Shinohara et al.
NFBSA	nonafluorobutane sulfonic acid
OHP	outer Helmholtz plane
ORR	oxygen reduction reaction
PEFC	polymer electrolyte fuel cell
PFSA	perfluorinated sulfonic acid polymer
Pt/C	Pt nanoparticles supported on carbon particles
RDE	rotating disk electrode
RE	reference electrode
RHE	reversible hydrogen electrode
SEIRAS	surface-enhanced infrared absorption spectroscopy
SEM	scanning electron microscope
SHE	standard hydrogen electrode
STM	scanning tunneling microscopy
TFMSA	trifluoromethane sulfonic acid
WE	working electrode
XPS	X-ray photoelectron spectroscopic
XRS	X-ray scattering

学位論文内容の要旨

博士（環境科学）　兒玉 健作

学位論文題名

Electrochemical interface in fuel cell reactions
（燃料電池反応中の電気化学界面）

固体高分子型燃料電池（PEFC）では電極触媒として貴金属である白金（Pt）が使用されており、その使用量低減が PEFC 実用化の鍵となっている。触媒を最大限活用するためには、反応を阻害する酸化物やアニオンなどの白金上吸着物質の被覆率を可能な限り小さくする必要がある。そのためには、種々の吸着物質の電気化学環境下での振舞いならびに燃料電池反応(水素酸化反応(HOR)、酸素還元反応(ORR)、メタノール酸化反応など)の速度に対する影響を定量的に評価する必要がある。本論文では、PEFC の燃料極あるいは空気極を模擬したモデル電極による実験から、燃料電池反応進行中の種々の吸着物質の役割を解明することを目的とする。第一章で序論を述べ、第二章で実験・解析手法の説明を行う。それ以降は以下の構成からなる。

第三章では、PEFC 空気極において最も基本的な反応阻害因子である白金酸化物に注目した。これまで、白金酸化物については正確な構造、および酸化物生成メカニズムについて、統一した説明がなされてこなかった。この課題の解決に向けた第一歩として、最も単純なモデル表面である Pt(111)上の酸化物生成速度の電位依存性を調べた。その結果、この反応速度が、非常に大きな電位依存性（小さな Tafel 勾配；～20mV・decade^{-1}）を持つことを見出した。この実験結果は、これまで最も受け入れられてきた酸化物生成モデルである内部酸化(subsurface-oxidation または place-exchange)モデルでは説明できないことが分かり、それに代わるモデルとして、酸化物生成反応が、速い電子移動素過程と、それに続く遅い過程との組み合わせから成るというメカニズムを提案した。つづいて、ORR における反応中間体としての白金酸化物の特性を調べるため、PEFC 空気極電位領域、0.8-1.0V において、Pt(111)上 ORR 反応次数を実験的に求めた。その際、従来の解析法より精度よく体系的に反応次数を見積もる方法を提案した。実験の結果、ORR 反応次数は酸においては 1、アルカリにおいては 0.5-0.9 であることが分かった。これは、酸中では反応速度が増加しても反応中間体が電極表面に溜まらないこと、アルカリ中では反応速度の増加とともにそれが溜まることを示している。現時点で酸とアルカリとでの ORR メカニズムの違いを解明するには至っていないが、少なくとも酸環境のプロトン交換型の PEFC においては、ORR 進行中に反応中間体の被覆率は変化しないため、ORR 速度を議論する際、反応中間体以外の吸着物質（spectator-species: 水が酸化することにより生成する酸化物や、アイオノマ高分子中のアニオンなど）の被覆率のみに注目すればよいことが分かった。

第四章では、電気化学反応における spectator-species の役割をより深く理解できる系として、アルカリ中 Pt 電極上メタノール酸化およびバルク CO 酸化へのカチオン種の

影響を調べた。従来、水系の電解液における電位窓、0-1.5V(水素電極基準)では、アルカリ（土類）金属カチオンはPt電極表面に共有結合的に吸着しないため、電極反応の阻害因子にはなり得ないと考えられてきた。しかし、本論文の研究により、この概念が誤りであり、アルカリ（土類）金属カチオンは、Pt電極上の水酸化物(OH(ads))を介した非共有結合性相互作用により電極近傍に水和クラスタを形成し、spectator-spciesとして上記反応に影響を与えることが見出された。バルクCO酸化反応の解析においては、OH(ads)被覆率が大きい場合のみ非共有結合性相互作用の影響が現われることが明確に示され、上記クラスタモデルが正しいことが裏付けられた。

第五章では、PEFC開発に向けた実践的な系として、Pt/アイオノマ界面を扱った。近年、アイオノマ物性がPEFCの性能に大きく影響することが分かっている。そこでまず、新規アイオノマ開発に向けたベンチマークとして、現在アイオノマとして主に用いられているパーフルオロスルホン酸ポリマ（PFSA、例えばNafion®）について、スルホン酸アニオンのPtへの吸着量およびそのORRへの影響を、Pt単結晶(111)電極を用いて定量的に評価した。この定量評価は、電極表面をアイオノマで均一に被覆する方法を確立したことで可能となっている。実験の結果、NafionでPt電極を被覆した場合、高分子中のスルホン酸アニオンは被覆率0.07モノレイヤでPtに吸着し、PtのORR活性は70%低下することが明らかになった。これは、Pt表面の30%しか触媒として活用できていないことを意味する。つづいて、Pt/アイオノマ界面を乾燥条件下で解析するため、Pt単結晶用固体電気化学セルを開発した。これにより、Pt(111)単結晶の明確なサイクリックボルタモグラムを固体セルで測定することに初めて成功し、スルホン酸アニオンのPtへの吸着性が、アイオノマの乾燥とともに増加することを見出した。この事実は、PEFCを低加湿で運転する際に重要な知見となる。さらに、アイオノマによる触媒被毒の抑制に向け、PFSAとアニオン構造の異なる、2官能型パーフルオロスルホンイミド酸アイオノマ(NBC4)の触媒被毒性を評価した。その結果、NBC4で被覆したPt(111)電極は、Nafionで被覆したそれよりアニオン被毒が少なく、ORR活性が50%高いことが分かった。これは、スルホンイミドのように嵩高い酸基構造にすることで、アイオノマの触媒被毒を低減できる可能性を示しており、新規アイオノマの分子構造の設計に役立つ知見である。論文の最後では、現在取り組んでいる、表面増強赤外吸収分光法(SEIRAS)を用いたPt/アイオノマ界面の解析について、手法の詳細やこれまで得られている結果を紹介した。電位スイープ中のSEIRAスペクトルにおいて、Ptに吸着したスルホン酸アニオンに由来すると思われるバンドが1400cm^{-1}付近に見つかり、また、Nafionのパーフルオロ骨格部分（主鎖・側鎖）や水分子の動きに由来すると思われるスペクトルの電位依存性を確認することができた。したがって、本手法の活用により、Pt/アイオノマ界面の全容が解明されることが期待される。

以上のように、白金電極上の種々の吸着物質の生成反応速度、被覆率、燃料電池反応に対する影響などを定量的に評価することで、今後のPEFC開発に役立つ知見が具体的に示された。

Chapter 1

Introduction

1.1 Automobile application of PEFC

In the growing concerns about environmental issues and sustainability, energy conversion devices with high efficiency and no emissions of greenhouse gases are desired. Automobiles that are propelled by electric motors are attractive in this respect because they are free from the Carnot-cycle limitation and do not emit exhaust gases in contrast to automobiles with internal combustion engines [1].

Fuel cell vehicles, in which the electricity is generated by electrochemical reactions of a continuously supplied fuel of reductant, such as hydrogen, and an oxidant such as oxygen in air, have an advantage regarding travel distance over electric vehicles with batteries, because of the weight-based high energy density for hydrogen [2], while their effectiveness still depends on the efficiencies of off-board steps including production, storage and transport of hydrogen [3, 4]. Depending on the form of the electrolyte, there are various types of fuel cells: e.g. polymer electrolyte fuel cell (PEFC), phosphoric acid fuel cell (PAFC), molten carbonate fuel cell (MCFC) and solid oxide fuel cell (SOFC) [5]. Among these types, proton-exchange-type PEFCs operated with hydrogen are currently the best choice for the automobile application because of their low operating temperature (50-100 °C) and high specific power (output per volume and weight) [6].

A typical composition of a PEFC is shown in Fig. 1.1.1. A polymer electrolyte membrane is used as the electrolyte and sandwiched by "catalyst layers", which generally consist of catalysts of Pt nanoparticles supported on carbon particles (Pt/C), polymer electrolytes covering the catalysts for forming good electrochemical interfaces, which is called "ionomer" to distinguish it from the electrolyte membrane, and pores for gas diffusions. The cells with this composition are stacked in series to obtain enough powers for automobile applications. Electric power is generated by the reactions of hydrogen oxidation reaction (HOR) and oxygen reduction reaction (ORR) taking place at the anode and cathode, respectively;

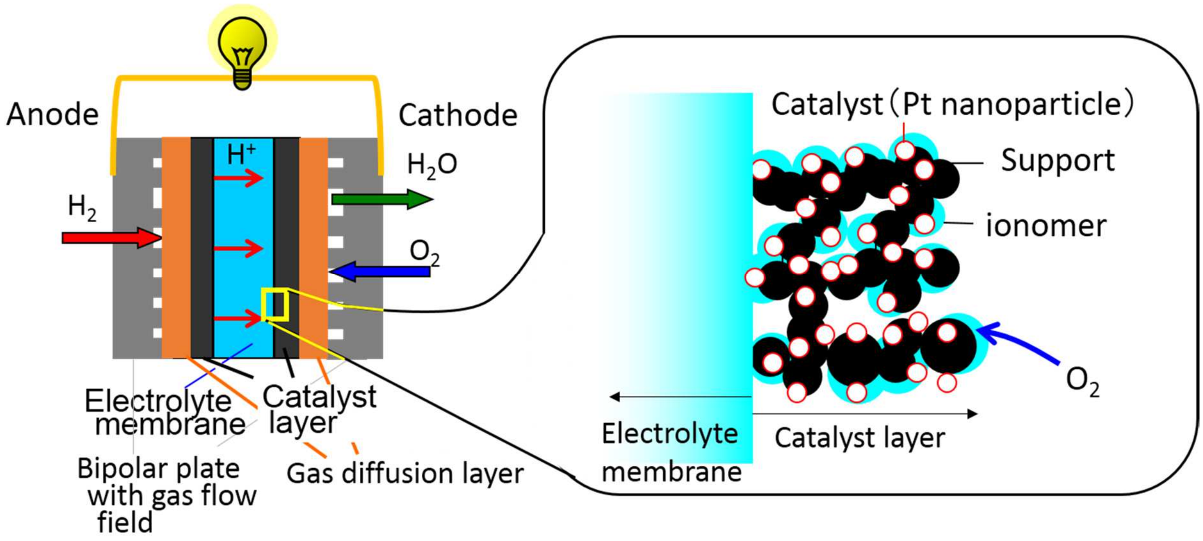

Fig. 1.1.1 A typical composition of PEFC.

$$\text{(anode)} \quad H_2 \rightarrow 2\,H^+ + 2\,e^- \qquad (1)$$

$$\text{(cathode)}\ 1/2\ O_2 + 2\,H^+ + 2\,e^- \rightarrow H_2O \qquad (2).$$

The theoretical cell-voltage, E_0, calculated from the Gibbs free energy for the total reaction ($H_2 + 1/2\ O_2 \rightarrow H_2O$), -237.13 $kJmol^{-1}$ [7], is 1.23 V at 298 K. The theoretical energy conversation efficiency is calculated to be 83 % from the ratio of the Gibbs free energy to the enthalpy for the total reaction, $\Delta G^o/\Delta H^o$. Although CO_2 is emitted in industrial mass production of H_2 from fossil fuels, the high energy conversion can eventually reduce the CO_2 emission.

1.2 Catalyst layer

The fuel cell reactions take place in the catalyst layers, where the reactant gasses, proton and electrons meet. The microstructure of the catalyst layer, therefore, significantly affects the fuel cell performance. In this section, the history of the research and development of high-performance catalyst layer is reviewed and the microscopic views of the catalyst layer are presented [3].

In the early stage of PEFC development, the electrode was fabricated by hot-pressing a mixture of Pt black (with the specific surface area of ca. 25 m^2g^{-1}) and fine particles of polytetrafluoroethylene (PTFE) directly onto an electrolyte membrane. This type of electrode showed a poor cell performance, largely because of a limited penetration of ionomer into the electrode from the membrane and consequent low proton conductivity in the catalyst layer region. In a subsequent study by Raistrick [8], Pt/C (with the specific surface area of 60 - 100 m^2g^{-1}), instead of Pt black, was bound to a carbon paper or cloth as a gas-diffusion layer using PTFE, and the catalyst side of the electrode is then impregnated with solubilized ionomer, followed by evaporation of the solvent and then by hot-pressing onto the membrane. Through this change in the fabrication method, the amount of Pt loading was significantly reduced (from ca. 4 $mg \cdot cm^{-2}$ to ca. 0.4 $mg \cdot cm^{-2}$ on the basis of geometric electrode area). In those two methods, PTFE was added to form hydrophobic gas diffusion pores free from flooding. As a negative effect, however, the fine PTFE particles were found to block active sites on Pt catalysts [9].

Further reduction of Pt loading (to 0.15 – 0.20 $mg \cdot cm^{-2}$) without a loss of the performance was achieved by Wilson and Gottesfeld [10], with a new approach, in which a catalyst layer was cast from an ink of Pt/C catalyst and solubilized ionomer, and resulting solid ionomer phase, instead of PTFE applied in the above conventional methods, served as binder as well as proton conductor. The high performance of the PTFE-free electrode implicates that gas-diffusion pores can be appropriately formed even without PTFE during the evaporation of solvent in the catalyst ink. The ink-process was further studied by many other groups [3, 11-15], with various modification, some of which included the addition of PTFE as well as ionomer into the catalyst dispersion for mitigating the flooding of catalyst layer with water under humid conditions.

It should be also noted that 3M company recently invented a novel ionomer-free electrode consisting of an assemblage of organic whiskers covered by thin layers of Pt or Pt alloy, and showed its higher performance than the conventional Pt/C based catalyst layer including ionomer under certain operating conditions [16]. The higher performance of the ionomer-free electrode indicates that protons can be transported to the catalyst surfaces without ionomer by some mechanisms such as surface diffusion of adsorbed hydrogen atoms on Pt surface (the so-called “spillover”) [17-19], water-mediated conduction [20], and localized pH variation [21]. The new catalyst, however, still has a problem of robustness: low performances under too dry and too humid conditions. Hence, ionomer is still required in catalyst layers at the present stage.

Microstructures of ionomers in a catalyst layer determine the proton conductivity and the gas diffusivity at the vicinities of the Pt surfaces, and therefore, have been studied with a particular interest. Because the identification of the nano-scale complex structure composed of ionomer and Pt/C from direct observations is difficult, the major strategy has been the “modelling” of micro structures that can comprehensively simulate the cell performances. Ionomer-filled agglomerates with the radius of between 0.1 and 1 μm, consisting of Pt/C particles, have been used for explaining mass-transport effects (see Section 1.3.1) in PEFC performances [22, 23]. In those studies, the data fittings with the experimental results were carried out by assuming that the reactant gas in pores (gas phases) of the catalyst layer is in equilibrium with that in ionomers (no mass-transport resistance exists at the gas-phase/ionomer interface). In a recent study by Suzuki et al. [24], however, agglomerates with such large sizes were not found as main components in the images of the catalyst layers using a high-resolution scanning electron microscope (Fig. 1.2.1a), and mass transfer effects in the cell performances were explained by the oxygen transport resistance at the interface between gas-phase/ionomer or between ionomer/Pt, the values of which had been measured in separate model experiments, while each Pt/C particle was assumed to be covered by a thin (< 3 nm) ionomer film without forming an agglomerate. The importance of the interfacial mass-transport resistances is now well recognized [25, 26], and the description of the microstructure of the catalyst layer suggested by Suzuki et al. [24] is likely to be reasonable. A schematic of the surround of a Pt catalyst based on their conclusion is shown in Fig. 1.2.1b.

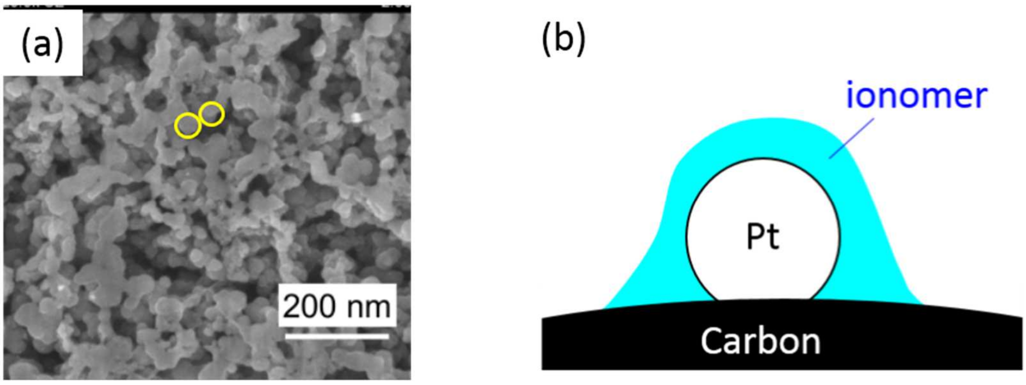

Fig. 1.2.1 (a) A secondary electron image of the cross-section of the cathode catalyst layer prepared with focused ion beam milling. (obtained by Juntaro Seki from Toyota Central R&D Labs. Inc.) Yellow circles correspond to the size of a primary carbon particle. (b) A present microscopic view of the surround of a Pt catalyst in PEFCs.

1.3 Challenges in PEFC development

For the commercialization of Fuel Cell vehicles, one of the most critical challenge is the cost for the production of fuel cell stacks. For example, Department of Energy (DOE) sets the ultimate cost target at \$ 30 / kW for a fuel cell stack [27], the maximum power of which is 114 kW for the fuel cell vehicle of “MIRAI” from Toyota [28]. The key issue in the cost reduction is the reduction of the used amount of platinum, the most effective electrocatalyst, which can be achieved, for example, by increasing the surface area though using smaller nanoparticles. The loading amount of Pt has been proposed to be reduced to 1/10 of the current loadings by New Energy and Industrial Technology Development Organization (NEDO) [29]. These cost targets, of course, have to be achieved at least without deteriorating the performance of the cell including the initial performance and durability, which are discussed in the following sections.

1.3.1 Initial performance

In the operations of PEFCs, the maximum theoretical cell-voltage, 1.23 V at 298 K, cannot be obtained and the practical efficiency of the fuel cell is usually 40 - 60 % in real PEFCs. (The theoretical one is 83 % at 298 K, calculated from $\Delta G^o/\Delta H^o$.) The main causes of the lowered voltage is classified into 1) slow reaction kinetics for ORR in the small current region, 2) ohmic loss for proton-transport in a middle current region, and 3) mass transport limitations for the reactants in the large current region. These factors can be found in a typical current-voltage curve for a PEFC shown in Fig. 1.3.1. In analytical studies for PEFCs, one of the goal is to understand the each barrier from the viewpoints of physics and chemistry related to the components of the cell, including membrane, support, Pt catalyst, ionomer, and the interfaces between them. In the following sections, these points are briefly discussed.

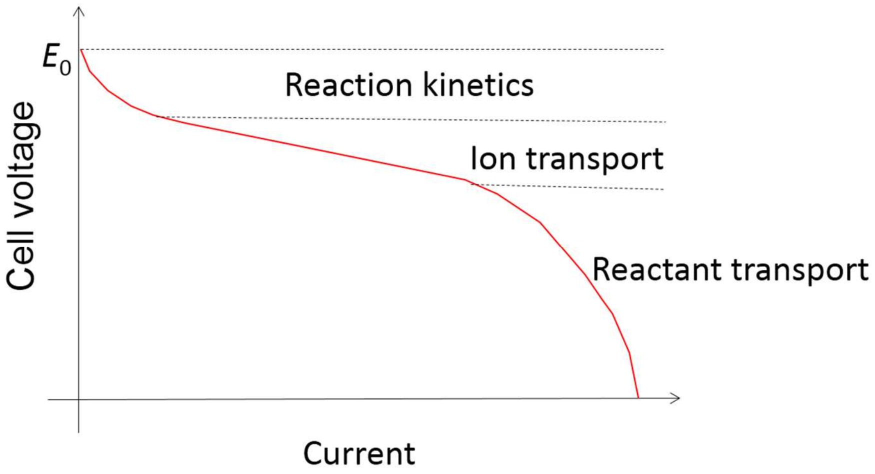

Fig. 1.3.1 A typical current-voltage curve for PEFC (red curve). The main cause of the voltage loss in each current region was posted.

Reaction kinetics for ORR

The reaction kinetics is, in principle, a matter only in the cathodic process because the exchange current density (the forward or backward reaction current density at equilibrium, see Section 2.3) for ORR on Pt is smaller by 7 orders of magnitude than that for HOR [30, 31]. The slow ORR rate has been ascribed to the slow removal of adsorbed (hydr)oxide on the Pt surface, the key step in ORR, due to the strong binding [32-35]. Au is much less active than Pt for ORR despite its small oxygen-binding energy. In this case, the low activity is ascribed to the slow oxygen adsorption. The plot of the ORR activity *vs.* the binding energy of the hydroxyl yields the so-called “volcano” profile [32], which can be explained in terms of the Sabatier principle that catalytic activity is maximal when the interaction between the catalyst and the substance is not too week and not too strong.

Tuning the electocatalytic property is the challenging theme in developing ORR electrocatalyst and the Sabatier principle is the guideline for this purpose. Alloying Pt with other element(s) is a possible way to enhance the electrocatalytic activity of Pt. $Pt_3Ni(111)$ has been experimentally shown to have 10 times larger ORR specific activity (activity per electrode surface area) than pure Pt(111) [36]. The surface structure of the Pt alloy catalyst has been characterized and found to have the so-called “Pt skin” structure, where the thin layer (at the levels of a few ML) of pure Pt phase covers the bulk alloy phase [37]. This “skin” structure plays a key role in tuning the oxophilicity of electrode surface, and the application of Pt alloy materials to the nanostructured cathode catalysts is one of the most important theme in the recent research of PEFCs [38-41].

Another factor for determining the reaction kinetics is the effects of spectator species such as anions in ionomer molecules, water, and impurities. Actually, the roles of spectator species in fuel cell reactions are the main subject of this thesis and will be again mentioned in Section 1.4.

Proton-transport

Protons in PEFCs are conducted through a polymer electrolyte, for which perfluorinated sulfonic acid polymer (PFSA) is almost exclusively used because of its high chemical stability and strong acidity. Fig. 1.3.2 shows the structure of Nafion® as an example of PFSA; the ratio of x/y is an important parameter determining the “equivalent weight” (EW, the weight of polymer in the unit of gram per the amount of sulfonic acid group in the unit of mole) and surely the proton conductance. In the bulk phase of hydrated PFSA membrane, segregation occurs between hydrophobic perfluorinated parts and hydrophilic sulfonic acid groups, the latter of which forms water channels with the size of 2 – 3 nm [42]. The hydration state of the membrane affects the segregation-morphology and consequently the proton-transport resistance, which is increased and becomes a problem with the drying of the membrane [43].

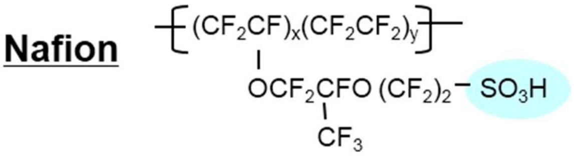

$$-[(CF_2CF)_x(CF_2CF_2)_y]- \quad OCF_2CF(CF_3)O(CF_2)_2-SO_3H$$

Fig. 1.3.2 Molecular structure of Nafion®.

The nano-scale morphology in the ionomer phase in the catalyst layers, however, should be different from that in the membrane, because the thickness of ionomer film on the Pt catalysts is in the scale of a few nanometers as described in Section 1.2, which is close to the size of the water channels in the membrane. The investigation of the relationship between the nano-scale morphology and proton conductivity in an ionomer thin film is the recent hot issues in fuel cell researches [44].

Mass-transport

The decrease in the cell voltage in the high current region (Fig. 1.3.1) is caused by the mass transport resistances in the gas-diffusion layers and catalyst layers. Therefore, appropriate designs of those components as well as the gas flow field of the bipolar plates (Fig. 1.1.1) are required for controlling the supplies of the reactants (H_2 and O_2) and the emission of the product (H_2O).

Recently, the ionomer films on the Pt surfaces in the cathode were also found to play important roles in O_2 transport to the catalyst surfaces as described in Section 1.2 [24, 45-47]. In a subsequent study, the presence of the mass transport resistance at the Pt/ionomer interface has been reported [48] and this observation suggests that the total Pt surface area can determines the mass transport property. (The mass transport rate should be proportional to the total Pt surface area if the resistance exists at the Pt/ionomer interface). Therefore, the total Pt surface area has to be kept large for keeping the cell performance in a high current region even if high mass-activity (activity per the loading of precious metals) catalysts are invented. In the same manner, the coverages of spectator species blocking the active sites on the catalyst have to be minimized for improving not only the reaction kinetics but also the mass transport rate because of the presence of the Pt/ionomer interfacial mass-transport resistance.

1.3.2 Durability

For automobile application, the durability of 5000 operating hours for fuel cell stacks is required [27]. The performances of the stacks, however, can be deteriorated by various processes [3]. In particular, the degradations of catalysts and electrolyte membranes have been widely studied from both practical and scientific viewpoints.

The degradation of catalysts is mainly caused by the corrosions of Pt nanoparticles and carbon supports, which lead to the decrease in the total Pt surface areas and porosity of the catalyst layer for the gas diffusions. Recent studies have shown that Pt dissolution is accelerated by potential cycles of cathode [49, 50], which is inevitable under operating conditions in automobile applications.

Electrolyte membranes can be degraded by chemical processes of the attacking by radicals formed through the dissociations of hydrogen peroxide as a cathode by-product or through some other mechanisms, or by the physical processes of mechanical stresses caused by repeated wetting (swelling) and drying (shrinking) of the membrane [51]. The chemical and physical degradation processes are accelerated in the open-circuit and potential-cycles (“on-off” cycles) modes, respectively [52, 53].

Although the topics of the durability are as important as those of the initial performance, I only treat the initial performance in this thesis with the focus on the roles of spectator species in fuel cell reactions.

1.4 Role of spectator species

The property of Pt/ionomer interface in the cathode catalyst layer significantly affects the ORR kinetics [54] and potentially the O_2 transport to the Pt surface as mentioned above, and thus is an important key factor for improving the cell performance.

Figure 1.4.1 shows the schematic of the interface between Pt and ionomer of perfluorinated sulfonic acid polymer, where O_2 molecules that have traveled through the ionomer are reduced at Pt surface free from adsorbates. While sulfonate anions always exist in this system, they have not been regarded as dominant adsorbates in the past because their mobile regions should be confined by the perfluorinated parts of the ionomer molecules. Recent studies, however, clearly showed that sulfonate anion in ionomer is adsorbed on Pt surface and ORR kinetics is affected by its adsorption [55-59].

Reaction intermediates also block the active sites if their removals are slow. Another important participant is water, which can affect the stabilities of other species [58] and can be oxidized to oxygenated species (such as OH and O) on the Pt surface having the blocking effect for ORR [60].

The blocking effect is expressed by $(1-\sum_i \Theta_i)$ in the pre-exponential factor of the reaction rate, where Θ_i is the coverage of species i, and thus determine the catalytic activity [54]. Understanding the properties of adsorbed species on Pt surface in PEFC operations is, therefore, another critically important issue for improving the electrocatalytic activity.

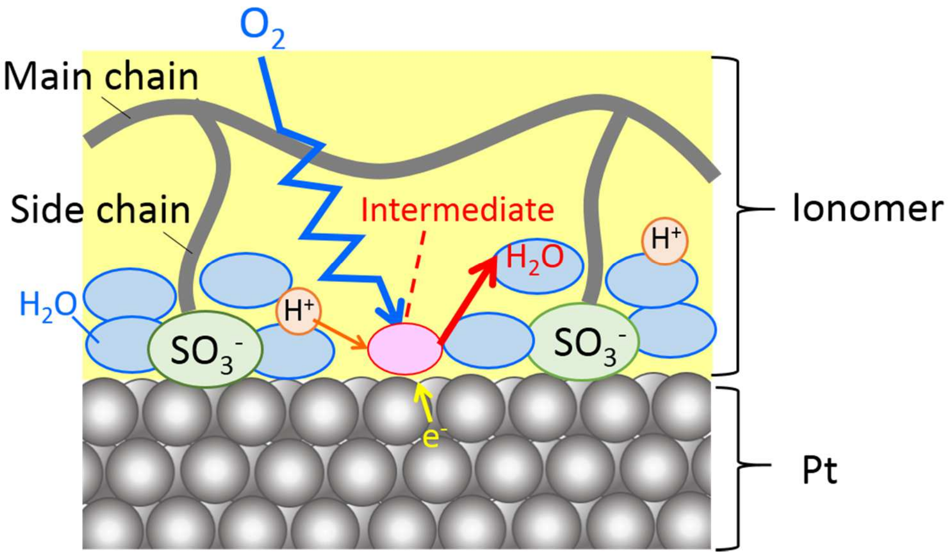

Fig. 1.4.1 Schematic of the Pt/ionomer interface.

1.5 Contents of this thesis

Even for investigating the practical system of Pt/ionomer interface in PEFCs, it is helpful to start the study with a generalized system of the interface between Pt and aqueous electrolyte including various types of adsorbed or near-surface species. Fig.1.5.1 shows the schematic of the interface, the so-called

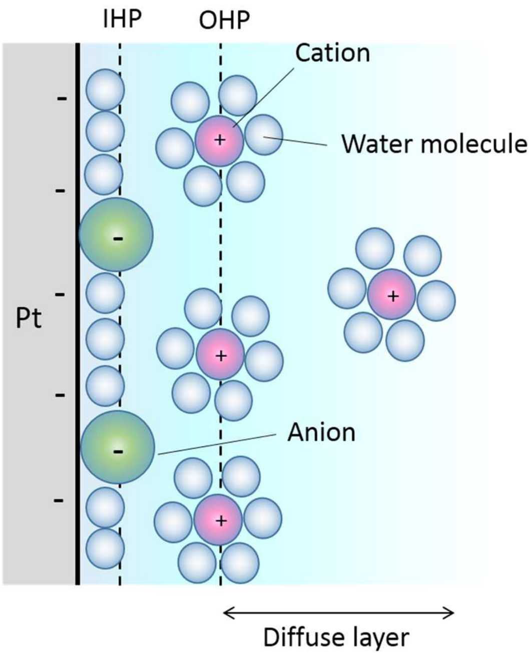

Fig. 1.5.1 A model for the interface between Pt electrode and aqueous electrolyte.

"electric double layer region" [61]. The first layer on the solution side contains water molecules and sometimes other species, the latter of which are said to be "specifically adsorbed species". Many types of anion are known to be specifically adsorbed on Pt surface. Adsorbed oxygenated species such as hydroxyl (OH(ads)) and oxygen atom (O(ads)) formed *via* the oxidations of water molecules can be also regarded as the same kind of species as the specifically adsorbed species in the sense that they are directly bonded with the Pt atoms. The locus of the centers of the specifically adsorbed species is called the "inner Helmholtz plane" (IHP). Cation is usually hydrated and therefore can approach to the electrode surface only to the distance corresponding to the thickness of the hydration shell. The locus of the electrical centers of those nearest hydrated cations is called the "outer Helmholtz plane" (OHP). The region where the charged species are distributed by the balance between the electrostatic interactions with the charged electrode and thermal motions is called the "diffuse layer", which extends from the OHP into the bulk of the solution.

In this thesis, the effects of the three types of adsorbed or near-surface species, oxygenated species, hydrated cations and specifically adsorbed anions, on the kinetics of various electrocatalytic reactions related to polymer electrolyte fuel cells, are separately studied. The thesis consists of five chapters including this Chapter devoted to Introduction. In Chapter 2, fundamentals and backgrounds of the analytical methods covering most parts of this thesis are presented. In Chapter 3, the focus is on the oxygenated species, which can be also called Pt (hydr)oxides if adjacent Pt atoms are included. In particular, the kinetics of oxide formation reaction and the roles of reaction intermediates in ORR are analyzed on the model surface of Pt (111) [62]. In Chapter 4, the effects of hydrated cations on several types of electrochemical reactions are investigated in alkaline solution. In this system, significant reaction-blocking or -promoting effects due to the so-called “non-covalent interactions” were newly found [63-65]. Although the systems treated in those two chapters are simper than the practical systems of Pt catalysts covered by ionomer films in PEFCs, general aspects of electrocatalytic interface can be learned and thus foundations for understanding more complicated systems with ionomer are provided. Then, Pt surface with ionomer is treated as a more practical research for developing PEFCs in Chapter 5, where the effects of specifically adsorbed anions in ionomer molecules on the model surface of Pt (111) are mainly investigated. For studying the ionomer effects under more realistic conditions, a novel analytical system (solid-state cell with Pt single crystals) was established [58]. In addition, the strategy for mitigating the catalyst poisonings with ionomers is presented by comparing the poisoning properties of different types of ionomer [59]. The general conclusions of this thesis are summarized in Chapter 6.

1.6 References

[1] M. Ehsani, Y. Gao, S.E. Gay, A. Emadi, *Modern Electric, Hybrid Electric, and Fuel cell Vehicles,* *Fundamentals, Theory, and Design*, CRC Press (2005) .

[2] F.T. Wagner, B. Lakshmanan, M.F. Mathias, *J. Phys. Chem. Lett.*, **1** (2010) 2204 .

[3] *Handbook of Fuel Cells, Vol 3,* W. Ielstich et al. ed., Wiley (2003) .

[4] *Prospects for Hydrogen and Fuel Cells,* OECD/IEA, (2005) ..

[5] J. Larminie, A. Dicks, *Fuel Cell Systems Explained, John Wiley & Sons*, (2000).

[6] *Handbook of Fuel Cells, Vol 1*, W. Ielstich et al. ed., Wiley (2003)

[7] D.R. Lide, *Handbook of Chemistry and Physics,* CRC press, New York, (1997).

[8] I.D. Raistrick, *"Modified Gas Diffusion Electrode for Proton Exchange Membrane Fuel Cells"* presented at Symposium on Diaphragms, Seperators and Ion-Exchange Membranes, Pennington, NJ, (1986) .

[9] M.S. Wilson, S. Gottesfeld, *J. Electrochem. Soc.*, **139** (1992) L28.

[10] M.S. Wilson, S. Gottesfeld, *J. Appl. Electrochem.*, **22** (1992) 1.

[11] M. Uchida, Y. Aoyama, N. Eda, A. Ohta, *J. Electrochem. Soc.*, **142** (1995) 463.

[12] A. Fischer, W. Hartmut, R. Zuber, *US Patent* 5, 861, 222, (1999) .

[13] T. Tomoyuki, *US Patent* 5, 843, 519, (1998) .

[14] G.A. Hards, T.R. Ralph, *US Patent* 5, 501, 915, (1996) .

[15] S. Swathirajan, Y.M. Mikhail, EP Patent 0, 569, 062 B1, (1993) .

[16] M.K. Debe, *Nature,* **486** (2012) 43 .

[17] J. McBreen, *J. Electrochem. Soc.,* **132** (1985) 1112 .

[18] J.H. Jiang, B.L. Wu, C.S. Cha, R.S. Zhai, *J. Electroanal. Chem.*, **445** (1998) 13 .

[19] S. Tominaka, C.W. Wu, K. Kuroda, T. Osaka, *J. Power Sources,* **195** (2010) 2236 .

[20] K. Chan, M. Eikerling, *J. Electrochem. Soc.*, **158** (2011) B18 .

[21] I.V. Zenyuk, S. Litster, *Electrochim. Acta*, **146** (2014) 194 .

[22] K. Broka, P. Ekdunge, *J. Appl. Electrochem.*, **27** (1997) 281 .

[23] F. Jaouen, G. Lindbergh, G. Sundholm, *J. Electrochem. Soc.*, **149** (2002) A437 .

[24] T. Suzuki, K. Kudo, Y. Morimoto, *J. Power Sources*, **222** (2013) 379 .

[25] M. Moore, P. Wardlaw, P. Dobson, J.J. Boisvert, A. Putz, R.J. Spiteri, M. Secanell, *J. Electrochem. Soc.*, **161** (2014) E3125 .

[26] Y. Ono, A. Ohma, K. Shinohara, K. Fushinobu, *J. Electrochem. Soc.*, **160** (2013) F779 .

[27] *2014 Annual Progress Report in Hydrogen and Fuel Cells Program in DOE*, (2014) .

[28] *Website of Toyota*

[29] *2014 Annual Report from NEDO*, (2014) .

[30] K.C. Neyerlin, W.B. Gu, J. Jorne, H.A. Gasteiger, *J. Electrochem. Soc.*, **153** (2006) A1955 .

[31] K.C. Neyerlin, W.B. Gu, J. Jorne, H.A. Gasteiger, *J. Electrochem. Soc.*, **154** (2007) B631 .

[32] J.K. Norskov, J. Rossmeisl, A. Logadottir, L. Lindqvist, J.R. Kitchin, T. Bligaard, H. Jonsson, *J. Phys. Chem. B*, **108** (2004) 17886 .

[33] J. Rossmeisl, G.S. Karlberg, T. Jaramillo, J.K. Norskov, *Faraday Discuss.*, **140** (2008) 337 .

[34] R. Jinnouchi, K. Kodama, T. Hatanaka, Y. Morimoto, *Phys. Chem. Chem. Phys.*, **13** (2011) 21070 .

[35] I.E.L. Stephens, A.S. Bondarenko, U. Gronbjerg, J. Rossmeisl, I. Chorkendorff, *Energy Environ. Sci.*, **5** (2012) 6744 .

[36] V.R. Stamenkovic, B. Fowler, B.S. Mun, G.F. Wang, P.N. Ross, C.A. Lucas, N.M. Markovic, *Science*, **315** (2007) 493 .

[37] V.R. Stamenkovic, B.S. Mun, M. Arenz, K.J.J. Mayrhofer, C.A. Lucas, G.F. Wang, P.N. Ross, N.M. Markovic, *Nat. Mater.*, **6** (2007) 241 .

[38] D.F. van der Vliet, C. Wang, D. Tripkovic, D. Strmcnik, X.F. Zhang, M.K. Debe, R.T. Atanasoski, N.M. Markovic, V.R. Stamenkovic, *Nat. Mater.*, **11** (2012) 1051 .

[39] C. Chen, Y.J. Kang, Z.Y. Huo, Z.W. Zhu, W.Y. Huang, H.L.L. Xin, J.D. Snyder, D.G. Li, J.A. Herron, M. Mavrikakis, M.F. Chi, K.L. More, Y.D. Li, N.M. Markovic, G.A. Somorjai, P.D. Yang, V.R. Stamenkovic, *Science*, **343** (2014) 1339 .

[40] L. Gan, C.H. Cui, M. Heggen, F. Dionigi, S. Rudi, P. Strasser, *Science*, **346** (2014) 1502 .

[41] P. Hernandez-Fernandez, F. Masini, D.N. McCarthy, C.E. Strebel, D. Friebel, D. Deiana, P. Malacrida, A. Nierhoff, A. Bodin, A.M. Wise, J.H. Nielsen, T.W. Hansen, A. Nilsson, I.E.L. Stephens, I. Chorkendorff, *Nat. Chem.*, **6** (2014) 732 .

[42] T.D. Gierke, G.E. Munn, F.C. Wilson, *J. Polym. Sci. Pt. B-Polym. Phys.*, **19** (1981) 1687 .

[43] T.A. Zawodzinski, M. Neeman, L.O. Sillerud, S. Gottesfeld, *J. Phys. Chem.*, **95** (1991) 6040 .

[44] M.A. Modestino, D.K. Paul, S. Dishari, S.A. Petrina, F.I. Allen, M.A. Hickner, K. Karan, R.A. Segalman, A.Z. Weber, *Macromolecules*, **46** (2013) 867 .

[45] H. Xu, H.R. Kunz, J.M. Fenton, *Electrochim. Acta*, **52** (2007) 3525 .

[46] Y. Ono, T. Mashio, S. Takaichi, A. Ohma, H. Kanesaka, K. Shinohara, *ECS Trans.*, **28** (2010) 69 .

[47] S. Jomori, N. Nonoyama, T. Yoshida, *J. Power Sources*, **215** (2012) 18 .

[48] K. Kudo, Y. Morimoto, *Meeting Abstracts of Electrochemical society*, MA2012-02 (2012) 1270 .

[49] P.J. Ferreira, G.J. la O', Y. Shao-Horn, D. Morgan, R. Makharia, S. Kocha, H.A. Gasteiger, *J. Electrochem. Soc.*, **152** (2005) A2256 .

[50] T. Nagai, H. Murata, Y. Morimoto, *J. Electrochem. Soc.*, **161** (2014) F789 .

[51] C. Lim, L. Ghassemzadeh, F. Van Hove, M. Lauritzen, J. Kolodziej, G.G. Wang, S. Holdcroft, E. Kjeang, *J. Power Sources*, **257** (2014) 102 .

[52] S.S. Zhang, X.Z. Yuan, R. Hiesgen, K.A. Friedrich, H.J. Wang, M. Schulze, A. Haug, H. Li, *J. Power Sources*, **205** (2012) 290 .

[53] X.Y. Huang, R. Solasi, Y. Zou, M. Feshler, K. Reifsnider, D. Condit, S. Burlatsky, T. Madden, *J. Polym. Sci. Pt. B-Polym. Phys.*, **44** (2006) 2346 .

[54] N.M. Markovic, P.N. Ross, *Surf. Sci. Rep.*, **45** (2002) 121 .

[55] R. Subbaraman, D. Strmcnik, V. Stamenkovic, N.M. Markovic, *J. Phys. Chem. C*, **114** (2010) 8414 .

[56] R. Subbaraman, D. Strmcnik, A.P. Paulikas, V.R. Stamenkovic, N.M. Markovic, *ChemPhysChem*, **11** (2010) 2825 .

[57] M. Ahmed, D. Morgan, G.A. Attard, E. Wright, D. Thompsett, J. Sharman, *J. Phys. Chem. C*, **115** (2011) 17020 .

[58] K. Kodama, R. Jinnouchi, T. Suzuki, H. Murata, T. Hatanaka, Y. Morimoto, *Electrochem. Commun.*, **36** (2013) 26 .

[59] K. Kodama, A. Shinohara, N. Hasegawa, K. Shinozaki, R. Jinnouchi, T. Suzuki, T. Hatanaka, Y. Morimoto, *J. Electrochem. Soc.*, **161** (2014) F649 .

[60] H.A. Gasteiger, S.S. Kocha, B. Sompalli, F.T. Wagner, *Appl. Catal., B*, **56** (2005) 9 .

[61] A.J. Bard, L.R. Faulkner, *Electrochmical methods, Fundamentals and Applications, 2nd ed., Wiley*, (2001) .

[62] K. Kodama, R. Jinnouchi, T. Suzuki, T. Hatanaka, Y. Morimoto, *Electrochim. Acta*, **78** (2012) 592 .

[63] D. Strmcnik, K. Kodama, D. van der Vliet, J. Greeley, V.R. Stamenkovic, N.M. Markovic, *Nat. Chem.*, **1** (2009) 466 .

[64] D. Strmcnik, D.F. van der Vliet, K.C. Chang, V. Komanicky, K. Kodama, H. You, V.R. Stamenkovic, N.M. Markovic, *J. Phys. Chem. Lett.*, **2** (2011) 2733 .

[65] K. Kodama, Y. Morimoto, D.S. Strmcnik, N.M. Markovic, *Electrochim. Acta*, **152** (2015) 38 .

Chapter 2

Experimentals and fundamentals of analyses

The works in this thesis are mainly based on voltammetric measurements and analyses. Fundamentals and backgrounds of the analyses are presented in this chapter. Further details of experiments are described in each chapters.

2.1 Electrochemical cell

A glass or Teflon electrochemical cell with conventional three-electrode design was used in the present study. A water-jacketed glass cell used in this study is shown in Fig. 2.1.1.

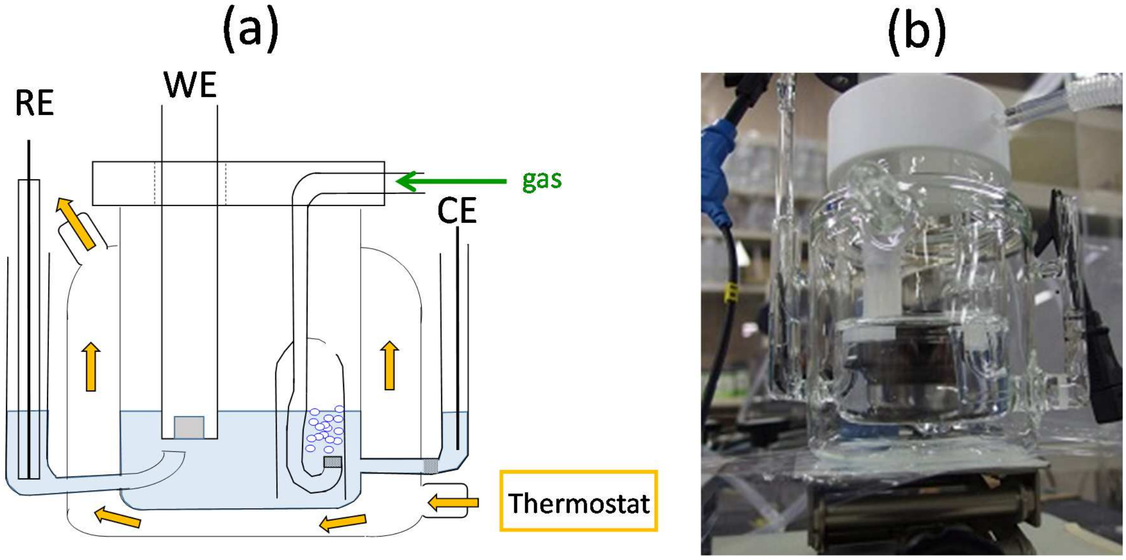

Fig. 2.1.1 (a) Illustration of the three-electrode cell with a water jacket used in the present study. RE: reference electrode, WE: working electrode, CE: counter electrode. The temperature of the electrolyte (light-blue shaded part) can be controlled by flowing water with the thermostat circulator (yellow arrows). (b) Photograph of the cell.

A single-crystalline Pt electrode with (100) or (111) orientation was used as the working electrode (WE). The counter electrode was a Pt or Au wire. Reference electrode (RE) used was either a reversible hydrogen electrode (RHE) or a commercial Ag/AgCl(saturated KCl) which was separated from the bulk solution with a Ruggin capillary placed close to the WE to reduce the cell resistance. The RHE was a platinized Pt mesh contacted with both *ca*. 1 atm of hydrogen and the electrolyte in a hydrogen-reserved glass tube. The Ag/AgCl was connected to the cell via a bridge with a valve to prevent the electrolyte from contamination of chloride anion. The potential of the Ag/AgCl was calibrated to the RHE scale by measuring its potential against the RHE in each measurement and the potential of WE is always described in the RHE scale in the present study. A potentiostat (Autolab, Metrohm Autolab, The Netherlamds) was used in recording cyclic voltammograms, in which the ohmic loss in the electrolyte was always calibrated (“IR-corrected”) by specifying the cell-resistance using the function of “positive feedback” equipped in the potentiostat.

All the parts of the cell were made of glass or Teflon, and cleansed by immersing them in a mixed acid (the mixture of nitric acid (60%) and sulfuric acid (98%) with the volume ratio of 1/1) at room temperature for a couple of hours and subsequently boiling them in Milli-Q water (three times). In the measurements using alkaline electrolytes, all the cell parts were made of Teflon to avoid the corrosion of glass in alkaline [1].

2.2 Preparation of single crystal electrode

In the study of electrocatalytic properties, analyses with single-facet (hkl) electrodes give a plenty of information because of their defined crystallographic sites, although multi-facet catalysts (e.g. nanoparticles) are used for real PEFCs. For example, the difference in electrochemical properties among various facets can be seen in the shape of cyclic voltammogram (CV) under inert condition as shown in Fig. 2.2.1 [2].

A single-facet Pt electrode can be prepared by cutting a bulk Pt single crystal with a suitable orientation. The method of the electrode preparation and transfer to an electrochemical system has been successfully established by Clavilier and co-workers [3]. In the present experiments, however, disks of Pt single crystals were purchased from a manufacturer (MaTecK) and repeatedly used by reproducing the (hkl) surfaces using an electromagnetic-inductive heating system shown in Fig. 2.2.2.

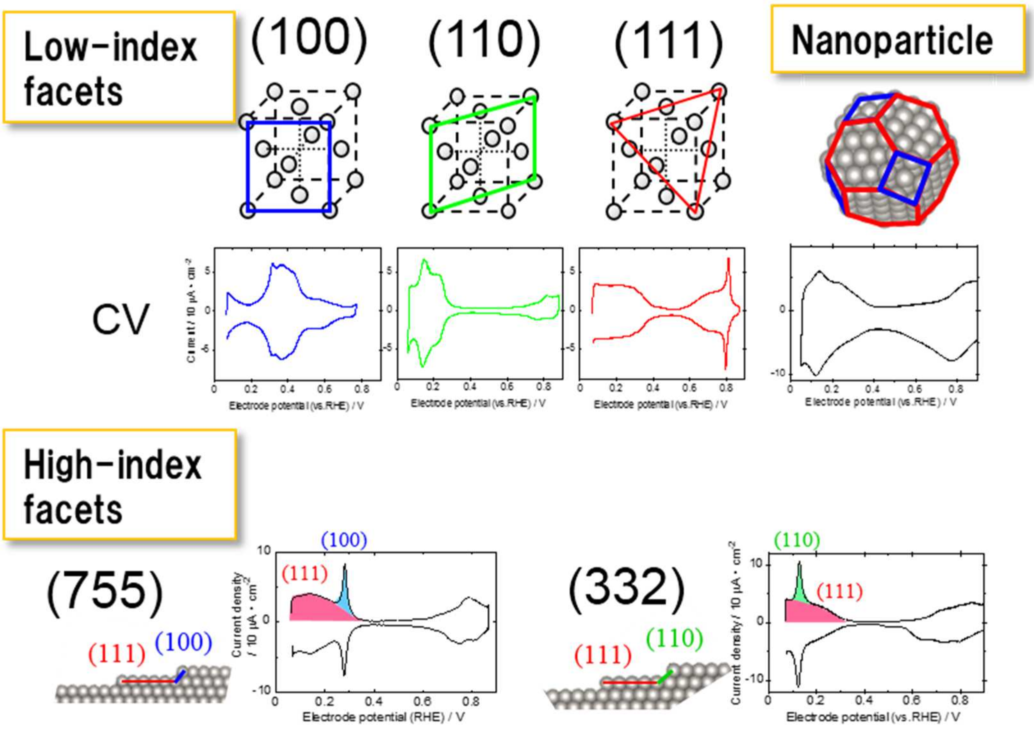

Fig. 2.2.1 The shapes of the cyclic voltammograms under inert condition of the three low-index facets, nanoparticles, and high index facets of (755) and (332) for Pt electrode. The assignments of peaks and interpretation of CV for Pt nanoparticles have been discussed by Feliu and co-workers [2].

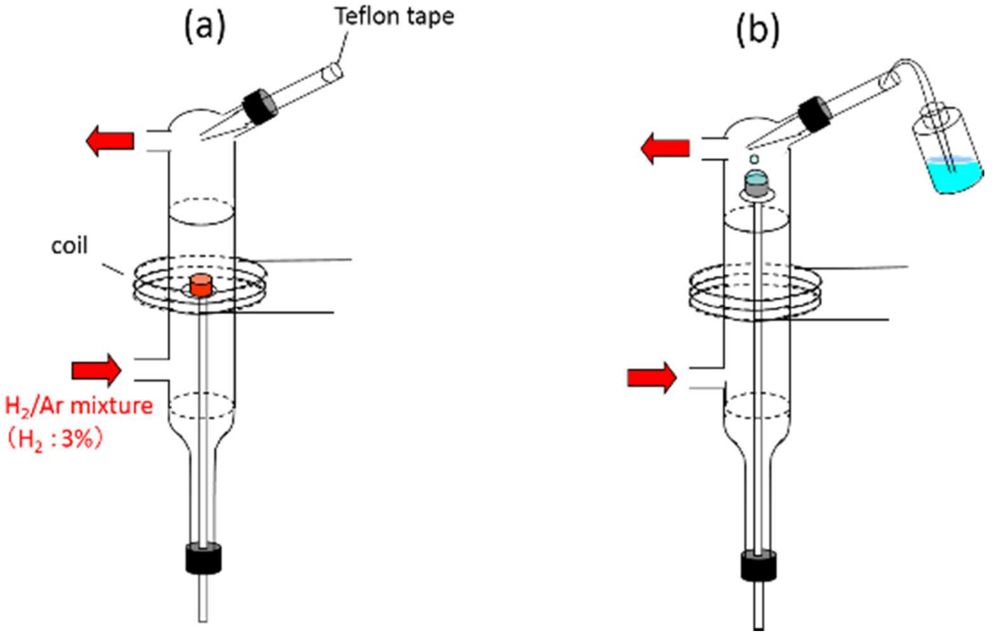

Fig. 2.2.2 The electrode preparation system with electromagnetic inductive heating. (a) The configuration of the system during the heating. The temperature is heated up to 1200 – 1650 K. (b) The method for protecting the electrode surface from contaminations; before the exposure of the Pt single crystal to atmosphere, the electrode surface is covered with a droplet of water.

Thus prepared electrode was assembled into the holder for a rotating disk electrode (RDE) system (ASR or MSR, PINE Instrument Company, The U.S.) [4], and then transferred to the electrochemical cell while the (hkl) surface is covered with a droplet of water (Milli-Q, 18.2 MΩ) to prevent its contamination in the air. There are two configurations for the electrode assembling: embedded form (Fig.2.2.3a) [5] and "hanging meniscus" form (HM-RDE, Fig. 2.2.3b) [6]. The former is hydrodynamically more ideal, and less susceptible to the wetting of the side surface, which leads to mixing of unconcerned currents from other facets with the current from the concerned (hkl) surface. Therefore, the configuration of the embedded form was applied as far as possible in the present study. The embedding procedure is described in Fig.2.2.4. However, HM-RDE was applied in the

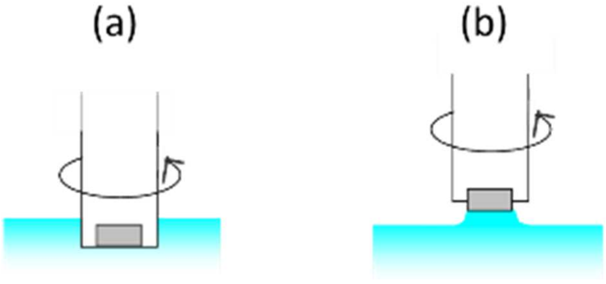

Fig. 2.2.3 The configurations of the (a) embedded form of RDE and (b) HM-RDE.

Fig.2.2.4 Schematics of the embedding of an electrode into an RDE assembly.

measurements with ionomer coatings (Chapter 5) because the ionomer films were found to be scraped during the embedding (Appendix B), and no problems were found with regard to the hydrodynamics and side-wetting.

2.3 Analysis of kinetics

The effect of electrode potential on electrochemical reactions can be understood in terms of the transition state theory [4]. Fig.2.3.1 shows the change in energy diagram along the reaction coordinate for a process of "O + e^- → R" for a change in electrode potential of ΔE (see the change from curve A to curve B) and the characteristics can be described as follows. (i) The energy for the reactant system is changed by $-F\Delta E$, where F is the Faraday constant, because the system includes one electron in the phase of electrode. (ii) Because the electron is not completely transferred to the oxidant O in the transition state (TS), the energy for the TS is also changed by a certain fraction of $-F\Delta E$, $-\alpha F\Delta E$, where α is called the symmetry factor. (iii) Therefore, the activation energy, ΔG^*, is changed by $(1-\alpha)F\Delta E$ and the reaction rate is changed by a factor of $\exp(-\frac{(1-\alpha)F\Delta E}{RT})$ at the temperature T, where R is the gas constant.

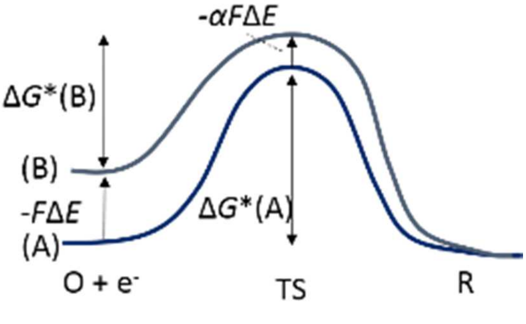

Fig. 2.3.1 Change in energy diagram along the reaction coordinate for a process of "O + e^- → R" with the change in electrode potential of ΔE; the energy diagram is changed from (A) to (B). ΔG^*(A) and ΔG^*(B) correspond to the activation energies for the curves of (A) and (B), respectively.

This consideration leads to the well-known Tafel equation in the potential region where the rate of the backward reaction is much smaller than that of the forward one and therefore negligible:

$$i(E) = i_0 \exp\left(-\frac{(1-\alpha)F\eta}{RT}\right) \qquad (2.3.1)$$

or

$$\eta = \frac{2.3RT}{(1-\alpha)F}\log|i_0| - \frac{2.3RT}{(1-\alpha)F}\log|i(E)| \qquad (2.3.2)$$

$$(\eta = E - E_0)$$

, where $i(E)$ is the current density for the reaction at the electrode potential of E, i_0 is the exchange current density, which is the forward or backward reaction current density at the equilibrium potential E_0, and η is called overpotential. The so-called Tafel plot, η vs $\log|i(E)|$, provides α from its slope and is therefore, a useful tool for analyzing reaction mechanisms as applied in several parts in this thesis.

2.4 References

[1] K.J.J. Mayrhofer, G.K.H. Wiberg, M. Arenz, *J. Electrochem. Soc.*, **155** (2008) P1 .

[2] J. Solla-Gullon, P. Rodriguez, E. Herrero, A. Aldaz, J.M. Feliu, *Phys. Chem. Chem. Phys.*, **10** (2008) 1359 .

[3] J. Clavilier, D. Armand, S.G. Sun, M. Petit, *J. Electroanal. Chem.*, **205** (1986) 267 .

[4] A.J. Bard, L.R. Faulkner, *Electrochmical methods, Fundamentals and Applications, 2nd ed.*, Wiley, (2001)

[5] N.M. Markovic, H.A. Gasteiger, P.N. Ross, *J. Phys. Chem.*, **99** (1995) 3411 .

[6] B.D. Cahan, H.M. Villullas, *J. Electroanal. Chem.*, **307** (1991) 263 .

Chapter 3

Kinetics of fundamental reactions on platinum electrode

Pt oxides, which are inevitably formed on cathode catalyst as far as water is present, are one of the most major reaction-blocking species for ORR. Their formation kinetics and role in ORR are discussed in this chapter.

3.1 Oxide formation

In a PEFC, the cathode is held in a high electrode potential range (above 1.0 V (RHE)) at which Pt oxides are formed on the catalyst surfaces. Pt oxides play key roles for both the activity and durability of the catalyst; the oxides block the site for oxygen reduction reaction [1-3] but protect subjacent Pt atoms from dissolution [4]. Therefore, the amount of Pt oxides needs to be adequately controlled during the operation of fuel cells.

For understanding the formation and reduction of Pt oxides, Pt single-crystals are useful as the model because the oxidation site is well-defined. Among the low-index planes, (111) has most widely been used in previous studies [3, 5-11].

Figure 3.1.1a shows the cyclic voltammogram (CV) of a Pt (111) single crystal in deaerated 0.1 M $HClO_4$. Three redox peaks are seen: the reversible flat peak between 0.05 – 0.4 V due to the oxidative desorption and reductive adsorption of underpotentially deposited hydrogen (H_{UPD}) [12, 13], the reversible butterfly-shaped peak between 0.6 - 0.9 V assigned to the oxidative adsorption and reductive desorption of hydroxyl (OH(ads)) [5, 6, 8, 10-14], and the irreversible peak between 0.8 – 1.1 V, shown as O*, assigned to the formation and reduction of Pt oxide [5, 7, 8]. Since the latter two peaks, OH(ads) and O*, are well separated, the two formation and reduction processes can be separately analyzed, whereas this is not the case for other planes and polycrystalline surfaces (Fig.3.1.1b).

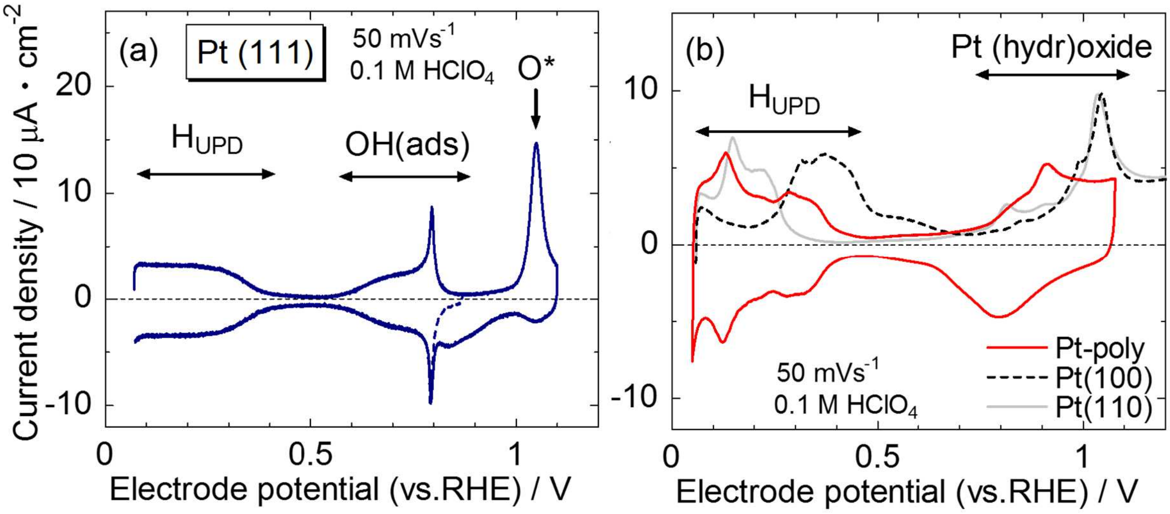

Fig. 3.1.1 (a) CVs for Pt (111) surface in deaerated 0.1 M $HClO_4$ for the upper limit of 1.1 V (solid line) and 0.87 V (dashed line). (b) CV for Pt-poly and anodic voltammograms for Pt (100) and Pt (110) in deaerated 0.1 M $HClO_4$.

For the structure of the Pt hydroxide (OH(ads)), it is widely agreed that hydroxyls are adsorbed on the surface, not incorporated into the subsurface. For the structure of the oxide, however, two microscopic views have been proposed. Nagy *et al.* suggested a “place-exchanged” structure (“subsurface oxide”) in which oxygen atoms are incorporated into the subsurface of the electrode from X-ray scattering (XRS) experiments [7]. On the other hand, Wakisaka *et al.* concluded the oxide as the state where oxygen atoms are adsorbed on the surface (O(ads)) from X-ray photoelectron spectroscopic (XPS) analysis and scanning tunneling microscopy (STM) observation [8, 9]. In addition to the structure, reaction mechanisms of the formation and reduction of the oxide have not been understood well even for the simplest surface (i.e., Pt(111)) either and there still remain following questions;. (i) is the reaction formula $Pt + H_2O \rightarrow PtO + 2\ H^+ + 2\ e^-$ or $PtOH \rightarrow PtO + H^+ + e^-$?; (ii) what will be the reason of the irreversibility of the O* peak?; and (iii) is the reaction totally kinetic or including other effects such as magnetic hysteresis proposed by Conway [15]?

As the first approach to these issues, kinetics of the oxide formation is studied on a Pt (111) surface in this section.

3.1.1 Experimental

Electrode preparation

A Pt (111) surfaced single crystal disk (99.99%, 0.196 cm^2, MaTecK) was annealed using electromagnetic inductive heating for 10 minutes at approximately 1300 K in the flow of a mixture of H_2 and Ar (3 % H_2, Taiyo Nippon Sanso, the purity of each gas: H_2: 99.99999%, Ar: 99.999%) [16]. The annealed specimen was cooled slowly to room temperature in the flow of the same gas mixture. Afterward the Pt (111) surface was covered with a droplet of water (Milli-Q, 18.2 MΩ) and then immersed in 0.1 M $HClO_4$ (MERCK, Suprapur) saturated with Ar (Taiyo Nippon Sanso, 99.999%) at 0.07 V.

Electrochemical procedures

The electrode potential was anodically scanned from 0.07 V to 0.98 – 1.02 V (at an interval of 0.01 V) at 50 mV s^{-1}, then held at the potential for 1 – 130 s and then cathodically scanned to 0.07 V at 50 mV s^{-1}. The amount of the oxide formed during the potential hold is estimated from the charge, q_{O*}, that flows in cathodic linear sweep voltammogram as a function of the potential holding time and the hold potential. The current density of the oxide formation is estimated from the time-differential of the q_{O*} vs. potential holding time curve. This method is essentially the same as that used by Vetter et al. [17] to examine the formation and reduction of Pt oxide, but they applied the method to a polycrystalline Pt, not a Pt single crystal, and therefore, could not identify the type of the formed oxide (OH(ads) or O*). As described in the following sections, the application of a Pt (111) single crystal electrode in the present study enabled detailed analyses of the mechanisms of Pt-oxide formation through comparisons between past observations using various non-voltammetric methods and the present results.

While the measurement was not being conducted (standby state), the electrode potential was being held at 0.07 V. The temperature was 303 K.

3.1.2 Results

Voltammogram with potential hold

Fig. 3.1.2 shows the voltammograms before and after the potential holds at 1.00 V for 0 (no hold), 10, 30 and 100 s. The reduction of the oxide is seen above 0.8 V in the cathodic scans.

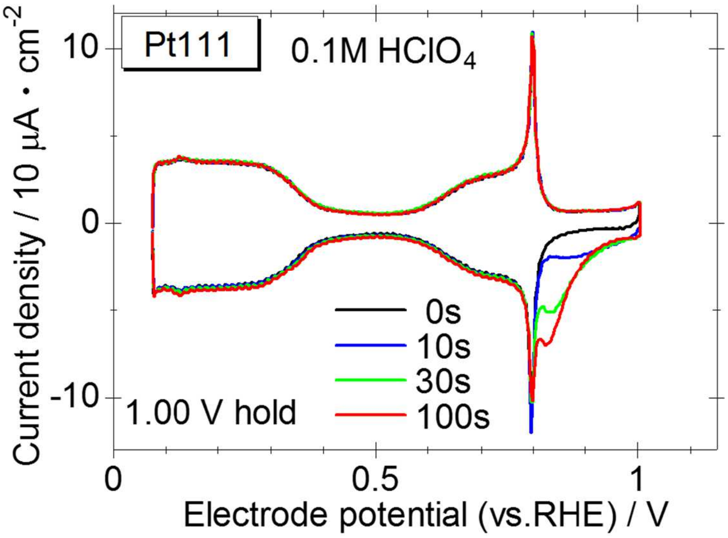

Fig. 3.1.2 The voltammograms before and after the potential holds at 1.00 V for 0 s (no hold) (black), 10 s (blue), 30 s (green) and 100 s (red).

Calculation of oxide amount

The amount of the oxide was estimated, as shown in Fig. 3.1.3, by subtracting the reductive charge of a voltammogram where only OH(ads) is formed, from that where both OH(ads) and the oxide are formed. As the former voltammogram, the one with the upper limit of 0.98 V without a potential hold ("background voltammogram") was chosen.

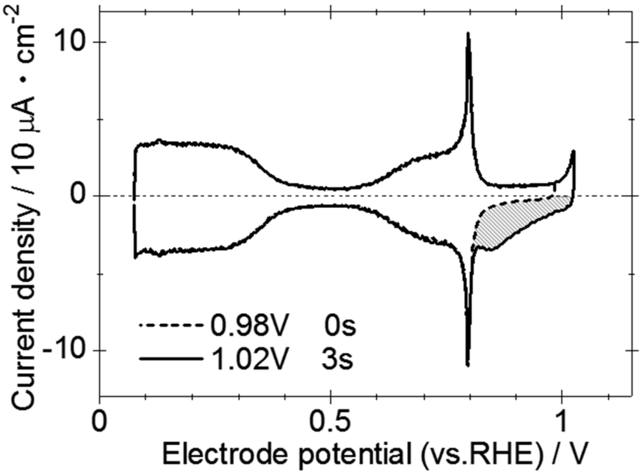

Fig. 3.1.3 The schematic of the estimation of the oxide amount, which corresponds to the shaded area.

Oxide amount vs holding time

Fig. 3.1.4 shows the oxide amount as a function of the potential holding time for each hold potential. The electric charge q_{O^*}, instead of surface coverage, was chosen as an indicator of the oxide amount, because the coverage cannot be determined unless otherwise the reaction mechanism is clarified.

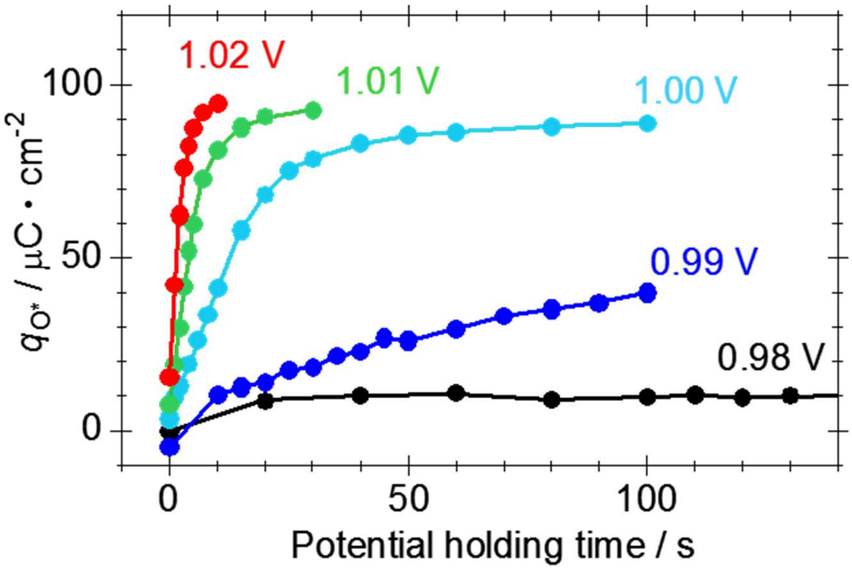

Fig. 3.1.4 The oxide amount as a function of the potential holding time for each hold potential. Black: 0.98 V, blue: 0.99 V, light blue: 1.00 V, green: 1.01 V, red: 1.02 V.

At 0.98 V, the oxide is formed quickly but does not grow further beyond 10 μC·cm^{-2}, which equals to 0.042 ML (monolayer) if the reaction is the one electron process and 0.021 ML if it is the two electron process. At 0.99 V, the oxide steadily grows up to 100 s (The behavior over 100 s has not yet been examined.). At 1.00 V or higher, the oxide grows faster and reaches its seemingly maximum value of approximately 100 μC·cm^{-2}, which equals to 0.42 ML for the one electron process and 0.21 ML for the two electron process.

Fig. 3.1.5 shows the logarithmic plot of Fig. 3.1.4. These S-shaped curves are in clear contrast to the behavior on a polycrystalline Pt, where the oxide amount increases linearly with the logarithm of the potential holding time over the range between 10^{-2} and 10^{3} s [17-19].

Current density for oxide formation reaction

The oxide formation current densities, in principle, can be obtained by differentiating the oxide growth curves of Fig. 3.1.4 with time. To enable differentiation at any point, continuous smooth curves were obtained using the least square fittings for several local plots close to the differentiating points by cubic functions of the logarithm of the potential holding time. Examples of the estimation procedure is shown in Fig.3.1.6; the locally fitted curves are shown as solid lines and the current densities at the oxide amount of 60 μC·cm^{-2} are equal to the slopes of the tangents (dashed lines).

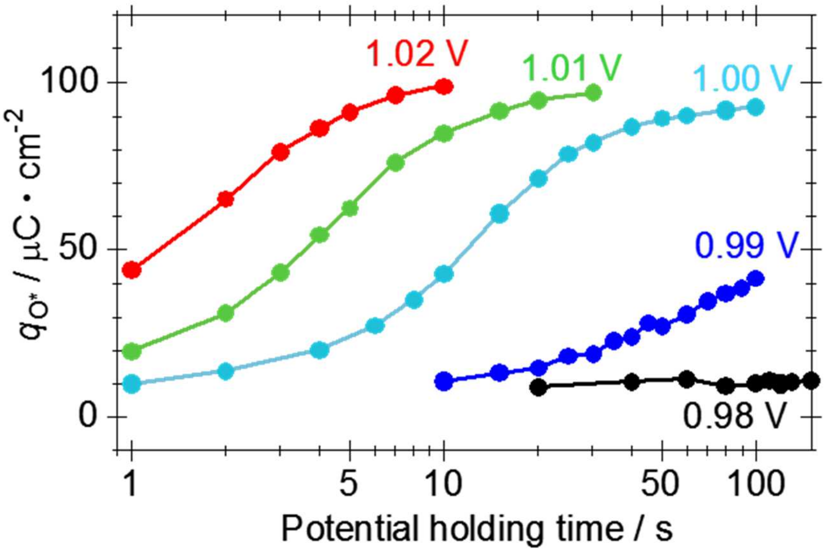

Fig. 3.1.5 The logarithmic plot of Fig. 4.

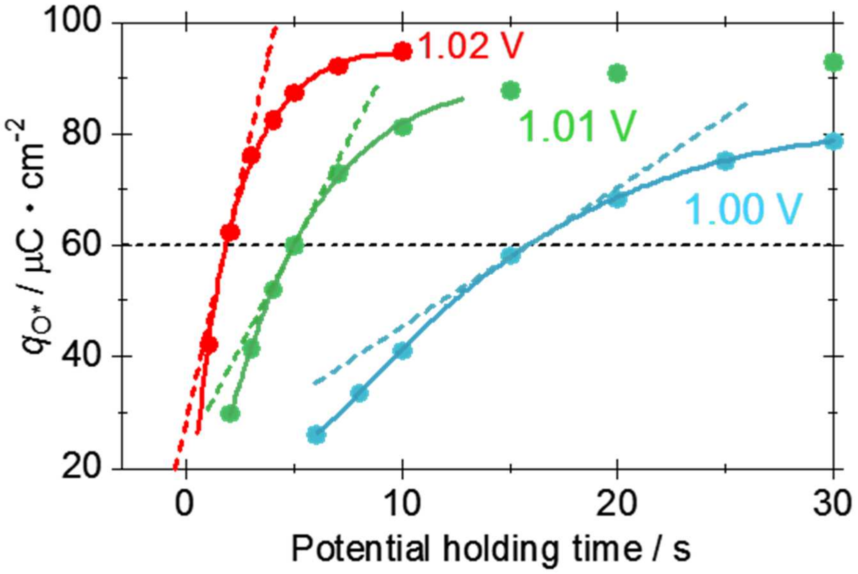

Fig. 3.1.6 The estimation procedure for the oxide formation current densities at the oxide amount of 60 µC·cm^{-2}. Solid lines: the locally fitted curves. Dashed lines: the tangents at 60 µC·cm^{-2} whose slopes are equal to the oxide formation current densities: 2.5, 7.4 and 17 µA·cm^{-2} at the electrode potentials of 1.00, 1.01 and 1.02 V.

Tafel plot

The potential dependency of the oxide formation current density was estimated at several oxide amounts. Fig. 3.1.7 shows the Tafel plots (the electrode potential *vs*. the logarithm of the current density) and their fitted straight lines at 50, 60, 70 and 80 µCcm^{-2}. The plots are well on the straight lines and hence, the reaction current density is well expressed by the Tafel equation:

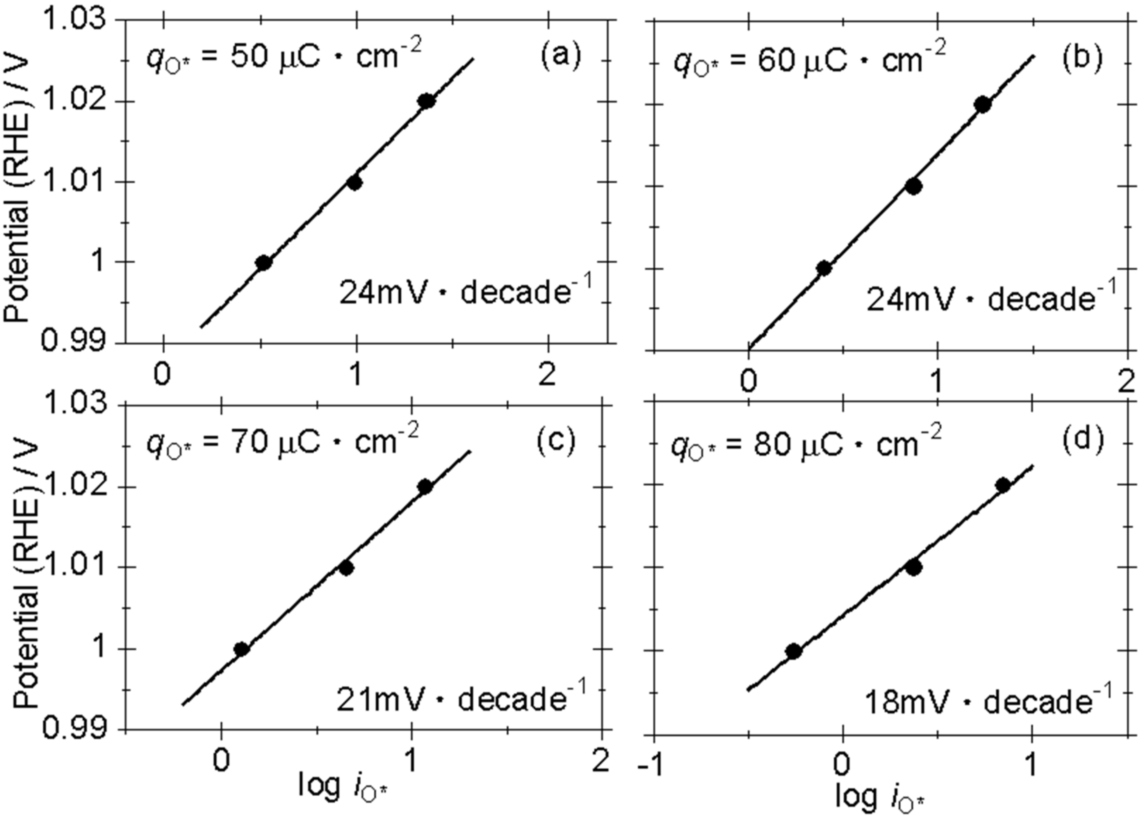

Fig. 3.1.7 Tafel plots for the oxide formation and their fitted straight lines at (a) 50, (b) 60, (c) 70 and (d) 80 μC·cm^{-2}.

$$i = i_0 \exp\left(\frac{\alpha F \eta}{RT}\right), \tag{3.1.1}$$

or

$$\eta = \frac{2.3RT}{\alpha F}\log i - \frac{2.3RT}{\alpha F}\log i_0 \quad , \tag{3.1.2}$$

where i is the reaction current density, i_0 the exchange current density, α the symmetry factor, F the Faraday constant, η the overpotential, R the gas constant and T the absolute temperature. This result means that, if the oxide amounts are equal, the reaction rate can be expressed by the simple electrochemical rate equation and hence, the states of the oxides seem to be identical, independent of the oxide formation conditions. The Tafel slope for the oxide formation is 18 - 24 mV·decade^{-1}.

In contrast, the Tafel plots are not on a straight line for 30 and 40 μC·cm^{-2} as shown in Fig. 3.1.8 and thus, the above discussion is not valid. The invalidity is also seen in the cathodic linear sweep voltammograms, shown in Fig. 3.1.9; the profile of the oxide reduction clearly depends on the oxide formation conditions and thus so does the oxide state.

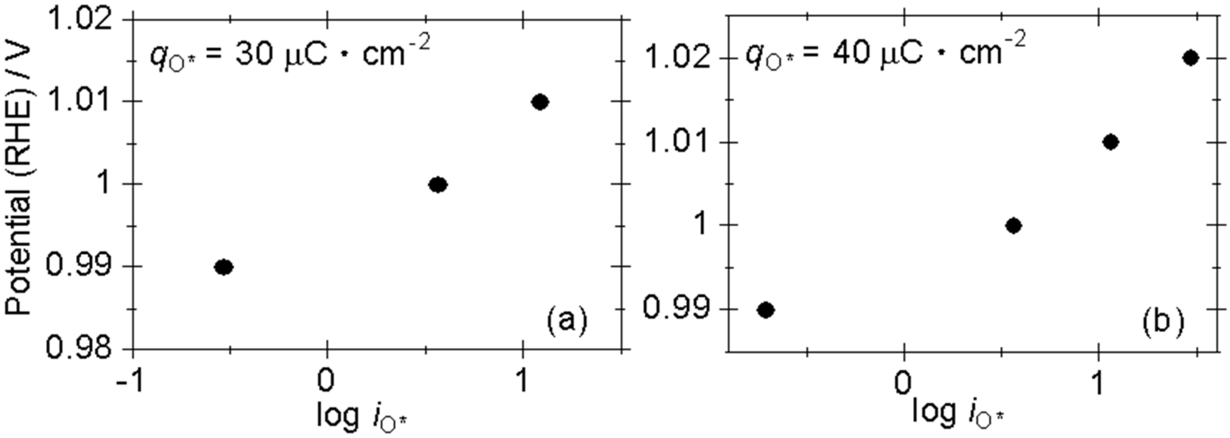

Fig. 3.1.8 Tafel plots for the oxide formation at (a) 30 and (b) 40 μC·cm^{-2}.

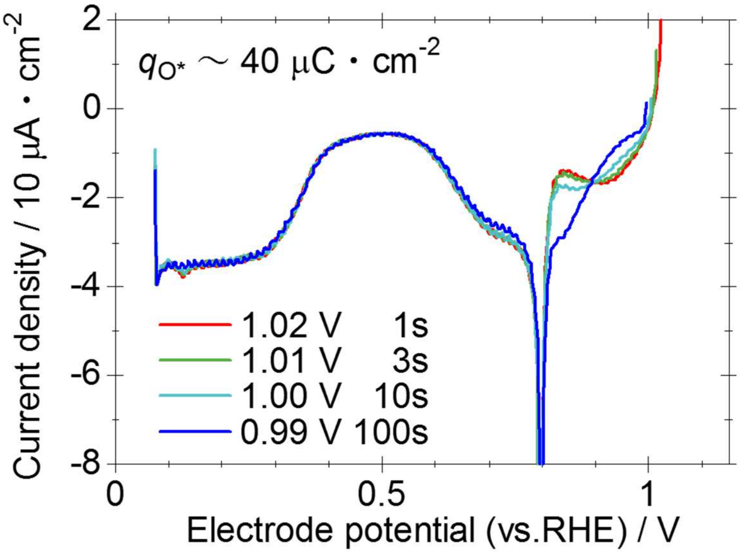

Fig. 3.1.9 The cathodic linear sweep voltammograms where q_{O*}'s are close to 40 μC·cm^{-2}. The hold potentials are 0.99 V (blue), 1.00 V (light blue), 1.01 V (green) and 1.02 V (red).

3.1.3 Discussion

The experimentally estimated Tafel slope of 18 - 24 mV·decade^{-1} is much smaller than that expected for one-step, one-electron transfer reactions:

$$\frac{\partial \eta}{\partial \log i} = \frac{2.3RT}{\alpha F} > 60\,\mathrm{mV \cdot decade^{-1}}, \tag{3.1.3}$$

for a symmetry factor of $0 < \alpha < 1$. A small Tafel slope, 36 mV·decade^{-1} was experimentally found also for a polycrystalline Pt by Vetter et al. [17, 20]. They ascribed the result to a subsurface oxidation by a place-exchange between a surface Pt atom and O(ads), the mechanism of which is explained as follows.

The surface Pt atom has a positive charge of Z_+, and O(ads) has a negative charge of Z_-. By the place-exchange, O(ads) moves from the top to the bottom of the inner Helmholtz layer, and the Pt atom moves from the bottom to the top of the inner Helmholtz layer. Therefore, the net electrostatic energy is decreased by $(Z_+ + |Z_-|) \cdot \Delta\varphi_\mathrm{i}$, where $\Delta\varphi_\mathrm{i}$ is the potential gap in the inner Helmholtz layer. By using the energy decrease due to the place-exchange, Vetter et al. described the oxide formation current density as

$$i \propto \exp\left(\frac{\alpha(Z_+ + |Z_-|)F}{RT} \Delta\varphi_\mathrm{i} \right). \tag{3.1.4}$$

In their experiment, $\Delta\varphi_i$ was linearly correlated to the electrode potential E using double layer capacitances [21], and as the result, the Tafel slope at a low oxide coverage was obtained as $2.3RT/\{\alpha F(Z_+ + |Z_-|)\}$. By assuming $Z_+ = |Z_-| = 2$ and $\alpha = 0.42$, the Tafel slope of 36 mV·decade^{-1} was reproduced.

The place-exchange model was also suggested by Conway et al [18]; a description of an oxide formation current density similar to Eq. 3.1.4 was used for explaining the “logarithmic law” for a polycrystalline Pt mentioned in Section 3.1.2 (the linear relation between the oxide amount and the logarithm of potential holding time). As mentioned in the introduction, Nagy *et al.* also suggested the place-exchange mechanism for the oxide formation on a Pt(111) single crystal [7]. Hence, the small Tafel slope in the present study may also be ascribed to the place-exchange mechanism.

However, analytical and theoretical studies suggest that in the low oxide coverage region treated in the present study, below 0.35 ML, subsurface oxides at a Pt(111) surface is unstable. Devarajan et al. concluded that, rather than the subsurface oxidation, oxide chain formation with buckling of the surface is more favorable below 0.75 ML from STM observation under ultrahigh vacuum (UHV) [22]. Hawkins et al. supported the experimental results using a density functional theory study [23]. As mentioned in the introduction, Wakisaka et al. characterized the oxide below 1.1 V as O(ads) in their XPS analysis and *in situ* STM observation [8, 9]. Hence, the applicability of the place-exchange model to the present study is questionable.

The small Tafel slope can also be theoretically elucidated without considering the subsurface oxides, if the oxidation reaction is described by a combination of a fast electron transfer step, and a following slow electron transfer or chemical step [24, 25] as

$$\text{Reactant} \underset{n'\text{e-}}{\overset{\text{Equilibrium}}{\leftrightarrow}} \text{Intermediate} \overset{\text{RDS}}{\rightarrow} \text{Product}.$$

In this case, the current density is described as

$$i \propto \exp\left(\frac{\alpha_\mathrm{rds} F\left(E - E_\mathrm{rds}^{0'}\right)}{RT} \right) \theta_\mathrm{I}^{\gamma} \quad , \tag{3.1.5}$$

where α_rds is the symmetry factor for the rate determining step (RDS), $E_\mathrm{rds}^{0'}$ the standard potential for the RDS, θ_I the coverage of the intermediate and γ the reaction order for the RDS. Because of the fast rates of the formation and reduction of the intermediate, the first step is assumed to be in equilibrium, and hence, the intermediate coverage can be described, using the Langmuir-type isotherm, as

$$\theta_{\mathrm{I}} = \frac{C_{\mathrm{R}} \exp\left(\dfrac{n' F\left(E - E_1^{0'}\right)}{RT}\right)}{1 + C_{\mathrm{R}} \exp\left(\dfrac{n' F\left(E - E_1^{0'}\right)}{RT}\right)} \quad , \qquad (3.1.6)$$

where C_{R} is the concentration of the reactant (or the coverage if it is an adsorbate), n' the stoichiometric number of the electron for the first step and $E_1^{0'}$ the standard potential for the first step. By substituting Eq. 3.1.6 into Eq. 3.1.5, the current density can be rewritten as

$$i \propto \frac{C_{\mathrm{R}}{}^{\gamma} \exp\left(\dfrac{\left(n'\gamma + \alpha_{\mathrm{rds}}\right)FE - n'\gamma F E_1^{0'} - \alpha_{\mathrm{rds}} F E_{\mathrm{rds}}^{0'}}{RT}\right)}{\left(1 + C_{\mathrm{R}} \exp\left(\dfrac{n' F\left(E - E_1^{0'}\right)}{RT}\right)\right)^{\gamma}} \quad . \qquad (3.1.7)$$

When $C_{\mathrm{R}}\exp(n'F(E - E_1^{0'})/RT)$<<1 (the coverage of the intermediate is small),

$$i \propto C_{\mathrm{R}}{}^{\gamma} \exp\left(\frac{\left(n'\gamma + \alpha_{\mathrm{rds}}\right)FE - n'\gamma F E_1^{0'} - \alpha_{\mathrm{rds}} F E_{\mathrm{rds}}^{0'}}{RT}\right) \quad . \qquad (3.1.8)$$

Hence, the Tafel slope,

$$\frac{\partial E}{\partial \log i} = \frac{2.3RT}{\left(n'\gamma + \alpha_{\mathrm{rds}}\right)F} \quad , \qquad (3.1.9)$$

can be much smaller than 60 mV·decade^{-1}. (If the RDS is a chemical process, the exponential term in Eq. 3.1.5 is unity and the following equations are valid by setting α_{rds}=0.) This description can be qualitatively understood as the addition of the potential dependency to the concentration term in the rate equation for the RDS and it has been suggested for an iron corrosion reaction (the Bockris mechanism) [24, 25].

Testing of this hypothesis including the identification of the reactants and intermediates needs further experimental investigations and support from first principles calculations. These are beyond the scope of the present study and will be addressed in the near future.

3.1.4 Conclusions

The kinetics of the electrochemical oxide formation on Pt(111) was examined using the voltammetric analysis. The current density of the oxide formation reaction was estimated as a function of the potential below the oxide coverage of 0.35 ML. Under the condition where the Tafel plot is on a straight line, the slope was 18 - 24 mV·decade^{-1}. This small Tafel slope is not likely to be elucidated by the place-exchange model, which has been proposed as the cause of the small Tafel slope for oxide formation on polycrystalline Pt, because the oxide coverage is too low to make subsurface oxides stable on Pt (111) as suggested in past studies. An alternative mechanism was proposed, in which the reaction is assumed as a combination of a fast electron transfer step and a following slow step. In this way, the sophisticated analyses using the well-defined Pt (111) single crystal led to the new suggestion.

3.2 Oxygen reduction reaction

In oxygen reduction reaction (ORR), oxygenated species are formed also as reaction intermediates. Understanding of the properties of the intermediates is important because their coverages determine the catalyst activity. Analyses of the properties of those species are, however, not as straightforward (the peak analysis in the previous section cannot be applied) as in the case in the dearated electrolyte treated in the previous section, because voltammograms with large faradaic ORR currents are featureless as shown in Fig. 3.2.1. In this section, another approach is presented for analyzing the oxygenated intermediates.

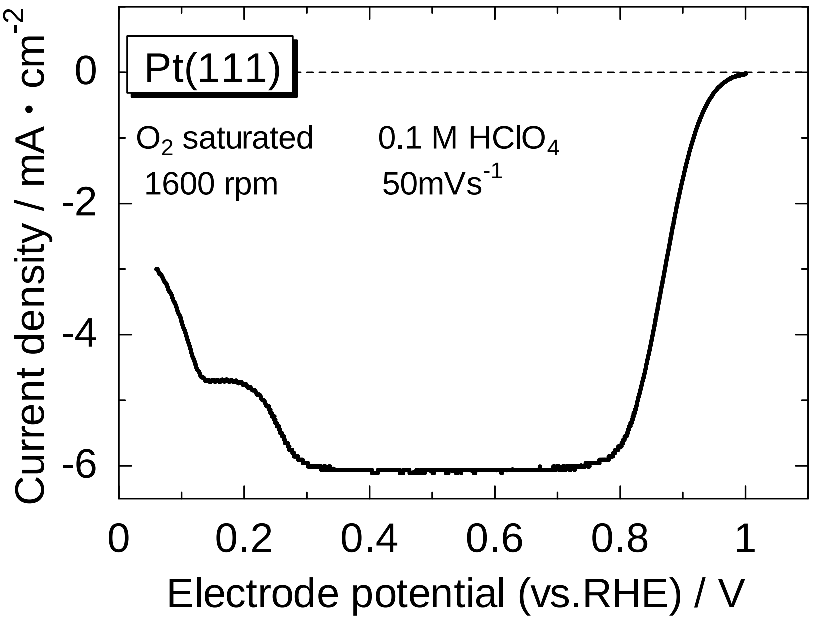

Fig. 3.2.1 The voltammogram on Pt (111) surface in 0.1 M $HClO_4$ saturated with O_2.

The focused physical quantity is reaction order of ORR, γ, the definition of which is described as

$$\gamma \equiv \left(\frac{\mathrm{d} \ln \dot{r}}{\mathrm{d} \ln C_\mathrm{S}} \right) \quad (3.2.1)$$

, where $\dot{r}$ is the ORR reaction rate and C_S is the concentration of O_2 at the electrode surface. The reaction rate, $\dot{r}$, can be described by considering the blocking effect (see Chapter 1);

$$\dot{r} = k\left(1 - \Theta_\mathrm{int} - \Theta_\mathrm{spec}\right)C_\mathrm{S} \quad (3.2.2)$$

where k is the reaction rate constant, Θ_int is the coverage of adsorbed reaction intermediate on the electrode surface, and Θ_spec is the coverage of adsorbed spectator species (*e.g.* electrolyte anions and impurities) [6].

If the removal of the intermediate is so fast that Θ_int is constant for any C_S, γ is 1. In contrast, if the removal of the intermediate is slow and Θ_{int} is increased with increasing of C_{S} (the intermediate is accumulated), γ is lower than 1. Thus, the reaction order provides information about the oxygenated intermediate. In this section, the reaction order for ORR on the model electrode of Pt (111) surface is experimentally estimated.

As shown by Eq. 3.2.1, the reaction order γ essentially describes the dependence of the reaction rate on the concentration of the reactant and, in principle, can be determined by measuring the reaction rate while controlling the reactant concentration on the reaction site. In reality, the reactant concentration on the reaction site is not equal to that in the bulk solution and depends on the reaction rate due to limited reactant transport to the reaction site and therefore experiments with controlled mass transport and data analysis for correcting the data are necessary.

Rotating disk electrode (RDE) technique is a well-established method for controlling the mass transport and its application to Pt single crystal electrodes was successfully accomplished by Markovic et al [26, 27]. Although the ORR reaction order on the model electrode of Pt (111) surface in acid electrolyte of 0.1 M $HClO_4$ has already been estimated at 0.8 V by Markovic et al. [26] and in a wider region of 0.8 – 0.95 V by Gómez-Marín et al. [28], a more sophisticated and systematic procedure is applied in the present study. In addition, the reaction order in alkaline solution, which has not yet been reported, is measured.

3.2.1 Experimental

Electrode preparation and electrochemical measurement

A Pt (111) surfaced single crystal disk with an electrode surface area of 0.283cm^2 was annealed using electromagnetic inductive heating for 5 minutes at approximately 1200 K in the flow of a mixture of H_2 and Ar (3 % H_2). The annealed specimen was cooled slowly to room temperature in the flow of the same gas mixture and covered with a droplet of water (Milli-Q, 18.2 MΩ). The electrode was then embedded into an RDE assembly. The detail of RDE assembling is described in Chapter 2 and in a previous paper [27].

Afterward the electrode was immersed in an acid (0.1 M $HClO_4$) or in an alkaline (0.1 M KOH) saturated with a mixture of O_2 and Ar at the electrode potential of 0.06 V (RHE), and then the potential was swept in the positive direction by 50 mVs^{-1} with the rotation rate of 1600 rpm. The recorded voltammograms are noted as ORR curves in the following. Cyclic voltammograms (CVs) were also measured with the scan rate of 50 mV·s^{-1} without the electrode rotation in the electrolytes saturated with Ar for checking the cleanness of the experimental system and measuring the background current. The potentials are always referred to RHE and ohmic drop was corrected.

$HClO_4$ was from JT baker (ULTREX II Ultrapure Reagent) and KOH from Alfa Aesar (99.99 % by metal basis). Gasses were from Airgas (99.9999 % for Ar, 99.999 % for O_2). A glass cell was used for the acid electrolyte and a Teflon (FEP) cell for the alkaline electrolyte. A gold wire was used for the counter electrode.

Data analysis

The detail of the data analysis is provided in Appendix A, which demonstrated that the reaction order γ can be estimated by the slope of the straight line fitted into a data set of $\ln i(E)$ *vs.* $\ln\{i_\mathrm{d}(1-i(E)/i_\mathrm{d})/i'_\mathrm{d}\}$ with various O_2 concentrations in the mixture, where $i(E)$ is the measured ORR current density at a certain electrode potential, E, and a certain O_2 bulk concentration, i_d is the diffusion limiting current density at the O_2 bulk concentration, and i'_d is the diffusion limiting current density in a standard bulk concentration of O_2, set at the saturated bulk concentration with 100 % O_2 in the present analysis, according to Eq. (3.2.3).

$$\ln i(E) = \gamma \ln\left\{\left(\frac{i_\mathrm{d}}{i'_\mathrm{d}}\right)\left(1-\frac{i(E)}{i_\mathrm{d}}\right)\right\} + A(E) \qquad (3.2.3)$$

where $A(E)$ is constant at the certain potential as described in the appendix A. i was obtained from the following equation.

$$i = i_\mathrm{LSV} - i_\mathrm{CV} \qquad (3.2.4)$$

where i_LSV is the current density of the ORR curve and i_CV is the current density of the CV in the positive scan, although this subtraction was found to have little effect on the results and conclusions in this study. The data set of $\ln i$ *vs.* $\ln\{i_\mathrm{d}(1-i/i_\mathrm{d})/i'_\mathrm{d}\}$ essentially describes the dependency of reaction rate on the concentration of the reactant at the electrode surface (not in the bulk) as described in the appendix A.

In past studies, similar plots of $\ln i$ *vs.* $\ln(1-i/i_\mathrm{d})$ obtained by changing electrode rotation rate under a constant bulk O_2 concentration have been mainly used for estimating the reaction order (The O_2 concentrations at the electrode surface can be also changed by changing the rotation speed) [26, 29]. This method is, however, susceptible to error because the O_2 concentrations at the electrode surface are always close to the setup bulk concentration and the plot range is narrow in the pure-kinetic potential region, where $i << i_\mathrm{d}$ and the consumption of the reactant at the electrode surface is slow (Fig. 3.2.2a). In contrast, our method using O_2/Ar mixtures with the same rotation speed, with which O_2 concentration at the electrode surface can be widely changed even in the pure-kinetic region (Fig. 3.2.2b), provides more reliable data.

Recently, Gómez-Marín et al. also applied the RDE technique with O_2/Ar gas mixtures and estimated the reaction order of ORR on Pt (111) surface [28] although their analytical procedure was different from ours. In their analysis, ORR currents were initially corrected for the mass-transport effect by assuming that $\gamma = 1$;

$$i_\mathrm{k}^{\gamma=1}(E) = \frac{i(E)i_\mathrm{d}}{i_\mathrm{d}-i(E)} \qquad (3.2.5).$$

Afterward the corrected ORR current, $i_{\mathrm{k}}^{\gamma=1}(E)$, which describes the current density if the concentration of O_2 at the electrode surface was equal to that in the bulk electrolyte and is the so-called kinetic current when $\gamma = 1$, was confirmed to be proportional to O_2 bulk concentration, and they concluded that $\gamma = 1$. While their conclusion is definitely self-consistent, the estimation procedure is only valid in the special case that $\gamma = 1$. In contrast, our procedure is valid for any γ since no assumption regarding γ was made in the derivation of Eq. 3.2.3.

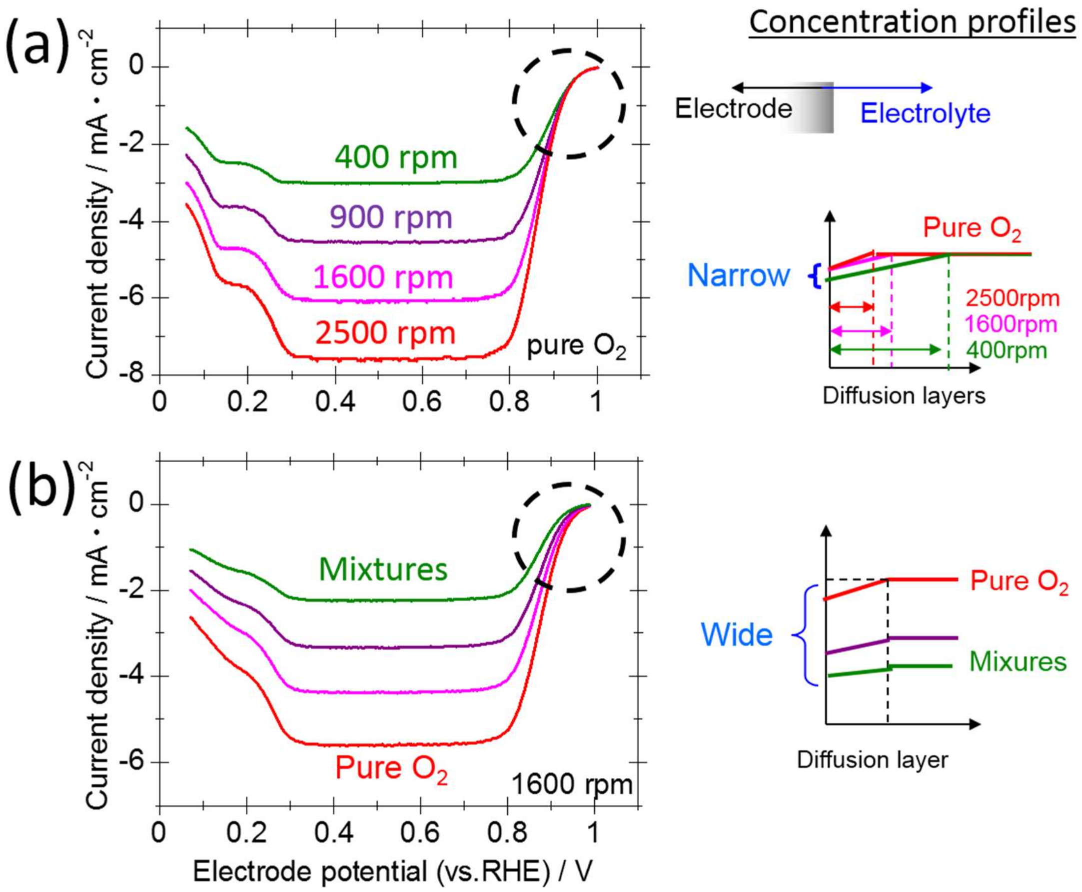

Fig. 3.2.2 ORR curves and concentration profiles of O_2 near the electrode surface with (a) pure O_2 with different rotation speeds and (b) O_2/Ar mixtures with different O_2 concentrations at the same rotation speed.

3.2.2 Results

CV and ORR curve

Figure 3.2.3 shows the CVs and ORR curves in 0.1 M $HClO_4$ and in 0.1 M KOH. Previous results were well reproduced for the CVs (Figure 3.2.3 (a) and (c)). Therefore, a well-defined Pt (111) surface is available and the experimental system is clean in our measurement.

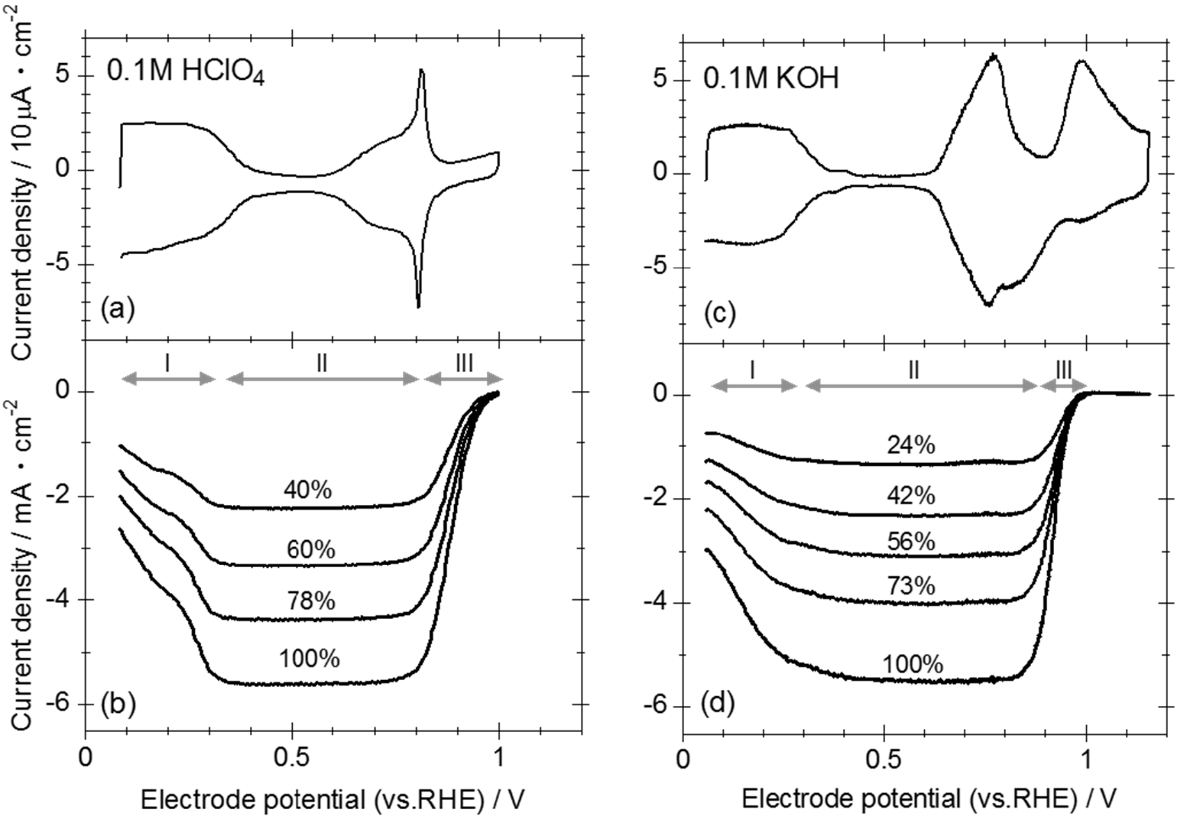

Fig. 3.2.3 (a) and (b): The CV and ORR curves (positive scan) on Pt(111) in 0.1 M $HClO_4$. (c) and (d): Those in 0.1 M KOH. The scan rate is 50mV s^{-1}. The electrode rotation rates are 0 rpm in CV and 1600 rpm in the ORR curves. Three potential regions I-III are visible (see the text for details). The analysis was conducted in the potential region III. The bulk concentrations of O_2 in the mixtures can be estimated from the diffusion limiting currents in the ORR curves and the resulting values are indicated in the figures.

Reaction order

Figure 3.2.4 shows typical plots of $\ln i$ *vs.* $\ln\{i_\mathrm{d}(1 - i/i_\mathrm{d})/i'_\mathrm{d}\}$ at 0.89 and 0.95 V with various O_2 partial pressures in 0.1 M $HClO_4$ and 0.1 M KOH and their fitted straight lines. The reaction order for each potential was estimated from the slopes.

Figure 3.2.5 shows the reaction orders of ORR as functions of the electrode potential in 0.1 M $HClO_4$ and 0.1 M KOH. The reaction order was estimated to be 1.1 in the acid electrolyte over the electrode potential region of 0.82 -0.96 V. It is unlikely that the reaction order of ORR exceeds 1.0 according to current theories for ORR, in which no more than one O_2 molecule participates in the reaction pathway [6, 30]. While further investigations are needed, the excess of 0.1 can be tentatively ascribed to the error in the analytical procedure despite the careful treatments described above. The reaction order in the alkaline is lower than that in the acid in the entire potential region and falls to minimum of approximately 0.5 at 0.95 V.

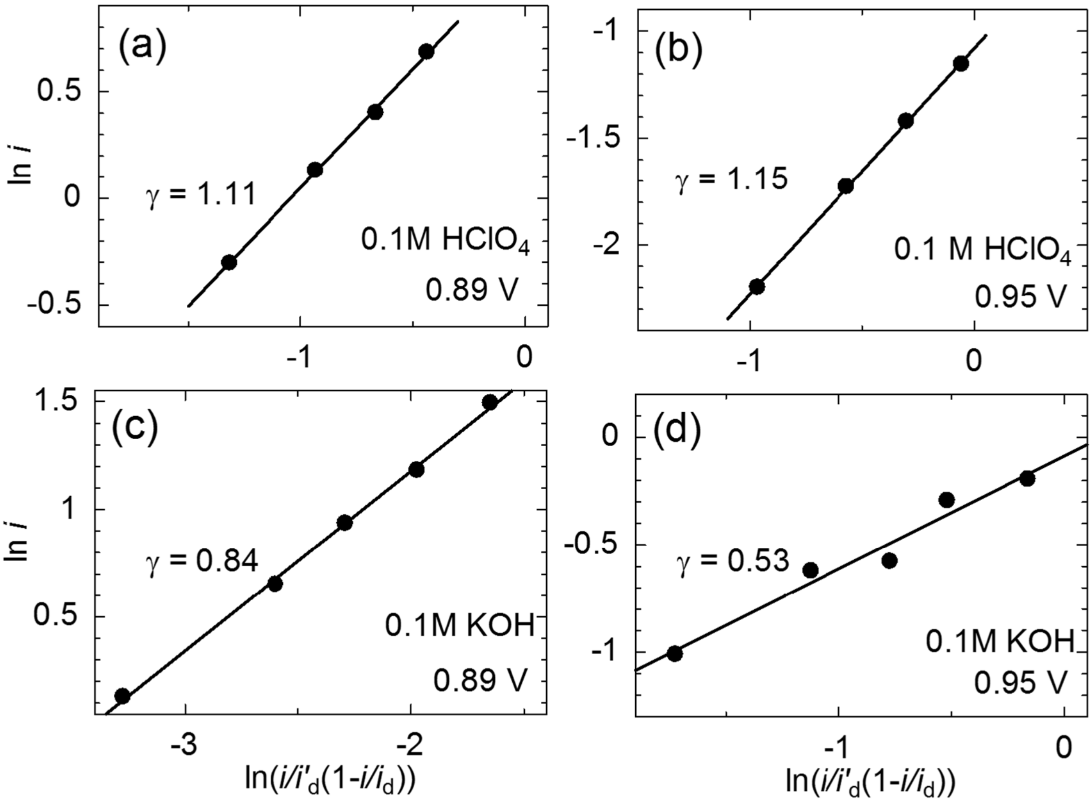

Fig. 3.2.4 Typical plots of $\ln i$ *vs.* $\ln\{i_d(1-i/i_d)/i'_d\}$. (a) The plots at 0.89 V in 0.1 M $HClO_4$, (b) those at 0.95 V in 0.1 M $HClO_4$, (c) those at 0.89 V in 0.1 M KOH and (d) those at 0.95 V in 0.1 M KOH.

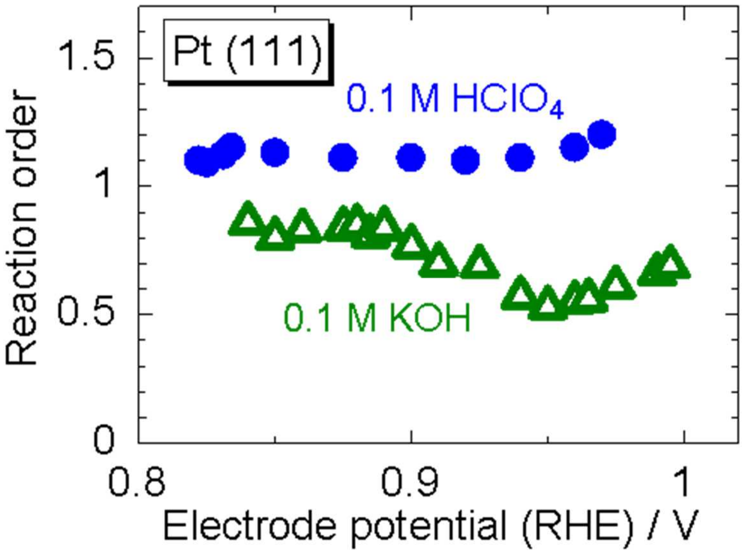

Fig. 3.2.5 The reaction orders of ORR on Pt (111) surface in 0.1 M $HClO_4$ and in 0.1 M KOH.

3.2.3 Discussion

The first-order kinetics in the acid electrolyte, which has been also shown in the two previous studies [26, 28], indicates that the reaction intermediates are not accumulated with the increase in O_2 concentration and the first step of O_2 adsorption in ORR pathway is RDS. Recently this mechanism was theoretically demonstrated by taking into account the reorganization of solvent at the interface for O_2 adsorption, which creates the additional barrier of 0.28 eV for the elementary step, by Hansen et al [30].

The reaction order significantly lower than 1 in the alkaline electrolyte indicates accumulation of intermediates. This result may be ascribed to different reaction mechanisms: e.g. different barrier for the solvent reorganization. There are few studies of ORR mechanisms in alkaline solution [31] and therefore, the origin of the small reaction order in alkaline is still open question.

While the unclear points are remaining, important information was obtained in this section. Since the oxygenated intermediates were found not to be accumulated with the increase in O_2 concentration in acid, the ORR kinetics can be discussed on the basis of knowledge of the spectator species (without considering the coverage of reaction intermediates) for PEFC with proton-exchange type.

3.2.4 Conclusions

The reaction order of ORR on a Pt(111) single crystal electrode was experimentally estimated as a function of the electrode potential in an acid and in an alkaline electrolytes with a more sophisticated way than previous studies. The reaction order is approximately 1 over the range of the electrode potential of 0.82 -0.96 V (RHE) in acid, while it is significantly lower than 1 in alkaline. The first-order kinetics in acid indicates that oxygenated species as intermediates are not accumulated with the increase in O_2 concentration and the ORR kinetics can be discussed on the basis of coverage with spectator species (including adsorbed anion and Pt oxide formed from water).

3.3 References

[1] A. Damjanovic, P. G. Hudson, *J. Electrochem. Soc.*, **135** (1988) 2269.

[2] H. A. Gasteiger, S. S. Kocha, B. Sompalli, F. T. Wagner, *Appl. Catal.*, *B*, **56** (2005) 9.

[3] V. R. Stamenkovic, B. Fowler, B. S. Mun, G. F. Wang, P. N. Ross, C. A. Lucas, N. M. Marković, *Science*, **315** (2007) 493.

[4] R. M. Darling, J. P. Meyers, *J. Electrochem. Soc.*, **152** (2005) A242.

[5] A. S. Bondarenko, I. E. L. Stephens, H. A. Hansen, F. J. Pérez-Alonso, V. Tripkovic, T. P. Johansson, J. Rossmeisl, J. K. Nørskov, I. Chorkendorff, *Langmuir*, **27** (2011) 2058.

[6] R. Jinnouchi, K. Kodama, T. Hatanaka, Y. Morimoto, *Phys. Chem. Chem. Phys.*, **13** (2011) 21070.

[7] Z. Nagy, H. You, *Electrochim. Acta*, **47** (2002) 3037.

[8] M. Wakisaka, H. Suzuki, S. Mitsui, H. Uchida, M. Watanabe, *Langmuir*, **25** (2009) 1897.

[9] M. Wakisaka, S. Asizawa, H. Uchida, M. Watanabe, *Phys. Chem. Chem. Phys.*, **12** (2010) 4184.

[10] A. Berná, V. Climent, J. M. Feliu, *Electrochem. Commun.*, **9** (2007) 2789.

[11] K. Aljaafgolze, D. M. Kolb, D. Scherson, *J. Electroanal. Chem.*, **200** (1986) 353.

[12] N. M. Marković, P. N. Ross, *Surf. Sci. Rep.*, **45** (2002) 121.

[13] K. J. P. Schouten, M. J. T. C. van der Niet, M. T. M. Koper, *Phys. Chem. Chem. Phys.*, **12** (2010) 15217.

[14] V. Rai, M. Aryanpour, H. Pitsch, *J. Phys. Chem. C*, **112** (2008) 9760.

[15] B. E. Conway, *Prog. Surf. Sci.*, **49** (1995) 331.

[16] D. S. Strmcnik, D. V. Tripkovic, D. van der Vliet, K. C. Chang, V. Komanicky, H. You, G. Karapetrov, J. Greeley, V. R. Stamenkovic, N. M. Marković, *J. Am. Chem. Soc.*, **130** (2008) 15332.

[17] K. J. Vetter, J. W. Schultze, *J. Electroanal. Chem.*, **34** (1972) 131.

[18] B. E. Conway, B. Barnett, H. Angersteinkozlowska, B. V. Tilak, *J. Chem. Phys.*, **93** (1990) 8361.

[19] A. Kongkanand, J. M. Ziegelbauer, *J. Phys. Chem. C*, **116** (2012) 3684.

[20] K. J. Vetter, J. W. Schultze, *J. Electroanal. Chem.*, **34** (1972) 141.

[21] J. W. Schultze, K. J. Vetter, *Ber. Bunsenges. Phys. Chem.*, **75** (1971) 470.

[22] S. P. Devarajan, J. A. Hinojosa, J. F. Weaver, *Surf. Sci.*, **602** (2008) 3116.

[23] J. M. Hawkins, J. F. Weaver, A. Asthagiri, *Phys. Rev. B*, **79** (2009) 125434.

[24] J. O. Bockris, D. Drazic, A. R. Despic, *Electrochim. Acta*, **4** (1961) 325.

[25] J. O. Bockris, H. Kita, *J. Electrochem. Soc.*, **108** (1961) 676.

[26] N. M. Markovic, R. R. Adzic, B. D. Cahan, E. B. Yeager, *J. Electroanal. Chem.*, **377** (1994) 249.

[27] N. M. Markovic, H. A. Gasteiger, P. N. Ross, *J. Phys. Chem.*, **99** (1995) 3411.

[28] A. M. Gómez-Marín and J. M. Feliu, *ChemSusChem* **6** (2013) 1091

[29] S.K. Zecevic, J.S. Wainright, M.H. Litt, S.L. Gojkovic, R.F. Savinell, *J. Electrochem. Soc.*, **144** (1997) 2973 .

[30] H.A. Hansen, V. Viswanathan, J.K. Norskov, *J. Phys. Chem. C,* **118** (2014) 6706 .

[31] T. Zhang, A. B. Anderson, *Electrochim. Acta*, **53** (2007) 982.

Chapter 4

The role of non-covalent interactions in electrochemical reactions

In the previous section, we discussed electrochemical reactions involving only oxygenated species formed from H_2O or O_2, which is the component of the fuel cell reaction itself. In practical situation, however, there will be the cases where reactions take place with the presence of spectators such as anions in ionomer molecules. In the following two chapters, we focus on the role of spectator species in various electrochemical reactions.

The most practical spectator species in PEFCs are anions in ionomer molecules, which can be covalently bonded to Pt surface, and this "ionomer effect" will be discussed in the next chapter. In contrast, alkali (earth) cations have been regarded as non-influential species on Pt surface because they are stably hydrated and do not form covalent bonding with Pt in the potential window of 0 – 1.5 V (RHE) for aqueous electrolyte (Fig. 1.5.1). Recently, however, they were found to strongly affect some types of electrochemical reactions. This "cation effect" is firstly treated in this chapter, because it is not only new, but also provides foundations for understanding roles of spectator species in electrocatalytic processes.

4.1 Effects on fuel cell reactions

In the history of electrochemistry, the effects of spectator species on reaction kinetics have been discussed with the focus on covalently adsorbed species (directly-bonded with the electrode surface *via* orbital overlap) including underpotentially-deposited hydrogen (H_{upd}) atom [1, 2], anions [3, 4], oxygenated species [5] and CO molecule [6]. Such "chemisorbed" species are located in the inner Helmholtz plane (IHP), defined as the locus of the electrical centers of the chemisorbed ions (Fig. 1.5.1), and play decisive roles in electrocatalytic processes. The energy of adsorption of reactants and/or intermediates, as well as of spectator species, varies strongly from metal to metal, and thereby leads to significant variation in the electrochemical reaction rates.

Lying at the opposite end of surface-ion interactions traditionally considered are electrostatic forces, which act at distances of tens of angstroms and involve nonspecific adsorption of hydrated ions located in the outer Helmholtz plane (OHP), defined as the locus of the centers of these nonspecifically adsorbed ions (Fig. 1.5.1). According to classic double-layer theory [7, 8], the concentration of ions in the OHP is determined by the ratio of the electrostatic energy $zF\Phi_2$ (where z is the charge of the ions and Φ_2 represents the potential at the OHP) to the thermal energy (RT). The classic description of these interactions comes from Frumkin's pioneering papers [9, 10], in which the importance of Φ_2 in describing both the double-layer structure and electrode kinetics is discussed in terms of the difference between the applied potential, E, and the value of Φ_2 at the OHP; the potential E is closely related to the inner potential of the metal, Φ_M, and Φ_2 depends mainly on the overall concentration of the electrolyte.

Although the Frumkin correlation holds quite well on adsorbate-free electrodes, the commonly observed sensitivity of charge transfer to the chemical nature of the double layer remains largely elusive on adsorbate-modified electrodes. This elusiveness may stem from the fact that, besides strong covalent interactions and very weak electrostatic interactions, the importance of so-called 'non-covalent' interactions on the double-layer structure and kinetics has been neglected completely. (The term 'non-covalent interactions' is used here in concordance with the chemical literature for interactions with bond or stabilization energies smaller than 85 kJ mol^{-1} [11-13] and includes hydrogen bonding, cation–water bonding and cation–OH bonding.) The non-covalent interactions have not previously been considered in the studies of electrocatalysts for fuel-cell reactions and will be treated in this section with the example of cation effects on methanol oxidation in alkaline solutions [14].

4.1.1 Experimental

A Pt (111) surfaced single crystal disk ($0.283 cm^2$) was annealed using electromagnetic inductive heating for 5 minutes at approximately 1200 K in the flow of a mixture of H_2 and Ar (3% hydrogen). The annealed specimen was cooled slowly to room temperature in the flow of the same gas mixture and then, the Pt (111) surface was covered with a droplet of ultrapure water (Milli-Q, 18.2 MΩ) saturated with hydrogen. Afterward the electrode was embedded into an insertable RDE assembly and then immersed in 0.1 M LiOH, 0.1 M NaOH or 0.1 M KOH saturated with Ar in a Teflon cell at 0.05 V versus the reversible hydrogen electrode (RHE).

The electrochemical response was measured by scanning the potential at 50 mVs^{-1} to 1.15 V in the same solution (to record cyclic voltammograms (CVs)), and to 1.05 V in the Ar-saturated solution in the presence of 0.1 M methanol with the electrode rotation rate of 1600 rpm (to record polarization curves for the methanol oxidation reaction).

LiOH was from EMD, NaOH and KOH from JT Baker, and methanol from Baxter (high-purity grade). All gases were of 5N5 quality and purchased from Airgas Inc. The potentials are referred to RHE and IR-corrected.

4.1.2 Results

Figure 4.1.1a shows the CVs for Pt (111) surface in 0.1 M LiOH, 0.1 M NaOH and 0.1 M KOH. Four potential regions are clearly visible: adsorption of hydrogen ($H^+ + e^- \leftrightarrow H_{upd}$) between 0.05 and 0.4 V (region I), followed first by double-layer charging (region II), then by the reversible adsorption of OH_{ad} species ($OH^- \leftrightarrow OH_{ad} + e^-$) between 0.65 and 0.85 V (region III) and, finally, by irreversible adsorption of oxygen-containing species, historically termed 'oxide', above 0.85 V (region IV). Neither H_{upd} nor the double-layer features were affected by the nature of the alkali metal cation and therefore alkali metal cations are not specifically adsorbed onto Pt(111). In contrast, adsorption of OH_{ad} was enhanced in solutions that contained Li^+, but the formation of 'oxide' was highly suppressed in the presence of this cation. This finding suggests the existence of unexpected interactions between oxygen-containing species covalently bound to the Pt(111) surface in the IHP and nonspecifically adsorbing hydrated alkali metal cations located in the OHP. (Previously, an effect of alkali metal cations on voltammetry had been observed in sulfuric acid and in phosphate-buffered solutions, but the measured trends were qualitatively different from the results we obtained in nonspecifically adsorbing alkaline electrolytes as discussed in ref. [15, 16] and in Section 4.1.4 in this thesis.)

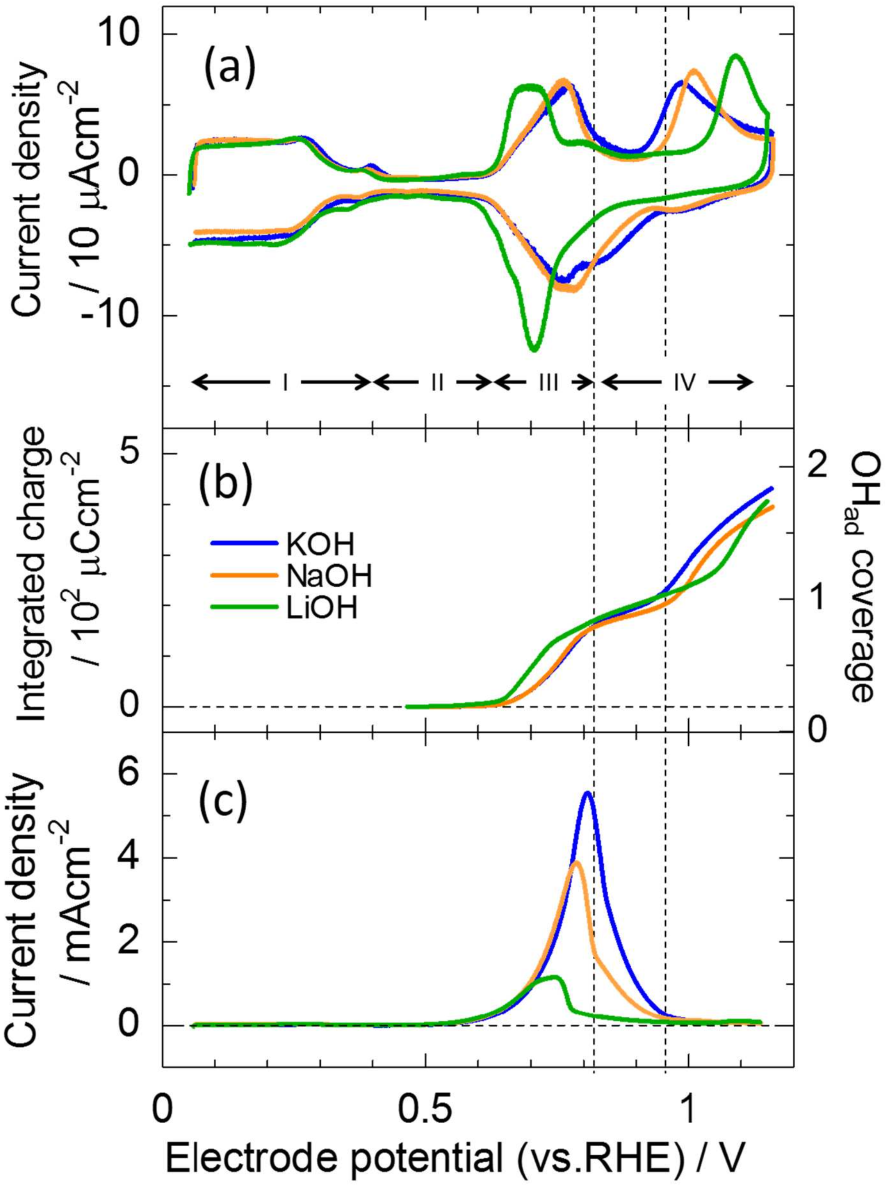

Fig.4.1.1 The effects of alkali metal cations on CVs and MOR currents in alkaline solution on Pt (111). (a) The effects on the shape of CV, including H_{upd} (region I), the double layer (region II), reversible adsorption of OH (region III) and irreversible oxide formation (region IV). (b) The effects on surface coverage of OH_{ad}. (c) The effects on polarization curves for MOR. The vertical dashed lines at 0.82 and 0.95 V emphasize that at a similar OH_{ad} coverage, the activities of MOR are controlled only by the nature of the cations.

The higher OH_{ad}-stabilization effect by smaller cation was confirmed using density functional theory (DFT) by Greeley [14]; the stabilization effect is larger in the presence of Li^+ than in the presence of Cs^+ by ca. 0.1 - 0.15 eV per one adsorbed OH. The stabilization can be thought of in terms of enhanced interaction energy between the hydrated OH adlayer and hydrated cation complexes, and is expected to result in a shift in the OH adsorption peak (Fig. 4.1.1a). The degree of the change in interaction energies from the DFT, less than ca. 80 kJ mol^{-1}, suggests that the interaction between covalently bound OH_{ad} groups and nonspecifically adsorbed cations can be classified as non-covalent one. Finally, the stabilization of OH is sufficiently large that further conversion of OH into atomic oxygen or bulk oxide-like species is rendered more endothermic, and thereby shifts the onset of the oxide formation to more positive potentials (see region IV in Fig. 4.1.1a).

Figure 4.1.1b shows the integrated charge for the OH_{ad} formation in the CVs (Fig 4.1.1a) and the corresponding surface coverage of OH_{ad} (Θ_{OH}) as a function of electrode potential. An apparent difference in Θ_{OH} is seen only between Li^+ and the other cations. However, this difference is observed only from 0.65 to 0.8 V, and again above 0.95 V, at which irreversible oxide formation takes place (region IV). In the potential region between 0.82 - 0.95 V (between vertical dashed lines), the curves of Θ_{OH} *versus* the electrode potential coincide and therefore the coverages of OH_{ad} are the same irrespective of the identity of the cation (ca. 0.6 - 0.8 ML). Also, if Θ_{OH} is the primary variable that determines the rates of oxygen reduction reaction (ORR) [17], hydrogen oxidation reaction (HOR) [1] and methanol oxidation reaction (MOR) [18], as has been suggested previously, those rates should be independent of the nature of the cation in this potential range.

Surprisingly, Fig. 4.1.1c shows that the activity of MOR between 0.8 - 0.95 V on Pt(111) is dramatically different and decreases in the sequence $K^+ > Na^+ >> Li^+$. (The same trends are also observed for ORR and HOR [14].) As these changes occur in the potential range where Θ_{OH} is independent of the nature of the alkali cation (between the vertical dashed lines), it seems likely that covalent interactions alone (as described by the Pt-OH_{ad} bond strength) are not sufficient to account for all of the reactivity trends. More essentially, the results of the cation effects give a clear evidence that the description only with a purely "inner-sphere" (covalent) bonding is not a perfect model of the electrochemical interface, and an "outer sphere" component, which has not been described previously, is likely to be important. This is not, however, to say that the covalently bound OH_{ad} is unimportant in determining the reactivity trends; indeed, MOR, (as well as ORR and HOR [14]), is only affected by the cation type in the potential region where Θ_{OH} is substantial (No cation effects are seen at the starting point of MOR (0.6 – 0.7 V) as shown in Fig 4.1.1c). Therefore, it appears that the measured activity changes result from direct interaction between hydrated cation, $M^+(H_2O)_x$, and OH_{ad}. This conclusion is also supported by results in sulfuric acid (Section 4.1.4), where OH_{ad} is not formed below 1 V (RHE) because of dominant adsorption of sulfate aninons and the cation effects on ORR curve are essentially eliminated. (Also, the more positive absolute potentials in acid imply that alkali ions will be found further from the electrode surface, reducing the interaction energy with OH_{ad} and further contributing to the lack of the cation effects.)

Fig. 4.1.2 shows the activity as Log(current) at constant potentials for ORR, HOR and MOR vs. the measured hydration energy of M^+ (drawn by Strmcnik) [14]. The each relationship is clearly linear and these correlations strongly suggest that a universal relationship exists between cation hydration energy and the reactivity of platinum surface in alkaline solution. In addition, such correlations are anticipated by the DFT analysis by Greeley [14] as mentioned above, given the analogies between the interactions for cation-water (hydration) and those for cation-OH_{ad}.

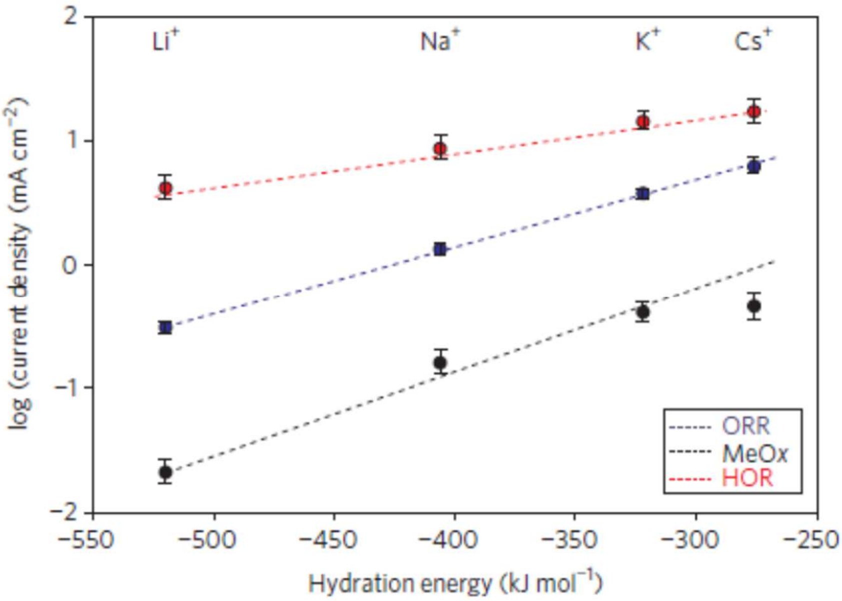

Fig.4.1.2 Logarithm of activity versus the hydration energy of alkali metal cation for ORR, HOR and MOR on Pt (111) in alkaline electrolyte (drawn by Strmcnik) [14]. As the measure of activity, diffusion –corrected currents at 0.9 and 0.95 V have been taken for ORR and HOR, respectively.

4.1.3 Discussion

As discussed above, hydrated cations are proposed to be stabilized in the compact part of the double layer through non-covalent bonding with adsorbed OH species. This stabilization leads to the formation of OH_{ad}-$M^+(H_2O)_x$ or $(H_2O)_{x-1}M^+\cdots H_2O\cdots OH_{ad}$ clusters (Fig. 4.1.3), which may be considered to be "quasi-specifically adsorbed" on platinum; the major difference between this quasi-specific adsorption of alkali metal cations and the well-known specific adsorption of anions [3, 4] is that, the contact is bridged by the adsorbed OH in the former case, while there is a direct metal-anion contact in the latter case. Note that the interaction between the adsorbed OH and the cation is substantially different from that suggested by Nagy et al. [19], and Wandlowski and De Levie [20] for a classic outer-sphere reaction, in which anions at the surface serve as a bridge that enhances electron transfer between adsorbed species and hydrated ions located at the OHP. In the new "non-covalent" model, the adsorbed OH species serve only as anchoring points for the hydrated cations, which enables the formation of clusters as spectators.

The concentration of OH_{ad}-$M^+(H_2O)_x$ clusters near the electrode surface should increase in the same order as the strength of interaction between OH_{ad} and $M^+(H_2O)_x$: $Li^+ > Na^+ > K^+ (> Cs^+)$. If the adsorbed clusters serve to inhibit the transfer of reactants to the electrode surface, the reaction rates are expected to decrease in the same sequence as the quasi-specific adsorption strength. Indeed, the activities for MOR (as well as ORR and HOR) in alkaline shows such a trend: $(Cs^+) > K^+ > Na^+ >> Li^+$.

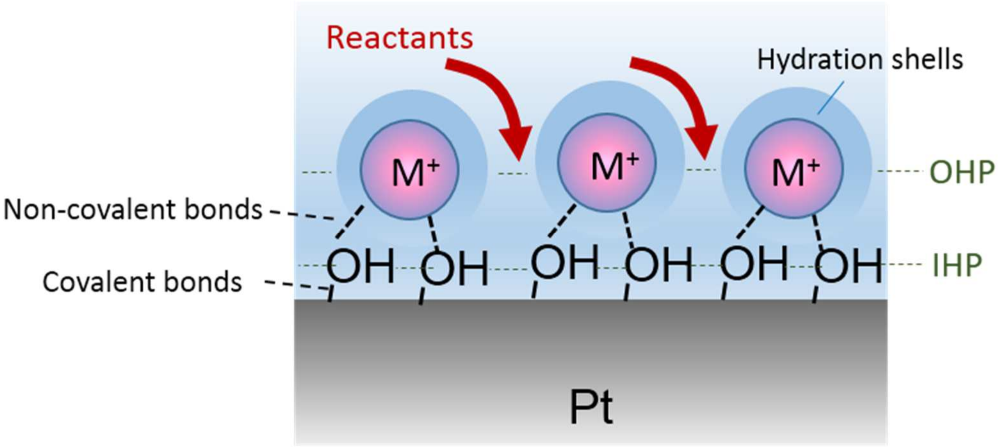

Fig.4.1.3 A model for non-covalent interactions between hydrated alkali metal cations and adsorbed OH.

4.1.4 Cation effect in acid

Figure 4.1.4 shows the CVs of Pt(111) in sulfuric acid solution with and without alkali metal cations (upper part) and corresponding polarization curves for the ORR (lower part). In agreement with previous results [15, 16], the CVs show that the peak at 0.65 V is shifted negatively in the presence of K^+, indicating that adsorption of sulfate/OH is affected by the hydrated cation. However, in contranst to alkaline solution, no effects of K^+ and Li^+ ions were observed on the ORR in the acidic media (Note that the applied Li^+ concentration of 10^{-2} M is definitely the level affecting the ORR activity in alkaline as presented in Section 4.2). The absence of a detectable effect in acids is likely due, in part, to the much lower surface coverage of OH_{ad} groups in sulfuric acid; this low coverage does not provide sufficient anchoring points for hydrated alkali cations, thus precluding the blocking effect, which were observed in alkaline in the above sections.

4.1.5 Conclusions

The importance of non-covalent interactions in electrochemical reactions was addressed by investigating the effects of the type of cation on MOR (as well as ORR and HOR) on Pt surface in alkaline solutions. The non-covalent interactions between OH_{ad} and $M^+(H_2O)_x$ were found to increase in the same order as the hydration energies of the included cations ($Li^+ >> Na^+ > K^+(> Cs^+)$) as indicated by an inverse trend for the reaction rate of MOR as well as ORR and HOR ($(Cs^+) > K^+ > Na^+ >> Li^+$), which can be well explained by higher concentration of OH_{ad}-$M^+(H_2O)_x$ clusters as spectators near the electrode surface for cation with larger hydration energy.

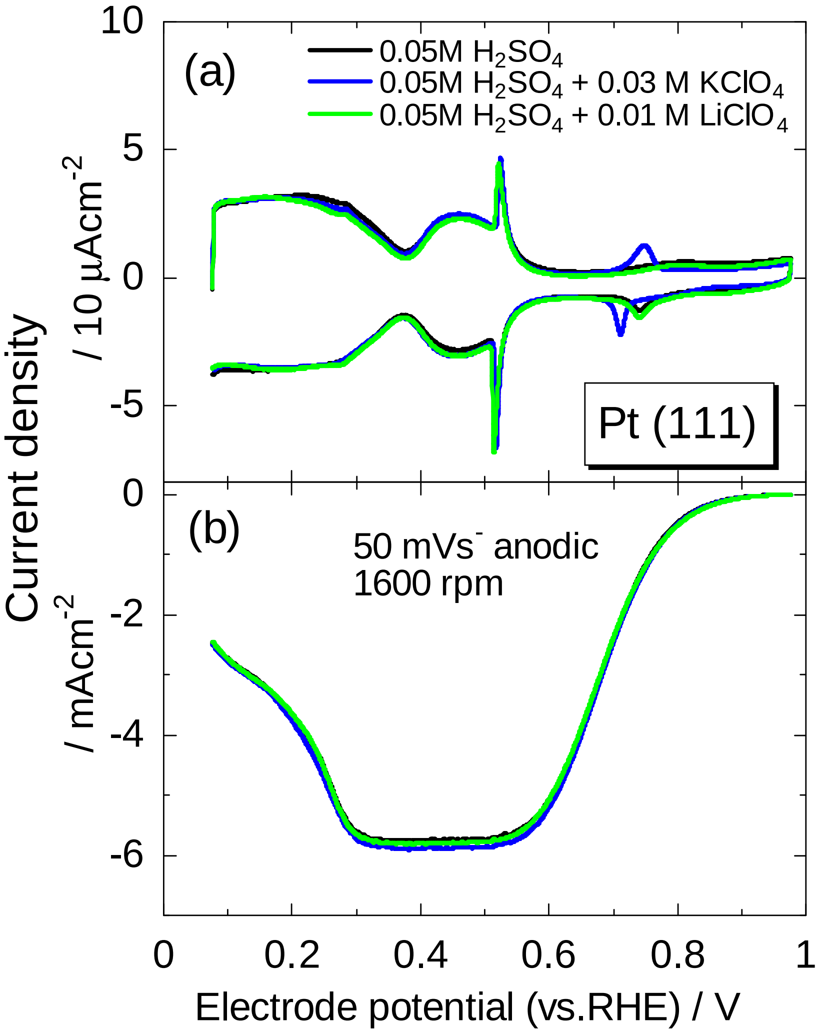

Fig.4.1.4 The effects of alkali metal cations on (a) CV and (b) ORR on Pt (111) in 0.05 M H_2SO_4.

4.2 Effects on bulk CO oxidation

In the previous section, the newly found cation effects on electrochemical reactions were presented. The new field in electrochemistry is now being developed as demonstrated by many works on the cation effects on various electrochemical reactions on Pt electrode. For example, by cations with large hydration enthalpies including Li^+, Ba^{2+} and Be^{2+}, oxygen reduction reaction (ORR) [14, 21-24], hydrogen oxidation reaction [14, 23], the oxidation of small organic molecules [25, 26], and the reduction of H_2O_2 [22] were suppressed while hydrogen evolution reaction [23, 27], CO oxidative stripping [28, 29] and the oxidation of H_2O_2 [22] were accelerated. The "non-covalent" model for explaining the cation effects has been supported using non-voltammetric methods; density functional theory calculations showed the higher stability of the OH_{ad}-hydrated cation cluster with larger hydration enthalpies of the cation [14]; X-ray scattering measurements suggested that Ba^{2+} cations are immobilized at 3.4 Å away from Pt (111) surface by OH_{ad} [21]; infrared spectroscopy measurements suggested the promotion of the OH_{ad} formation by Li^+ [30].

The non-covalent effects were also studied on Au electrode, and however, no cation effects were observed [21, 26]. This result as well as no cation effects in sulfuric acid presented in Section 4.1.4 was explained by lower coverage of OH_{ad} on the electrode. Thus OH_{ad} coverage seems to play an important role in the formation of the OH_{ad}-hydrated cation clusters.

In this section, the relationship between OH_{ad} coverage and the non-covalent interaction was further investigated by analyzing "bulk CO (CO_b) oxidation" (CO oxidation in electrolyte saturated with CO) in alkaline on Pt (111) and Pt (100) surfaced single crystal electrodes through voltammetric analyses. These experimental conditions are appropriate for the purpose because the OH_{ad} coverage can be drastically changed by adsorbing and lifting of CO molecules, and in the case of Pt (111), the potential region of the OH_{ad} formation can be definitely identified [31].

4.2.1 Experimental

Electrode preparation

A Pt (111) or (100) surfaced single crystal disk ($0.283 cm^2$) was annealed using electromagnetic inductive heating for 5 minutes at approximately 1200 K in the flow of a mixture of H_2 and Ar (3% hydrogen). The annealed specimen was cooled slowly to room temperature in the flow of the same gas mixture and then, the electrode surface was covered with a droplet of ultrapure water (Milli-Q, 18.2 MΩ) saturated with hydrogen. The electrode was then embedded into an insertable RDE assembly. Further details and the RDE assembling are described in Chapter 2 and a previous paper [32].

Afterward the electrode was transferred to alkaline electrolytes by two ways. In the first way, the electrode was transferred to alkaline electrolytes directly after being embedded into the RDE assembly. The electrode prepared using this procedure is noted as "as-prepared". In the second way, the embedded electrode was immersed in an acid electrolyte (0.1M $HClO_4$) saturated with argon at a potential of 0.06 V (RHE), was potential-cycled (lower limit: 0.06 V, upper limit: 0.96 V, $50 mV\cdot s^{-1}$, 20 cycles) with a rotation rate of 1600 rpm after the electrolyte was saturated with CO, and then was transferred to alkaline electrolytes, while the electrode was covered with a droplet of water saturated with hydrogen. The electrode prepared using this procedure is noted as “CO-annealed”.

CO reactivity measurements

The electrodes were immersed in 0.1M KOH, 0.1M KOH including 10^{-2} M LiOH, 0.1M KOH including 10^{-4} M $Ba(OH)_2$, or 0.1M KOH including 10^{-6} M $CuSO_4$ saturated with Ar at a potential of 0.06V and then the flow of Ar into the electrolyte was switched to that of CO. 25 minutes after the gas switching, the electrode potential was swept in the positive direction by $50mVs^{-1}$. The rotation of RDE was started at 1600 rpm 4s before the potential sweep. This procedure was found to make the results reproducible by our thorough investigation.

Chemicals etc.

LiOH was from Sigma-Aldrich (99.995% by metal basis), KOH from Alfa Aesar (99.99% by metal basis), $Ba(OH)_2$ from Sigma-Aldrich (99.996% by metal basis), and $HClO_4$ from JT baker (ULTREX II Ultrapure Reagent). Gasses were from Airgas (99.9999% for argon and hydrogen, 99.997% for CO). A glass cell was used for the acid electrolyte and a Teflon (FEP) cell for the alkaline electrolytes. A gold wire was used for the counter electrode. The potentials are referred to RHE and IR-corrected.

4.2.2 Results and discussion

In Figure 4.2.1a and 4.2.1b, the full red curves represent the CO_b oxidations on the Pt(111) and (100) pre-conditioned with the so-called CO annealing protocol [33-37] to remove defect sites of adislands.

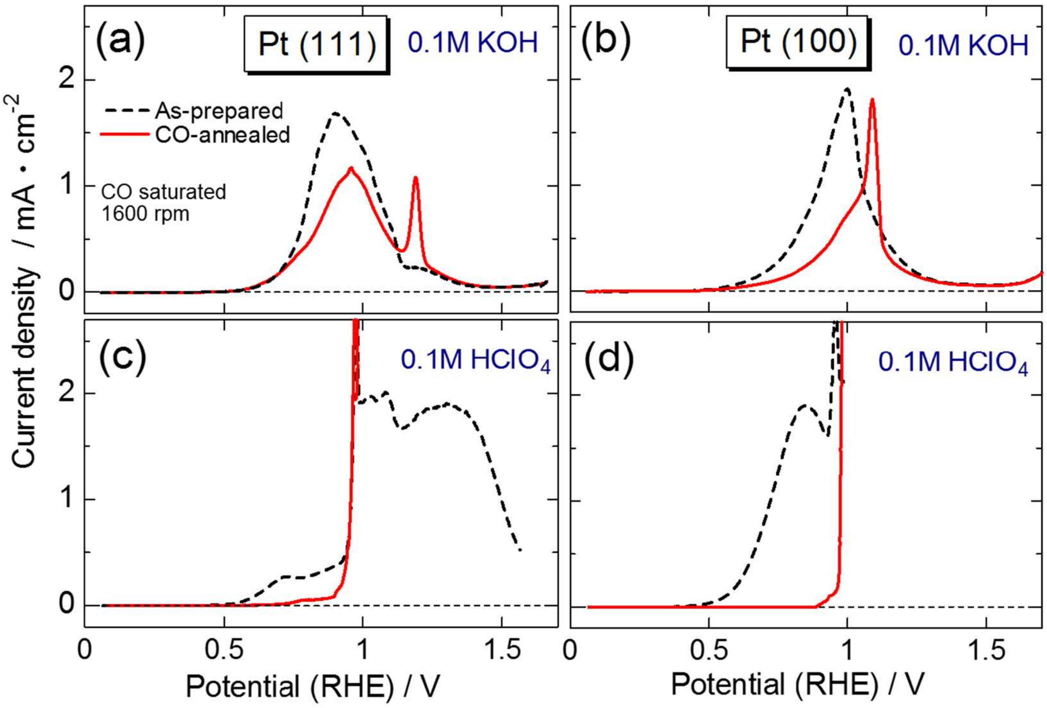

Fig.4.2.1 CO bulk oxidation voltammograms in the positive potential sweep on as-prepared and CO-annealed (a) Pt (111) and (b) Pt (100) surfaces in 0.1 M KOH. Those in 0.1 M $HClO_4$ are also shown for comparison on (c) Pt (111) and (d) Pt (100).

Several observations are noteworthy. (i) No CO oxidation is observed below 0.5 V in contrast to a previous study [38]. (ii) A broad oxidation peak is observed between 0.5 and 1.2 V. This peak is reminiscent of a pre-ignition peak in acid (Fig. 4.2.1c and 4.2.1d) regarding the potential region (starting at 0.5 V), which is observed only on the as-prepared surfaces and ascribed to CO oxidation on defect sites of adislands [33]. The CO oxidation starting at the low potential of 0.5 V even on the CO-annealed surfaces indicates additional types of active site which function only in alkaline (e.g. steps and ridges formed by the CO-annealing [33]). (iii) A sharp peak similar to CO-stripping peak centered at 1.1 - 1.2 V is observed. The stripping peak, which is indicative of the oxidations of large CO domains, is a testament of the fact that CO_b oxidations are taking place on almost completely CO-covered surfaces.

In the past, to improve CO oxidation, it was custom to introduce more oxophylic sites so that the adsorption of OH^- can compete with CO adsorption from the bulk of the electrolyte. Here, in order to promote the OH adsorption and thus CO oxidation, either the electrode or the solution side of the interface is tailored.

The dashed curves in Figure 4.2.1a and 4.2.4.b show the effect of an increased amount of Pt adislands on CO oxidation. Although the surfaces are still not active in the potential region below 0.5 V, the activities for CO oxidation on the “as prepared” surfaces are significantly higher than on the adisland-free CO-annealed surfaces. Note that, although the conditions for the first exposure to CO of the CO-annealed surfaces and of the as-prepared surfaces are different (i.e. acid for the CO-annealed surfaces and alkaline for the as-prepared ones as described in the experimental section) and the effect of solution pH at which the CO adlayer is formed on the activity for CO oxidation has been demonstrated [39], this is not the case for the present study because the as-prepared Pt (111) on which the CO adlayer had been formed in acid also showed the higher activity as shown in Fig. 4.2.2. Thus higher oxophylicity of Pt “defect” sites indeed plays an important role in the CO_b oxidation in alkaline [33, 38, 40-46] .

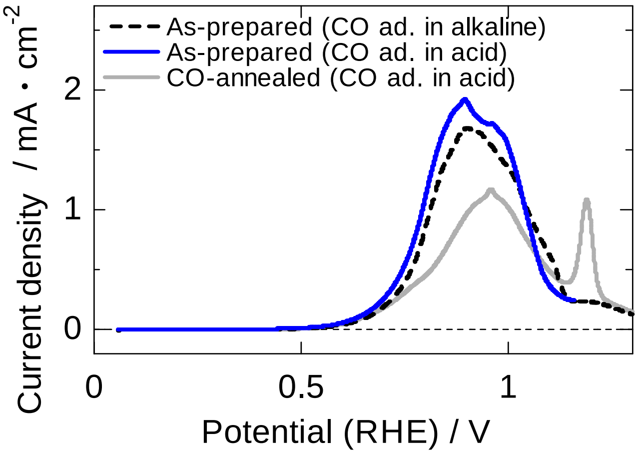

Fig.4.2.2 The effect of the condition for the first exposure to CO on the bulk CO oxidation in alkaline. Black dashed line: the activity on the as-prepared surface shown in Fig. 4.2.1a, on which the CO adlayer has been formed in the alkaline in the standard experimental protocol. Blue solid line: the activity on the as-prepared surface on which the CO adlayer has been formed in the acid before the activity measurement in the alkaline. Gray: the activity on the CO-annealed surface shown in Fig. 4.2.1a, on which the CO adlayer has been formed in the acid in the standard experimental protocol.

Along the same lines, an even more pronounced effect was observed on the surface, decorated by copper adislands that are formed via the underpotentially deposition (UPD) effects. As shown in Fig. 4.2.3, oxidation currents are observed as low as 0 V with the presence of a small amount of Cu^{2+} in the electrolyte. The currents are positive even in the negative-going scans (Fig. 4.2.3c and 4.2.3d) and moreover, as shown in Fig. 4.2.4, the oxidative charge below 0.5 V with the scan rate of 1 mVs^{-1} (0.05 C for the shaded area in Fig. 4.2.4) cannot be explained by dissolution of Cu even if the total amount of Cu^{2+} included in the cell was deposited on the Pt surface; 1 μM (Cu^{2+} concentration) × 0.07 L (amount of the electrolyte) × 96500 Cmol^{-1} (Faraday constant) × 2 (valence state of the Cu ion) = 0.0135 C. Therefore the observed prewaves should be due to CO$_b$ oxidations, implying that small coverage with Cu$_{upd}$ has significant catalytic effect by providing the necessary sites for OH$_{ad}$ as reactant. The resulting polarization curves are very similar to what has been reported for Pt(111)-CO system in alkaline before [38] and therefore a trace level of Cu^{2+} as an impurity was the most likely cause for the observed activity. The role of some other metal impurities on the CO oxidation and other electrochemical reactions was presented in ref. [47]. As noted above, however, in a Cu^{2+}-free solution, no activity is observed below 0.5 V.

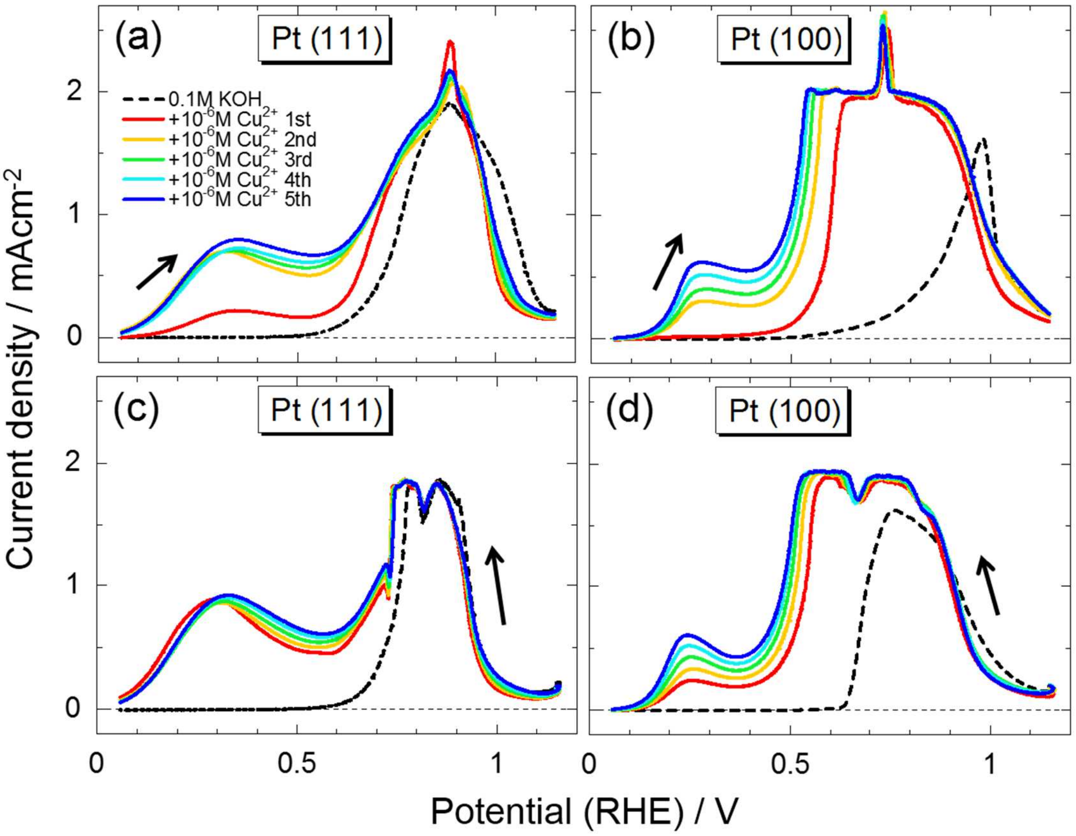

Fig.4.2.3 Changes in CO bulk oxidation voltammograms on the Pt surfaces during potential cycles to 1.15 V with the presence of 10^{-6} M Cu^{2+} for (a) Pt (111) and (b) Pt (100) in the positive potential sweep, and (c) Pt (111) and (d) Pt (100) in the negative potential sweep.

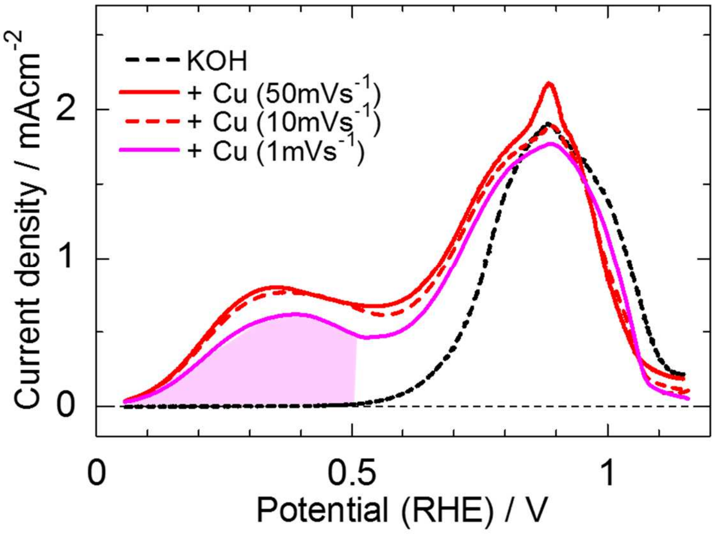

Fig.4.2.4 The effect of potential-scan rate on CO bulk oxidation in the positive scan on Pt (111) surface with the presence of 10^{-6} M Cu^{2+}. The voltammogram without Cu^{2+} is also shown for comparison (black dashed line). The oxidation charge below 0.5 V for 1 mVs^{-1} is calculated as 0.05 C, which corresponds to the shaded area.

In the both cases, the introduction of more oxophylic centers, which are covered by OH or oxides or a mix of both, to the Pt surfaces promotes the oxidation of CO. In the following, we explore if the adsorption of OH_{ad} can be promoted by modifying the solution side of the interface with non-covalently bound cations.

Figure 4.2.5 summarizes the cyclic voltammogram (CV) of Pt (111) (upper part) and the polarization curve for the CO_b oxidation (lower part) in 0.1 M KOH in the same potential region. The

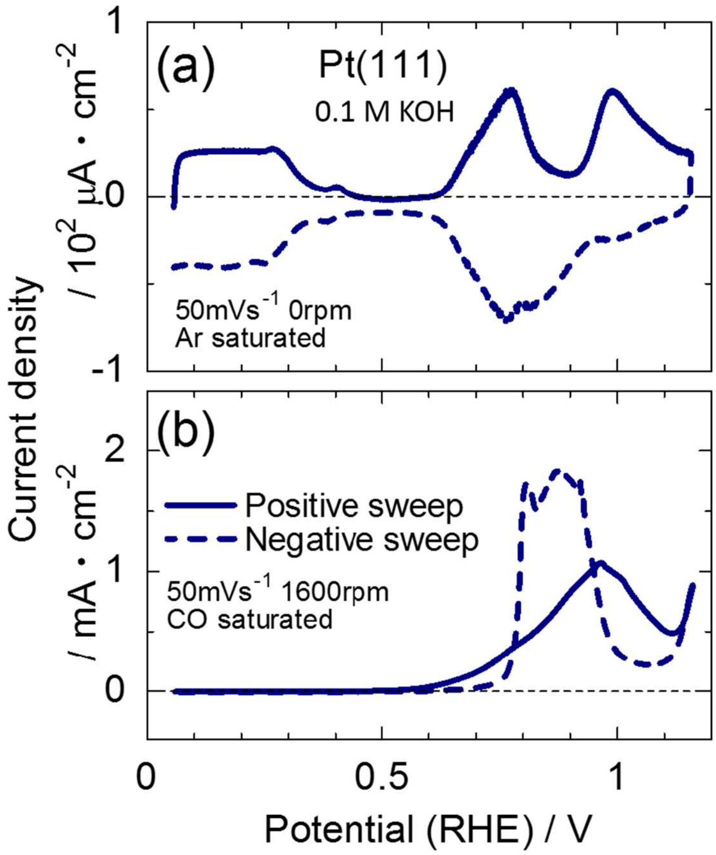

Fig.4.2.5 (a) Cyclic voltammogram of Pt (111) in inert condition in 0.1M KOH. (b) The difference in CO bulk oxidation voltammogram on the CO-annealed Pt (111) between the positive and negative potential sweeps, when the potential is turned at 1.2 V. The solid curves are the currents in the positive sweep and the dashed curves are the ones in the negative sweep.

CV shows a characteristic hydrogen adsorption potential region between 0.05 - 0.45 V which at more positive potentials is followed first with a double layer, then with reversible adsorption of OH_{ad} (0.6 - 0.9 V), and finally with an irreversible formation of a ‘true” Pt oxide. A typical CO oxidation polarization curve recorded on the positive sweep direction shows that CO oxidation starts at 0.5 V reaching the maximum activity at 0.95 V and then the activity is monotonically decreasing due to oxide formation. On the reverse sweep direction, diffusion-limited CO oxidation current [33] appears as a plateau between 0.95 - 0.80 V and the observed differences are typical for the process where in the positive sweep the electrode is covered with CO and on the reverse sweep the electrode is pre-covered by oxygenated species that are required for the reaction to proceed. The potential region of the plateau corresponds to the one where the reduction of Pt oxide starts but OH_{ad} coverage still remains high as shown in the CV (Fig. 4.2.5a). Therefore, CO_b oxidation is promoted when both oxide-free Pt atoms are accessible to CO in the electrolyte and adsorbed OH_{ad} is abundant to react with CO via Langmuir-Hinshelwood mechanism [48].

Figure 4.2.6 shows the effects of the additions of Li^+ and Ba^{2+} on CV and CO_b oxidation. In CV (Fig. 4.2.6a), the adsorption of OH is promoted (the peak at 0.65-0.85 V is shifted to lower potential) and both the formation and reduction of oxide (the anodic peak in the potential above 0.9 V and the cathodic peak appearing at the shoulder of the peak for OH desorption) are suppressed by these additives, while the behavior of underpotentially deposited hydrogen (0.05 - 0.4 V) is not affected. The effects are larger for Ba^{2+} with the concentration of 10^{-4} M than for Li^+ with the 100 times higher concentration, 10^{-2} M. For CO_b oxidation, the effects of those additives are not at all observed in the positive sweep (Fig. 4.2.6b). In the negative sweep, however, a substantial change in the activity occurs by the addition of Ba^{2+}; the potential region of the diffusion limiting plateau is negatively shifted (Fig. 4.2.6c). A small but clearly discernable negative shift of the polarization curve is observed for the addition of Li^+ .

To explain these effects, we rely on recent advances in electrocatalysis, which pertain to the influence of non-covalently bound cations on the behavior of the electrochemical interfaces. Specifically, it has been shown that the presence of Li^+ and Ba^{2+} cations has a pronounced effect on the reactivity of metal surfaces in alkaline solutions. For example, in the presence of 10^{-4} M Ba^{2+} a huge deactivation of ORR was observed; e.g., a negative shift of 150 mV for the half-wave potential as shown in Fig. 4.2.7 [21]. It has been shown that Ba^{2+} solvated cations can modify the surface in a variety of ways, ranging from direct enhancement of OH adlayer formation to the formation of non-specifically adsorbed patterns of Ba^{2+}-water complex that selectively block access of solution phase species to the surface and to affecting the interfacial properties of water molecules [21, 23] . It has also been shown that the oxidation of CO monolayer in solution free of CO can be catalyzed by the addition of cations with high energy of hydration, such as Li^+ and Be^{2+}, due to their promoting effect on the formation of OH adlayer [28]. In contrast to CO stripping experiment, CO_b oxidation is independent of the nature of cations in the positive sweep direction (Fig. 4.2.6b). The effect of cations is only observed on the negative sweep, where Li^+ and Ba^{2+} have promoting effects (Fig. 4.2.6c). The reason

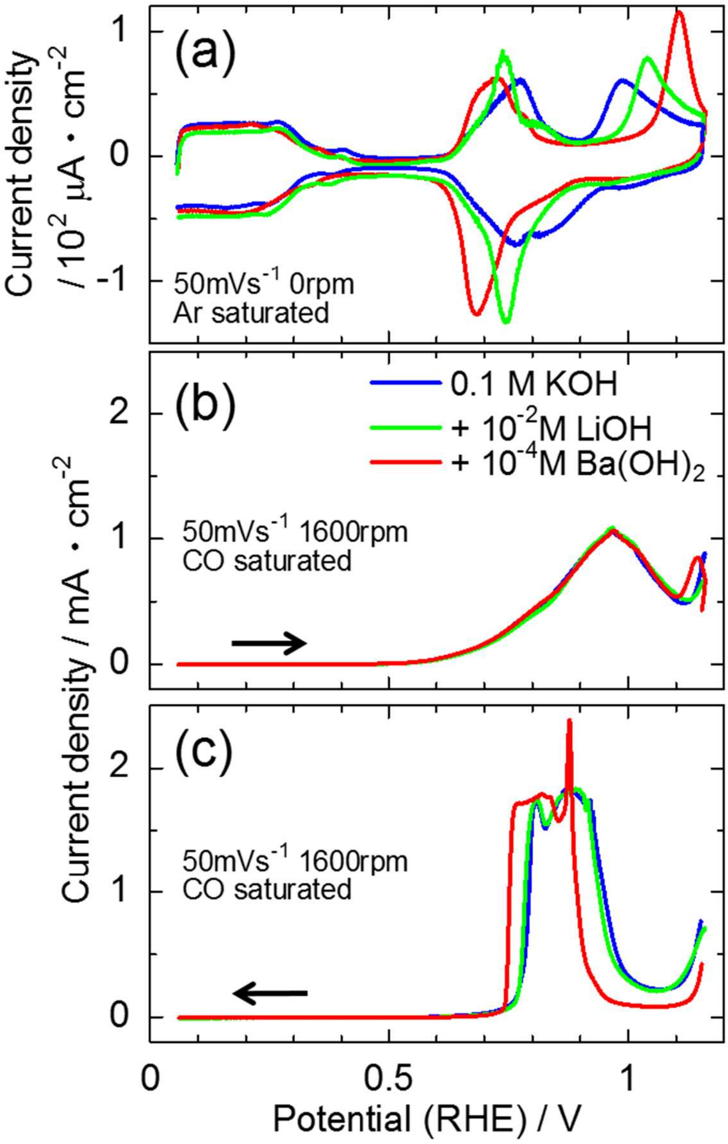

Fig.4.2.6 The effects of the additions of Li^+ and Ba^{2+} on (a) CV in inert condition, (b) CO bulk oxidation voltammogram in the positive potential sweep and (c) that in the negative potential sweep.

for this is believed to lie in the critical coverage by OH_{ad}. Because the non-covalent van der Waals forces are relatively weak, the coverage by OH_{ad} has to be substantial in order to attract the hydrated cations. This explanation has been supported by the results on Au (hkl) surfaces in alkaline [21, 26] and Pt (111) surface in sulfuric acid (Section 4.1.4), where the effects of cation on the reaction rates below 1 V (RHE) are negligible because of the low coverage with OH_{ad}. The same is true for the CO_b oxidation on Pt (hkl) where the surface is fully covered by CO, as in the present case (Fig.4.2.8a). In the negative sweep direction, however, the situation is quite different as the surface is now covered by oxygenated species and interacts strongly with the hydrated cations in the double layer (Fig. 4.2.8b). In fact, Ba^{2+} and Li^+ interactions stabilize the OH adlayer as demonstrated in the CVs in Fig 4.2.6a. Hence, the activity order for CO_b oxidation in the negative sweep is K^+<Li^+<Ba^{2+} (Fig. 4.2.6c).

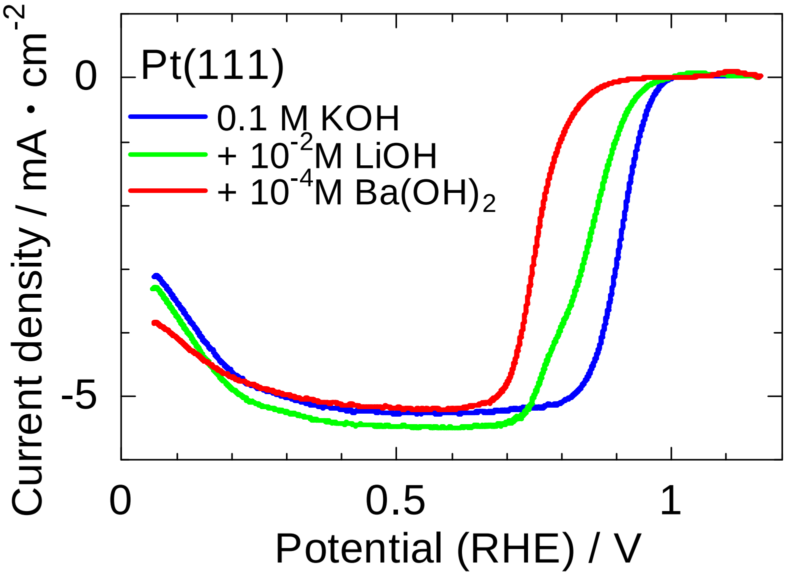

Fig.4.2.7 The effects of the additions of Li^+ and Ba^{2+} on ORR curve for Pt (111) surface in the positive potential sweep.

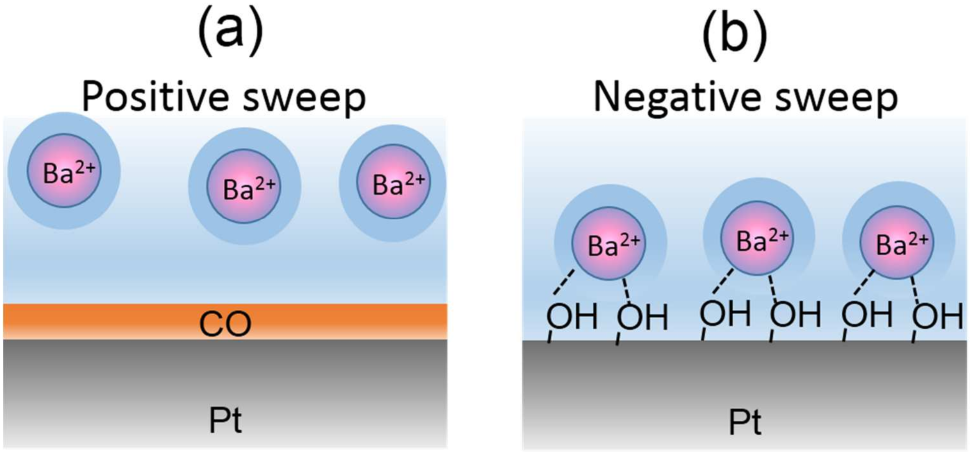

Fig.4.2.8 Models for the interface between the Pt electrode and alkaline solution with the additive of Ba^{2+} in the CO bulk oxidation voltammetry (a) in the positive potential sweep (with high coverage of CO_{ad}) and (b) in the negative potential sweep (with low coverage of CO_{ad}).

4.2.3 Conclusions

The role of non-covalent interactions on CO_b oxidation on Pt surface in alkaline solution was investigated. Similar to acidic environment, the presence of adsorbed OH_{ad} on the surface is instrumental for a good catalyst. While we find that the reaction is much more facile in the pre-ignition region compared to acid, there is still no oxidation observed below 0.5 V. Trace levels of Cu^{2+} were found to dramatically improve the rate of the reaction through an oxidized form of copper on the Pt surface; the oxidation potential is shifted roughly 0.5 V more negative, to 0 V vs. RHE, by providing the necessary sites for the adsorption of OH as reactant. Furthermore, the non-covalent effect of the added cations is not observed when the surface is highly covered with CO_{ad}, because of lowered OH_{ad} coverage by CO_{ad}. Once the CO_{ad} layer is stripped by oxidation, electrode surface is available for adsorption of OH_{ad}, and interaction with cations from the solution; CO_b oxidation is promoted in the presence of Li^+ and Ba^{2+}, and the non-covalent interaction effect is demonstrated.

Finally, a strong correlation between the OH_{ad} coverage and the double layer structure was demonstrated. By changing one, we inherently affect the other. This observation offers a great tool for designing of future catalysts as it allows us to change the activity for specific reactions by orders of magnitude by careful tailoring of the electrochemical double layer structure.

4.3 References

[1] B.E. Conway, B.V. Tilak, *Electrochim. Acta*, **47** (2002) 3571 .

[2] D. Strmcnik, D. Tripkovic, D. van der Vliet, V. Stamenkovic, N.M. Markovic, *Electrochem. Commun.*, **10** (2008) 1602 .

[3] O.M. Magnussen, *Chem. Rev.*, **102** (2002) 679 .

[4] D.V. Tripkovic, D. Strmcnik, D. van der Vliet, V. Stamenkovic, N.M. Markovic, *Faraday Discuss.*, **140** (2008) 25 .

[5] N.M. Markovic, P.N. Ross, *Surf. Sci. Rep.*, **45** (2002) 121 .

[6] C. Korzeniewski, C.L. Childers, *J. Phys. Chem. B*, **102** (1998) 489 .

[7] P. Delaahay, *Double Layer and Electrode Kinetics*, Wiley, (1963) .

[8] W.R. Fawcett, *Frontiers in*, Electrochemistry (1998) 323 .

[9] A.N. Frumkin, *Z. Physik. Chem.*, **A164** (1933) 121 .

[10] A.N. Frumkin, B. Slygin, *Acta Physiochem.*, URSS (1936) 819 .

[11] K. Muller-Dethlefs, P. Hobza, *Chem. Rev.*, **100** (2000) 143 .

[12] D.J. Miller, J.M. Lisy, *J. Am. Chem. Soc.*, **130** (2008) 15381 .

[13] D.J. Miller, J.M. Lisy, *J. Am. Chem. Soc.*, **130** (2008) 15393 .

[14] D. Strmcnik, K. Kodama, D. van der Vliet, J. Greeley, V.R. Stamenkovic, N.M. Markovic, *Nat. Chem.*, **1** (2009) 466 .

[15] J.M. Feliu, M.J. Valls, A. Aldaz, M.A. Climent, J. Clavilier, *J. Electroanal. Chem.*, **345** (1993) 475 .

[16] N. Garcia, V. Climent, J.M. Orts, J.M. Feliu, A. Aldaz, *ChemPhysChem*, **5** (2004) 1221 .

[17] N.M. Markovic, R.R. Adzic, B.D. Cahan, E.B. Yeager, *J. Electroanal. Chem.*, **377** (1994) 249 .

[18] N. Markovic, P.N. Ross, *J. Electroanal. Chem.*, **330** (1992) 499 .

[19] N.C. Hung, Z. Nagy, *J. Electrochem. Soc.*, **134** (1987) 2215 .

[20] T. Wandlowski, R. Delevie, *J. Electroanal. Chem.*, **380** (1995) 201 .

[21] D. Strmcnik, D.F. van der Vliet, K.C. Chang, V. Komanicky, K. Kodama, H. You, V.R. Stamenkovic, N.M. Markovic, *J. Phys. Chem. Lett.*, **2** (2011) 2733 .

[22] I. Katsounaros, K.J.J. Mayrhofer, *Chem. Commun.*, **48** (2012) 6660 .

[23] N. Danilovic, R. Subbaraman, D. Strmcnik, A.P. Paulikas, D. Myers, V.R. Stamenkovic, N.M. Markovic, *Electrocatal.*, **3** (2012) 221 .

[24] J. Suntivich, E.E. Perry, H.A. Gasteiger, Y. Shao-Horn, *Electrocatal.*, **4** (2013) 49 .

[25] E. Sitta, B.C. Batista, H. Varela, *Chem. Commun.*, **47** (2011) 3775 .

[26] C.A. Angelucci, H. Varela, G. Tremiliosi, J.F. Gomes, *Electrochem. Commun.*, **33** (2013) 10 .

[27] R. Subbaraman, D. Tripkovic, D. Strmcnik, K.C. Chang, M. Uchimura, A.P. Paulikas, V. Stamenkovic, N.M. Markovic, *Science*, **334** (2011) 1256 .

[28] C. Stoffelsma, P. Rodriguez, G. Garcia, N. Garcia-Araez, D. Strmcnik, N.M. Markovic, M.T.M. Koper, *J. Am. Chem. Soc.*, **132** (2010) 16127 .

[29] D.F. van der Vliet, M.T.M. Koper, *Surf. Sci.*, **604** (2010) 1912 .

[30] M. Nakamura, Y. Nakajima, N. Hoshi, H. Tajiri, O. Sakata, *ChemPhysChem*, **14** (2013) 2426 .

[31] M. Wakisaka, H. Suzuki, S. Mitsui, H. Uchida, M. Watanabe, *Langmuir*, **25** (2009) 1897 .

[32] N.M. Markovic, H.A. Gasteiger, P.N. Ross, *J. Phys. Chem.*, **99** (1995) 3411 .

[33] D.S. Strmcnik, D.V. Tripkovic, D. van der Vliet, K.C. Chang, V. Komanicky, H. You, G. Karapetrov, J. Greeley, V.R. Stamenkovic, N.M. Markovic, *J. Am. Chem. Soc.*, **130** (2008) 15332 .

[34] S.W. Lee, S. Chen, W. Sheng, N. Yabuuchi, Y. Kim, T. Mitani, E. Vescovo, Y. Shao-Horn, *J. Am. Chem. Soc.*, **131** (2009) 15669 .

[35] K.J.J. Mayrhofer, M. Hanzlik, M. Arenz, *Electrochim. Acta*, **54** (2009) 5018 .

[36] E.G. Ciapina, E.A. Ticianelli, *Electrochim. Acta*, **58** (2011) 172 .

[37] E. Toyoda, R. Jinnouchi, T. Ohsuna, T. Hatanaka, T. Aizawa, S. Otani, Y. Kido, Y. Morimoto, *Angew. Chem.-Int. Edit.*, **52** (2013) 4137 .

[38] N.M. Markovic, T.J. Schmidt, B.N. Grgur, H.A. Gasteiger, R.J. Behm, P.N. Ross, *J. Phys. Chem. B*, **103** (1999) 8568 .

[39] M.S. Farias, C. Busó-Rogero, R. Gisbert, E. Herrero, J.M. Feliu, *J. Phys. Chem. C*, **118** (2014) 1925 .

[40] S.C. Chang, J.D. Roth, M.J. Weaver, *Surf. Sci.*, **244** (1991) 113 .

[41] N.P. Lebedeva, M.T.M. Koper, J.M. Feliu, R.A. van Santen, *Electrochem. Commun.*, **2** (2000) 487 .

[42] W. Akemann, K.A. Friedrich, U. Stimming, *J. Chem. Phys.*, **113** (2000) 6864 .

[43] J.S. Spendelow, J.D. Goodpaster, P.J.A. Kenis, A. Wieckowski, *J. Phys. Chem. B*, **110** (2006) 9545 .

[44] J.S. Spendelow, Q. Xu, J.D. Goodpaster, P.J.A. Kenis, A. Wieckowski, *J. Electrochem. Soc.*, **154** (2007) F238 .

[45] E. Herrero, Q.S. Chen, J. Hernandez, S.G. Sun, J.M. Feliu, *Phys. Chem. Chem. Phys.*, **13** (2011) 16762 .

[46] J. Inukai, D.A. Tryk, T. Abe, M. Wakisaka, H. Uchida, M. Watanabe, *J. Am. Chem. Soc.*, **135** (2013) 1476 .

[47] R. Subbaraman, N. Danilovic, P.P. Lopes, D. Tripkovic, D. Strmcnik, V.R. Stamenkovic, N.M. Markovic, *J. Phys. Chem. C*, **116** (2012) 22231 .

[48] S. Gilman, *J. Phys. Chem.*, **68** (1964) 70 .

Chapter 5

Pt/ionomer interface

The interface between Pt surface and ionomer, a practical system in fuel cell reactions, is treated in this chapter. Pt single crystal electrodes are powerful model electrodes in this case as well, because anion adsorption can be detected by cyclic voltammetry, as exemplified by the case for the adsorption of sulfate anion on Pt (111) (Fig. 5.1) [1].

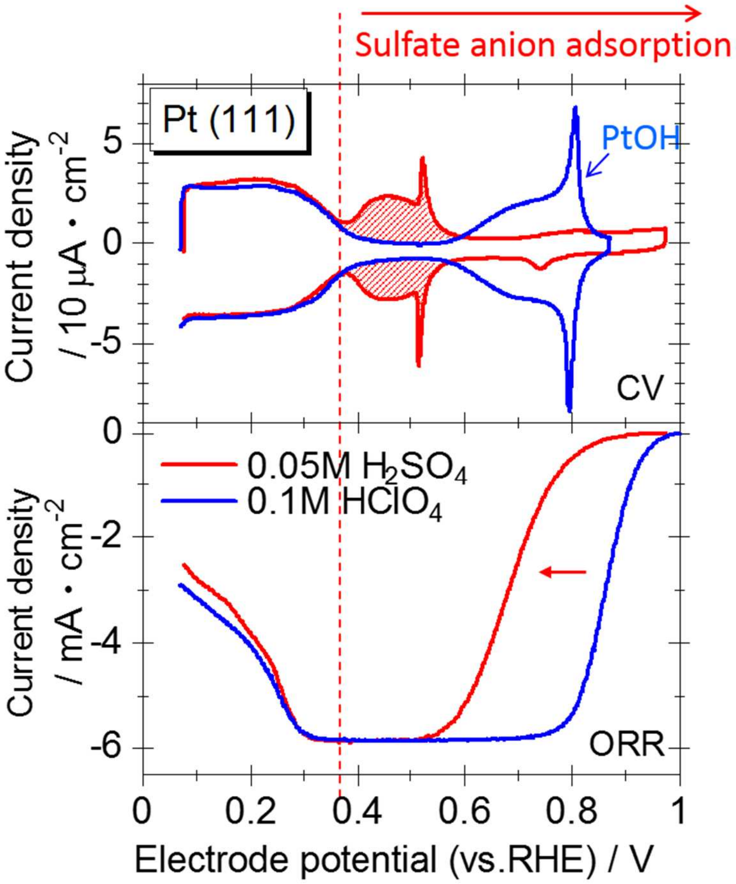

Fig. 5.1 The effect of sulfate anion adsorption on the CV and ORR curve on Pt (111) surface. The shaded butterfly peaks correspond to the oxidative adsorption and reductive desorption of sulfate. ORR activity is significantly suppressed by the anion adsorption.

5.1 Oxygen reduction reaction at Pt/ionomer interface

In catalyst layers of polymer electrolyte fuel cells, a solid polymer electrolyte, called “ionomer” for distinguishing it from the electrolyte membrane, is generally used to form good electrochemical interfaces on catalyst surfaces (Fig. 1.1.1). However, model experiments using Pt single crystal electrodes covered with ionomer films suggested that sulfonate anion in perfluorinated sulfonic acid polymer (*e.g.* Nafion, Fig. 1.3.2), which is almost exclusively used as the ionomer, blocks active sites on Pt catalyst and therefore slows down the kinetics of ORR (“catalyst-poisoning effect”) [2].

The results obtained by an elegant experimental approach with Pt single crystals developed by Subbaraman et al. [2] were impressive because the adsorption and desorption of the sulfonate anions of Nafion on Pt (111) surface were clearly observed electrochemically. The uniformity of the film, however, was not confirmed by any direct observations and thus it was not conclusive whether the electrode surface was completely covered with the film or not. (If the coverage is not perfect, the behavior of bare-Pt (111) is superposed and thus quantitative information cannot be obtained.) This issue is addressed and the effect of Nafion coating on ORR is quantitatively analyzed in this section. The uniformity of the film on the electrode is checked using scanning electron microscope (SEM) equipped with energy-dispersive X-ray spectroscopy (EDS) and the method developed by Subbaraman et al. [2] is used in electrochemical measurements.

5.1.1 Experimental

Electrode preparation

A Pt (111) surfaced single crystal disk (99.99%, 0.196 cm^2, MaTecK) was annealed using electromagnetic inductive heating for 10 minutes at 1400 - 1650 K in the flow of a mixture of H_2 and Ar (3 % H_2, Taiyo Nippon Sanso, the purity of each gas: H_2: 99.99999%, Ar: 99.999%) [3]. The annealed specimen was slowly cooled down to room temperature in the flow of the same mixed gas and then, the Pt (111) surface was covered with a droplet of ultrapure water (Milli-Q, 18.2 MΩ).

Ionomer coating

The prepared specimen was immersed in 1 mM KBr to form one monolayer (ML) of Br on the surface for minimizing contaminations during the following ionomer-coating procedure [4], and then was rinsed with ultrapure water. While the Pt (111) surface was wet, 20 μL of 0.005 wt % ionomer solution (20 wt% dimethylformamide (DMF) aqueous solution [2, 5], to which 5 wt % Nafion solution (ALDRICH, equivalent weight: 1100 $g\cdot mol^{-1}$) was added) was dropped on the surface. The specimen was then dried at *ca.* 378 K to evaporate water and DMF, followed by a heat-treatment at *ca.* 420 K for 3 minutes to improve the physico-mechanical stability of the film.

Electrochemical cleaning

The ionomer-coated Pt (111) surface was dipped into 0.1 M $HClO_4$ (MERCK, Suprapur) saturated with Ar (Taiyo Nippon Sanso, 99.999%) in the configuration of hanging meniscus rotating disk electrode (HM-RDE) [6] and subjected to potential cycling between 0.0 and 0.98 V at a scan rate of 50 $mV\cdot s^{-1}$ for more than 30 cycles at an electrode rotation rate of 1850 rpm to accelerate the removal of contaminations from the electrode surface by hydrogen evolution [4]. All potentials refer to RHE and are IR-corrected.

Electrochemical measurements

Cyclic voltammograms were obtained in the same electrolyte saturated with Ar at a scan rate of $50mV\cdot s^{-1}$. Then the electrode was transferred to 0.1 M $HClO_4$ saturated with O_2 (Taiyo Nippon Sanso, 99.999%) in the HM-RDE configuration, and LSVs (ORR polarization curves) were taken at a scan rate of $50mV\cdot s^{-1}$ with an electrode rotation of 1850 rpm. The temperature was 303 K.

SEM observation

The electrode surface was observed with SEM-EDS after the electrochemical measurements. The acceleration voltage for the electron beam was 15 kV.

5.1.2 Results and Discussion

Uniformity of Nafion film

Figure 5.1.1a shows an SEM image of the whole region of the Nafion-coated Pt (111) surface after the electrochemical measurements. The surface appears bright at the periphery and is light grey in the inner area. The two regions have a clear boundary, as shown in the magnified image (Fig.5.1.1b). The EDS analysis (Fig. 5.1.1c) shows that fluorine, which is included in Nafion, is in the light grey region but not in the bright periphery. Hence, the light grey region and bright periphery correspond to Nafion film and bare Pt surface, respectively and this analysis shows that the whole Pt (111) surface except for the thin periphery was kept covered with Nafion throughout the electrochemical measurements. This well-defined Nafion/Pt(111) interface enables quantitative discussion of the effect of the Nafion coating. The key points for casting a uniform and clean film are discussed in Appendix B.

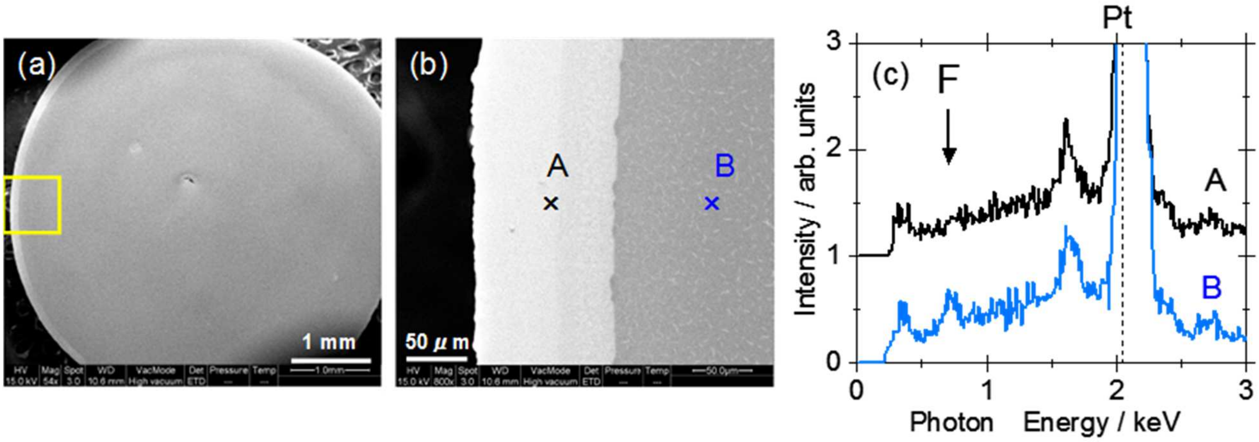

Fig.5.1.1 SEM-EDS analysis of the Nafion film on the electrode surface. (a) SEM image of the entire region. (b) Magnified SEM image for the square region in (a). The marks are the places where EDS was measured. (c) EDS measured in the bright region (A) and in the grey region (B), where the electron beam was focused on an area of $50\times50\mu\mathrm{m}^2$. The peak position for fluorine is denoted by the down-pointing arrow.

The thickness of the ionomer film is calculated to be 35 nm from the volume of the ionomer solution dropped on the surface assuming the density of dried Nafion, 1.5 g·cm^{-3}, which is much thinner than the diffusion layer thickness in the liquid electrolyte at the rotation rate of 1850 rpm, approximately 15 μm from the RDE theory. Therefore, the ORR kinetic current can be precisely estimated by assuming the first reaction order using the mass-transport correction described as

$$i_{\mathrm{k}}^{\gamma=1}(E) = \frac{i(E)i_{\mathrm{d}}}{i_{\mathrm{d}} - i(E)}, \qquad (3.2.5)$$

where $i_{\mathrm{K}}(E)$ is the kinetic current, i_{d} is the diffusion limiting current, $i(E)$ is the measured current and E is the electrode potential (see Section 3.2).

CV

Figure 5.1.2 shows the CVs for Pt (111) surfaces with and without the Nafion coating. The flat reversible peak between 0.07 – 0.4 V due to underpotentially deposited hydrogen (H_{upd}) is not changed by the Nafion coating, indicating that Nafion molecules do not interact with Pt (111) surface in this potential region and in addition, the Pt (111) surface is kept clean and morphologically well-defined even after the Nafion coating.

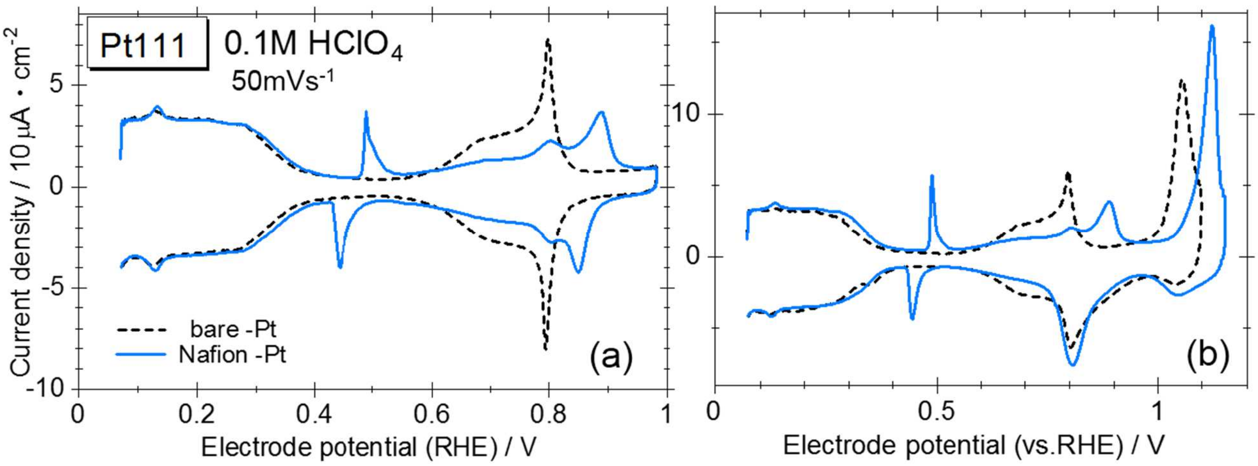

Fig. 5.1.2 CVs for Pt (111) surfaces with and without the Nafion coating. Upper limit of the potential scan: (a) 0.98 V, (b) 1.15 V. Blue solid line: with Nafion coating, black dashed line: without Nafion coating (bare-Pt).

As a distinct behavior for Nafion-coated Pt (111), irreversible sharp peaks are observed in the double layer region (0.4 – 0.6 V). They have been attributed to the oxidative adsorption and reductive desorption of sulfonate anions [2, 4, 5, 7, 8]. The charge for the anodic peak is 16 $\mu\mathrm{Ccm}^{-2}$, corresponding to the coverage of *ca*. 0.07 ML if the adsorption is a one-electron-transfer process: $-SO_3^- + Pt \rightarrow -SO_3 - Pt + e^-$. The hydroxyl adsorption (the butterfly peak between 0.6 V and 0.85 V) and oxide formation (the peak above 1.0 V) are suppressed on the Nafion-coated electrode. This implicates that poisoning by Nafion molecules occurs up to at least 1.0 V, and therefore is expected to affect the ORR kinetics.

ORR curve

Figure 5.1.3 shows the ORR curves in the anodic scan for Pt (111) surfaces with and without the Nafion coating. The diffusion-limiting plateaus are clearly seen in the potential range of 0.3 – 0.7 V for the both electrodes and diffusion-limiting currents, *ca*. 7 $\mathrm{mA{\cdot}cm^{-2}}$, are close to the theoretical value of 6.6 $\mathrm{mA{\cdot}cm^{-2}}$ [9]. These data show that the RDE experiments were properly carried out.

The current is lower for the Nafion-coated Pt than for the bare-Pt in the potential region above 0.7 V, indicating that the ORR kinetics is slowed down by the Nafion coating. From Eq. 3.2.5, the kinetic current is decreased by 73 % at 0.82 V and by 54 % at 0.90 V.

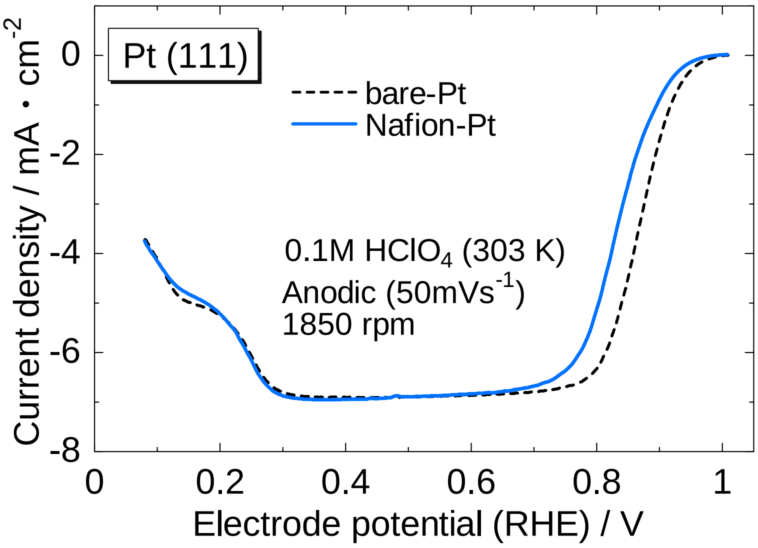

Fig. 5.1.3 ORR curves in the anodic scan for Pt (111) surfaces with and without the Nafion coating. Blue solid line: with Nafion coating, black dashed line: without Nafion coating.

These reduction ratios are much more significant than those estimated from an assumption that the kinetic current is proportional to (1 - θ_S), where θ_S is the ratio of the electrode surface area poisoned by the sulfonate anions to the total electrode surface area, and is estimated to be *ca.* 0.2 even at a maximum by assuming that each sulfonate anion masks three Pt atoms via three oxygen atoms of the functional group and that the coverage of sulfonate is 0.07 ML as suggested from the CV (Fig. 5.1.2). This discrepancy can be elucidated if other species are adsorbed on the electrode surface without peaks in the CV. Plausible candidates are OH(ads), H_2O molecules and the fluorinated part of the polymer chain. In-situ infrared (IR) spectroscopy will be useful for detecting them if any.

5.1.3 Conclusions

A uniformly-Nafion-coated Pt (111) electrode enabled quantitative analysis of the effect of the Nafion coating on the ORR kinetics. Sulfonate anions in the Nafion molecules are adsorbed on the electrode surface above 0.5 V (RHE) with a coverage of 0.07 ML. The ORR kinetic current is decreased by 73 % at 0.82 V and by 54 % at 0.90 V by the Nafion coating.

5.2 Ionomer effect under dry conditions

In the previous section, a well-defined interface between Pt (111) and Nafion film was prepared and the quantitative discussion was enabled. In addition, the success in the preparation of the well-defined and clean Pt/Nafion interface on the Pt single crystal, which is essential for precise analysis for electrode kinetics, even after the exposure of the Pt surface to organic chemicals for the casting of the Nafion film, opens up a new field of analytical methods using Pt single crystals. Since the experiments in the previous section were carried out by contacting the ionomer-coated electrode surface to an aqueous electrolyte, the ionomer is fully hydrated. The conditions are largely different from those in the catalyst layer in real fuel cells. For getting insights into real PEFCs, it is also important to examine the electrochemistry of dried Nafion-coated electrodes.

For this purpose, a solid-state cell, in which an electrode is not dipped into an aqueous electrolyte but pressed onto a solid electrolyte membrane [10-13], is applied for analyzing an electrochemical interface in dry states. In this section, on the basis of the Nafion-coating technique described in the previous section, a solid-state cell with a Nafion-covered Pt (111) single crystal is devised and electrochemical measurement is carried out to clarify the effect of hydration state of the ionomer on the anion adsorption behavior [7]. The application of a solid-state cell to Pt single crystal electrodes has not yet been reported in the history of electrochemistry.

5.2.1 Experimental

Configuration of Solid-cell

The configuration of the newly developed solid-state cell is shown in Fig. 5.2.1. A Nafion-coated Pt (111) surfaced single crystal (99.99 %, MaTecK) with an electrode surface area of 0.196 cm^2 for the working electrode (WE) was pressed against a cast Nafion membrane having a thickness of 1 mm. The Nafion membrane had been cleansed thoroughly beforehand by boiling it in 10 % H_2O_2 twice, then in 0.5 M H_2SO_4 once, and finally in water (Milli-Q) three times. The whole cell was placed in a gas-exchangeable container. A platinized Pt mesh in a hydrogen-reserved glass tube immersed in 0.1 M $HClO_4$ connected to the Nafion membrane was used for the reference electrode (RE). The counter electrode (CE) was a Pt plate.

Electrode preparation and mounting

A Nafion-coated Pt (111) surface electrode was prepared through the procedure described in the previous section. The prepared surface was dipped into deaerated 0.1 M $HClO_4$ and the cyclic voltammogram (CV) was obtained to examine the cleanness of the surface. Then the electrode was rinsed with Milli-Q water, and then transferred to the solid-state cell. After the electrode was mounted on the Nafion membrane, the solid-state cell was enclosed in the container. Then, Ar gas bubbled through water was flowed into the container. Afterward, the CV was obtained under the wet condition. The temperature and scan rate were 295 K and 50 mVs^{-1}, respectively, in all experiments in the present study. Gas flow rates were not controlled in all experiments, but the effect of drying of ionomer can be qualitatively discussed as described in the following sections.

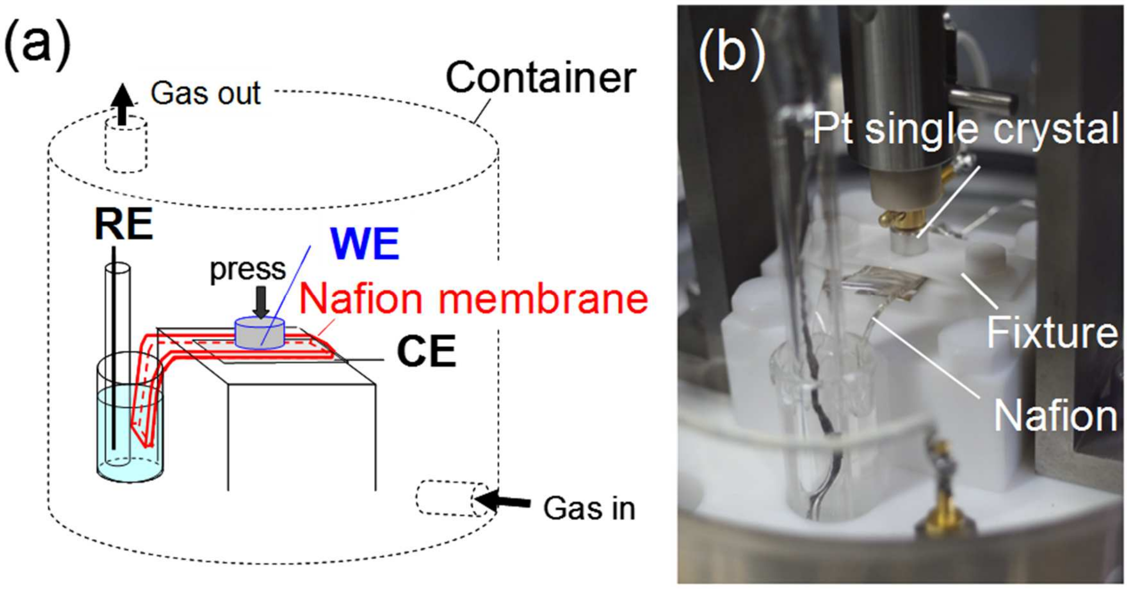

Fig. 5.2.1 The configuration of the solid-state cell. (a) The illustration of the whole setup. (b) The magnified photograph of the cell. The fixture has a hole for the mounting of the Pt single crystal.

5.2.2 Results and Discussion

CV

Figure 5.2.2 shows the CVs for the Nafion-coated Pt (111) surfaces in the aqueous electrolyte (0.1M $HClO_4$) and in the solid-state cell under the wet condition. The potential was referred to RHE for each measurement, the potential of which was measured by filling the each container with hydrogen.

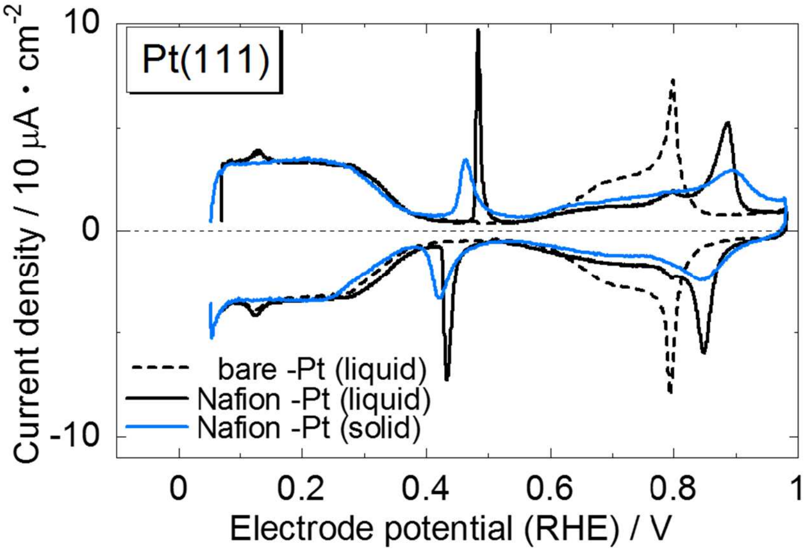

Fig. 5.2.2 The CVs for the Nafion-coated Pt (111) surfaces in the aqueous (liquid) electrolyte of 0.1 M $HClO_4$ (black solid line) and in the solid-state cell (blue solid line). The CV for a bare Pt (111) is also shown for comparison (black dashed line).

The result in the previous studies was reproduced in the aqueous electrolyte. That is, by the Nafion coating, irreversible sharp peaks due to the adsorption and desorption of the sulfonate anions emerged in the double layer region (0.4 – 0.5 V) and the hydroxyl adsorption (0.6 - 0.85 V) was suppressed, while the flat reversible peaks (0.07 – 0.4 V) due to underpotentially deposited hydrogen (H_{upd}) were not changed [2, 4, 5]. In the solid-state cell, the voltammogram is quite similar to that in the aqueous solution, and therefore the peaks can be assigned to H_{upd} (0.07 -0.4 V) and anion-adsorption/desorption (0.4 – 0.5 V). This data is the first observation of the CV of Pt (111) in a solid-state cell in the history of electrochemistry.

Anion adsorption property under dry condition

After the measurement under the wet condition, the wet-gas flow was switched to a dry-gas flow. Figure 5.2.3a shows the CVs after the switching. In this graph, the potential was referred to the terminal potential of the RE, not RHE potential. Two small peaks are observed at *ca*. 0.08 V and *ca*. 0.15 V in hydrogen desorption region in some voltammograms. These can be ascribed to the oxidation of hydrogen molecules generated in the cathodic scan and hydrogen desorption from defect site of (110) step formed during potential cycles [14], respectively. In the following, we do not go further into these peaks but focus only on the anion-related behaviors above 0.3 V.

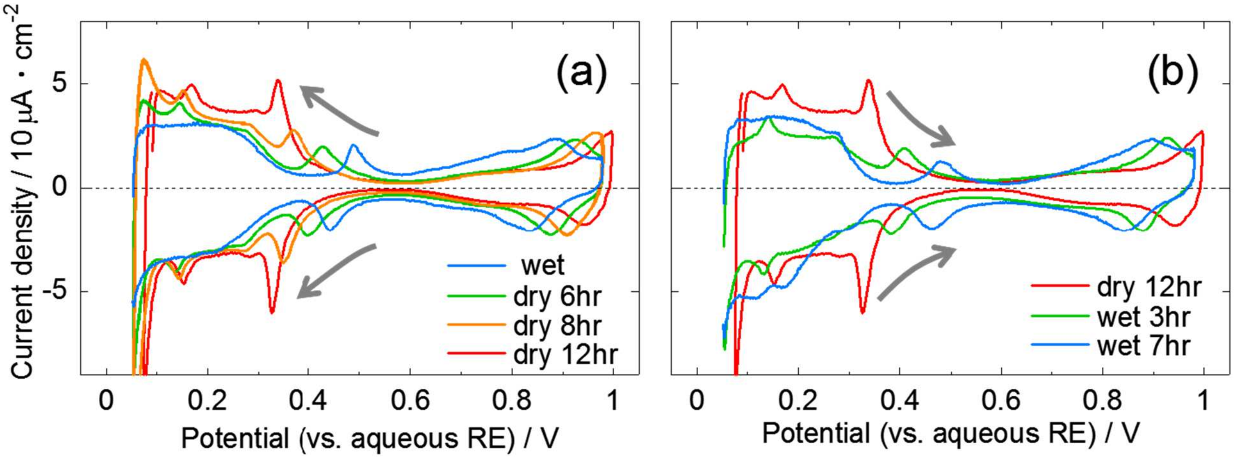

Fig. 5.2.3 Changes in the CV for the Nafion/Pt(111) interface in the solid-state cell after (a) the switching to the dry-gas flow and (b) the re-switching to the wet-gas flow. The potential is referred to the terminal potential of the RE.

The anion-adsorption/desorption peaks are shifted to lower potentials during the dry-gas flow as indicated by the arrows. This peak shift is reversible as shown in Fig. 5.2.3b, which shows that the peaks are shifted back to higher potentials after re-switching to the wet-gas flow. In these gas-switching and re-switching periods, the Nafion membrane, and surely the ionomer as well, experienced dehydration and then hydration as indicated by the ionic resistance of the membrane measured between the WE and CE using impedance spectroscopy (Fig. 5.2.4) [15]. The anion adsorption potential is in

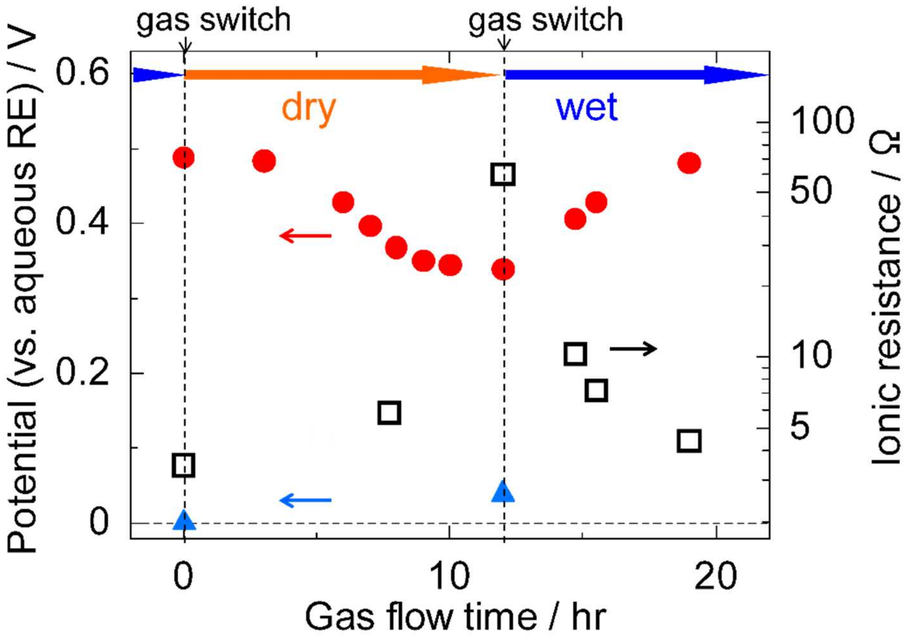

Fig. 5.2.4 The peak potential for the anion adsorption (red circle), terminal potential of the WE under hydrogen atmosphere against the RE (blue triangle), and ionic resistance of the Nafion membrane between the WE and CE (open square), plotted against the gas flowing time after the switching to the dry-gas flow. The dry-gas flow was re-switched to the wet-gas flow at 12 hr.

good correlation with the hydration/dehydration process as shown in Fig. 5.2.4 and therefore, can be judged to be lowered when the ionomer becomes dehydrated.

In Fig. 5.2.4, the terminal potential of the WE under hydrogen atmosphere against the RE, $\Delta E_{\mathrm{hydrogen}}$, is also plotted against the gas flowing time. $\Delta E_{\mathrm{hydrogen}}$ is almost zero (within ±1 mV) under the fully-wet condition, and is not zero (*ca.* +40 mV) under the driest condition. This result can be explained as follows. Under the wet condition, protons in the aqueous phase of 0.1 M $HClO_4$ and in the solid phase of Nafion are in equilibrium (*Donnan* equilibrium), and therefore potential difference, $\Delta\Phi$, is formed to cancel the potential difference between the RE and WE due to the difference in the activity of proton between the two phases (Fig. 5.2.5a). In contrast, under the dry condition, water can steadily flow from the aqueous RE to the dried membrane, and therefore, protons in the two phases are not in equilibrium. The positive $\Delta E_{\mathrm{hydrogen}}$ indicates the increase in the reversible hydrogen potential for the WE with drying (Fig. 5.2.5b), which is most likely due to the increase in the chemical potential of proton in the ionomer by water evaporation.

Since the RE potential is fixed (reversible hydrogen potential in 0.1 M $HClO_4$), the decrease in the anion adsorption potential shown in Fig. 5.2.4 is ascribed to the decrease in the absolute potential for the anion adsorption, not the increase in the RE potential, and indicates the intrinsic increase in the anion adsorptivity, which is also visible in the hydroxyl adsorption/desorption region (above 0.6 V in Fig. 5.2.3); the dryer the condition is, the more suppressed the hydroxyl adsorption is. Suppression of Pt-oxide formation with drying of ionomer has also been reported for Pt nanoparticles in PEFCs

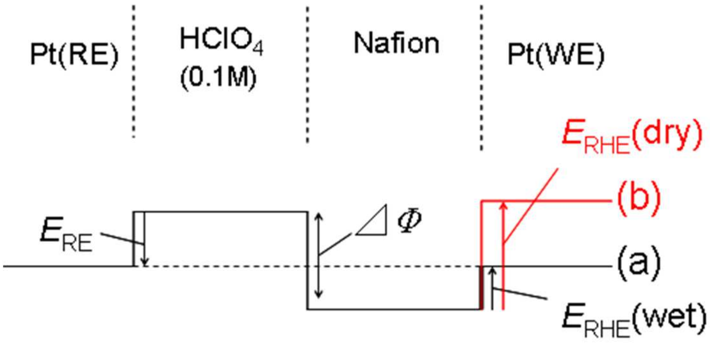

Fig. 5.2.5 Potential profiles in the cell when the WE is under hydrogen atmosphere in (a) fully-wet and (b) dry conditions. E_{RE}: electrode potential for the RE, $\varDelta\Phi$: potential difference between the aqueous phase and solid phase formed by *Donnan* equilibrium, E_{RHE}: electrode potential for the WE under hydrogen atmosphere. Terminal potential is the potential in Pt phase.

operations and ascribed to the increase in the adsorptivity of sulfonate anions by Watanabe and co-workers [16-18].

This higher adsorptivity of the dehydrated ionomer can be explained by higher chemical potential of the hydrated (desorbed) sulfonate anion, which is probably caused by two reasons: decrease in the hydration stabilization energy of ionomer and increase in the anion concentration in water channels in ionomer. Detailed mechanisms could be obtained from further quantitative experimental data such as a plot of the anion adsorption potential *vs*. the hydration number (the number of water molecules per one sulfonic acid) of the ionomer, λ, and their comparison with theoretical calculation. Those data should be obtained under steadily controlled relative humidity. For that purpose, a modification of the solid-state cell is underway to use a solid RE.

5.2.3 Conclusions

A novel experimental scheme using a solid-state cell with a Pt single crystal electrode was established. The cyclic voltammogram showed that a well-defined and clean Nafion/Pt (111) interface was successfully formed in the solid-state cell; peaks due to the adsorption and desorption of the sulfonate anions were clearly observed. The data is the first observation of the CV of Pt (111) in a solid-state cell in the history of electrochemistry. With dehydration of the ionomer, the anion-adsorption/desorption peaks are shifted to lower potentials and the hydroxyl adsorption is more suppressed. The results show that the anion adsorptivity is increased with drying in PEFCs.

5.3 Catalyst poisoning property of sulfonimide acid ionomer

In the previous sections, the catalyst poisoning with sulfonate anion in Nafion has been demonstrated. For improving the ORR performance, therefore, ionomers with functional groups that are less adsorptive to Pt surface are expected to be developed. In this section, the catalyst poisoning property of a sulfonimide acid polymer, which is also a promising electrolyte for PEFCs, is discussed [19].

Gibbs free energies for the adsorptions of various anions on Pt (111) surface, ΔG, at 0.8 V *vs.* standard hydrogen electrode (SHE) have been already obtained by a first principles theory combined with a continuum electrolyte theory by Jinnouchi (Fig. 5.3.1) [19]. The result shows that the adsorption is weaker for sulfonimide anion than for sulfonate anion.

Recently, Shinohara et al. developed a novel ionomer having two sulfonimide acid groups in its side chain ended with a perfluorobutane, instead of a sulfonic acid, NBC4 (Fig. 5.3.2), which has higher protonic conductivity and O_2 permeability than Nafion [20]. Since the acid group in the newly-introduced side chain is less-adsorptive as shown by the theoretical calculation (Fig. 5.3.1) and ended with the inactive fluorinated part, NBC4 is expected to be less-poisoning and to have improved properties not only for the proton conduction and O_2 transport but also for ORR kinetics. These expectations are experimentally examined in this section.

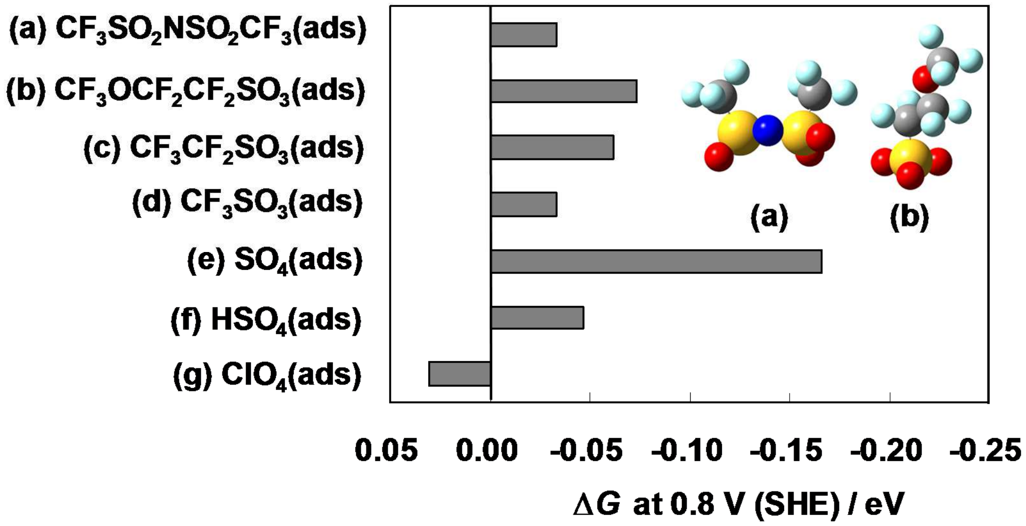

Fig 5.3.1 The theoretically calculated free energies of the adsorption reactions, ΔG, on Pt (111) surface for (a) perfluoro-sulfonimide anion and (b,c) perfluoro-sulfonate anions at 0.8 V (SHE) [19]. Those for (d) trifluoromethanesulfonate anion, (e,f) sulfuric acid anion (for the adsorbate of (e) sulfate and that of (f) bisulfate), and (g) perchlorate anion are also shown for comparison.

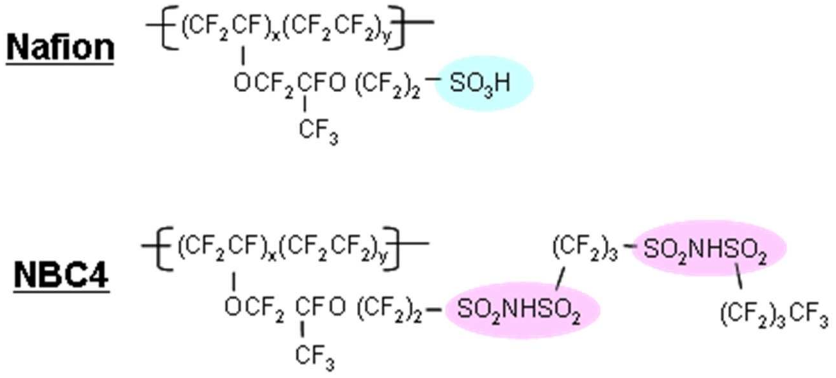

Fig. 5.3.2 Molecular structures of Nafion and NBC4. y/x: 6.6 for Nafion and 6.8 for NBC4.

5.3.1 Experimental

The preparations of the ionomer-coated Pt (111) surfaces and electrochemical measurements were carried out through the procedures described in Section 5.1. The amounts of Nafion and NBC4 deposited on the Pt (111) surface are equal on a weight basis.

5.3.2 Results and Discussion

Uniformity of ionomer film

The Nafion film has already been concluded to be uniform from the contrast in SEM image of the whole region of the Pt (111) surface (Section 5.1.2). The NBC4-coated Pt (111) surface shows a similar contrast as shown in Fig. 5.3.3; the surface appears bright at the periphery corresponding to bare-Pt and light grey in the inner area corresponding to the ionomer film. Therefore, a uniform film was obtained also for NBC4.

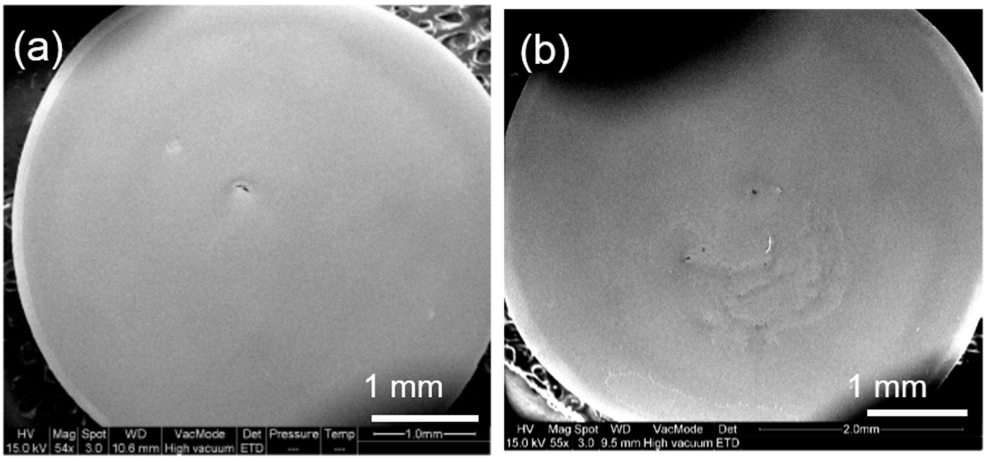

Fig. 5.3.3 SEM images of the whole regions of the (a) Nafion-coated and (b)NBC4-coated Pt (111) surfaces after the electrochemical measurements.

CV

Cyclic voltammograms for Pt (111) surfaces covered with the ionomers and for the bare surface are shown in Fig. 5.3.4. The Nafion-coated Pt showed irreversible sharp peaks in the double layer region (0.4 – 0.6 V), which have been attributed to the oxidative adsorption and reductive desorption of sulfonate anion [2, 4, 5, 7].

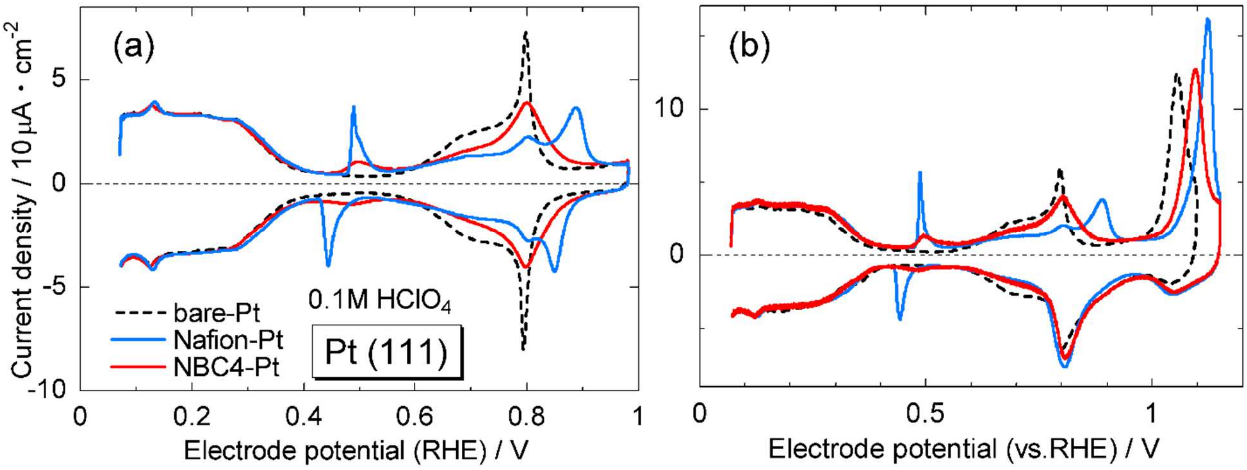

Fig. 5.3.4 The CVs for Pt (111) surfaces covered with the ionomers and the bare surface. Upper limit: (a) 0.98 V, (b) 1.15 V. Black dashed line: without ionomer coating (bare-Pt), blue solid line: with Nafion coating, red solid line: with NBC4 coating.

Although the NBC4-coated Pt also has seemingly-anion-related peaks in the same potential range, they are much duller. Another difference in the nature of the anion adsorption is visible in the hydroxyl adsorption/desorption (0.6 - 0.9 V) and oxide formation (above 1.0 V) regions. While both the ionomer-coatings suppress the hydroxyl adsorption and oxide formation, the degree of suppression is much less for the NBC4-coating than for the Nafion-coating. These results show that the poisoning by the anions of NBC4 is weaker than that of Nafion and are consistent with the theoretical results (Fig. 5.3.1). The steric effect due to the perfluorobutane-terminal in NBC4, which is not included in the theoretical calculation, may also play a role for the weaker anion adsorption.

ORR

Figure 5.3.5 shows the ORR polarization curves for Pt (111) surfaces covered with the ionomers and for the bare surface. The diffusion-limiting plateaus are clearly seen in the potential range of 0.3 – 0.7 V for all the electrodes and the diffusion-limiting currents are close to the theoretical value of 6.6 mA·cm^{-2}. These data show that the RDE experiments were properly carried out.

Figure 5.3.6 shows the Tafel plots for the ORR kinetic currents obtained using Eq. 3.2.5. The Tafel slope is 65 mV·decade^{-1} for the bare Pt, which is close to a reported value above 0.82 V, 60 mV·decade^{-1} [21]. The NBC4-coated surface exhibits a higher ORR kinetic current than the Nafion-coated surface (by *ca*. 50 % at 0.82V) and thus, has a better property for the ORR kinetics than the

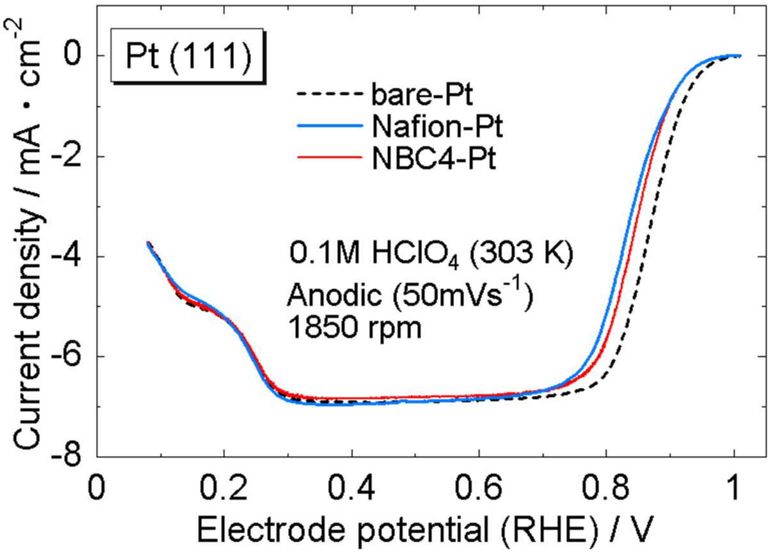

Fig. 5.3.5 The ORR polarization curves for Pt (111) surfaces covered with the ionomers and for the bare surface. Black dashed line: without ionomer coating (bare-Pt), blue solid line: with Nafion coating, red solid line: with NBC4 coating.

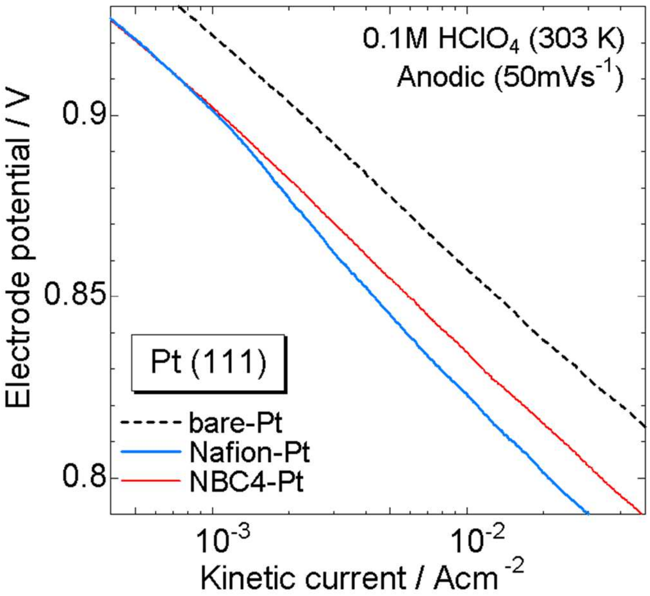

Fig. 5.3.6 The Tafel plots for the ORR kinetic currents.

Nafion-coated surface. The kinetic current for the NBC4-coated electrode is however, still significantly less than that for the bare surface (60 % less at 0.82 V), indicating that the electrode surface is still poisoned by NBC4. One of the poisoning species is probably sulfonimide anion as suggested by the broad anion-related peak in the CV (Fig. 5.3.4); sulfonimide anion has higher adsorptivity than perchlorate anion (Fig. 5.3.1). Poisoning with fluorinated parts of the polymer chain may also occur [22-25], although it is not detectable in the simple voltammetric analysis.

The kinetic current for the Nafion-coated surface approaches to that for the NBC4-coated surface with increasing of the electrode potential above 0.85 V and the latter surface shows, no longer, the ORR-improving effect above 0.90 V. Hence, the anion coverages on the two electrodes are likely equal in this potential range, where the hydroxyl, the formation of which is suppressed in the lower potentials, is finally formed even on the Nafion-coated Pt surface as shown by the peak at 0.9 V in the CV and some of the sulfonate may be desorbed instead [26, 27].

5.3.3 Conclusions

The catalyst poisoning property of a novel ionomer, NBC4, which has two sulfonimide acid groups in its side chain ended with a perfluorobutane, was compared with that of Nafion. The experiment was carried out using Pt (111) surfaced single crystal electrodes covered with the ionomer films. The CVs and ORR polarization curves showed the weaker anion adsorption and higher ORR activity by *ca*. 50 % at 0.82V (RHE) for NBC4 than for Nafion. The electrode surface is, however, still poisoned by NBC4, as shown by the significant suppression of the kinetic current caused by the NBC4 coating.

5.4 Molecular-scale understanding (Future work)

For elucidating the Pt/ionomer interface structure in a molecular scale, in-situ surface-enhanced infrared absorption spectroscopy (SEIRAS) [28] is a powerful tool, which can detect not only adsorbed anions, but also adsorbed or near-surface electrically neutral species, including perfluorinated parts in ionomer molecules. A past study using SEIRAS [29], however, showed no clear bands for the adsorbed sulfonate anion, probably because of the interference from an aqueous electrolyte of perchloric acid used over ionomer-coated Pt. To avoid this problem, a solid-state cell without liquid electrolytes was devised for SEIRAS in the present study.

5.4.1 Experimental

Spectroelectrochemical solid-state cell

The configuration of the solid-state cell is shown in Fig. 5.4.1 for SEIRAS measurements. The SEIRAS measurements were carried out with the Kretschmann attenuated total reflection (ATR) technique, where the infrared (IR) radiation was introduced from the behind of the working electrode (WE), an ionomer-coated Pt film deposited on an Si prism. A Nafion membrane (N117), which had been thoroughly cleansed by boiling it in 10% H_2O_2 twice and then in Milli-Q water three times, was pressed onto the WE by a Pt plate as a counter electrode (CE). A hydrogen-absorbed Pd wire (Pd/H_2) pressed onto the Nafion membrane was used as a reference electrode (RE). The concept of the solid-state cell for SEIRAS has already been presented in a study by Kunimatsu et al [30], where the focus of the analyses was on the mechanisms of ORR, not the adsorption of ionomor on Pt surface.

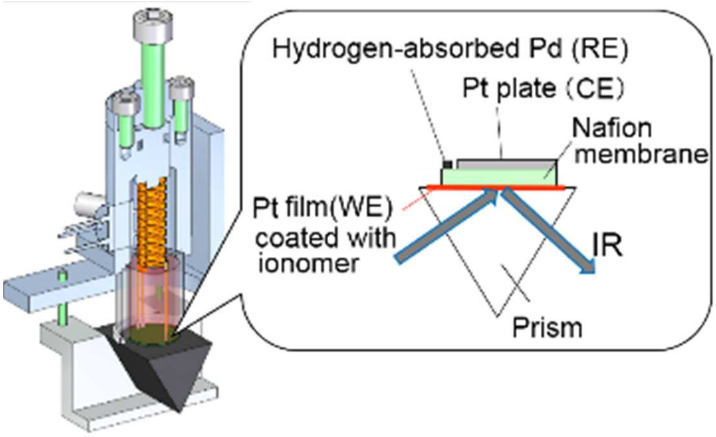

Fig.5.4.1 The configuration of the solid-state electrochemical cell for the SEIRAS measurements.

Preparation of ionomer-coated Pt film

The Pt film was prepared on the total-reflecting plane of the Si prism with a chemical (or electroless) deposition technique using a commercially available plating solution (LECTROLESS PT100®, Electroplating Engineering of Japan). An aliquot of 0.05 wt% aqueous Nafion dispersion prepared from a 5 wt% alcoholic solution (equivalent weight (EW): 1100 $g{\cdot}mol^{-1}$, Aldrich) was dropped on the Pt film and then dried at approximately 330 K. The ionomer-coating procedure was repeated until the ionomer-dropping region of the Pt film becomes completely covered by ionomer film. The ionomer-coated Pt film with the prism was subjected to a heat treatment at approximately 420 K, then potential-cycled between 0.08 - 1.4 V *vs.* reversible hydrogen electrode (RHE) in 0.1 M $HClO_4$ to clean the Pt surface, and finally assembled into the solid-state cell.

Pretreatment

After the assembly, the cell was saturated with Ar bubbled through water and then hydrogen was evolved on the Pd wire for 5 minutes by applying a voltage between the Pd wire and an auxiliary electrode of Pt wire. Thereafter the Pd wire showed a stable potential over 1 hr and was used as RE; the evolved hydrogen is expected to be absorbed and retained in the Pd wire. Afterward the WE of the Pt film was potential-cycled between 0.05 and 1.4 V to check the cleanness of the electrode surface.

SEIRAS measurement

SEIRA spectra were obtained using a Fourier transform infrared spectrometer (Bio-Rad, FTS 575C) equipped with a mercury cadmium telluride (MCT) detector. The spectrum at the electrode potential *E* is indicated in units of absorbance defined as $-\log(I/I_0)$, where I and I_0 are the intensities of the IR signals reflected from the total-reflecting plane of the Si prism at the potential *E* and a reference potential E_0, respectively.

5.4.2 Results

Cyclic voltammogram

Figure 5.4.2a shows the cyclic votammogram (CV) obtained with the solid-state cell at a scan rate of 50 mVs^{-1}. The shape of the CV is typical for a Pt polycrystalline electrode as characterized by the oxidation of underpotentially-deposited hydrogen (H_{upd}) between 0.05 – 0.3 V, double layer (DL) charging between 0.3 – 0.7 V, Pt hydroxide and/or oxide formation above 0.75 V in the positive sweep and their counter peaks in the negative sweep. The apparent roughness factor of the Pt film is calculated as 4.4.

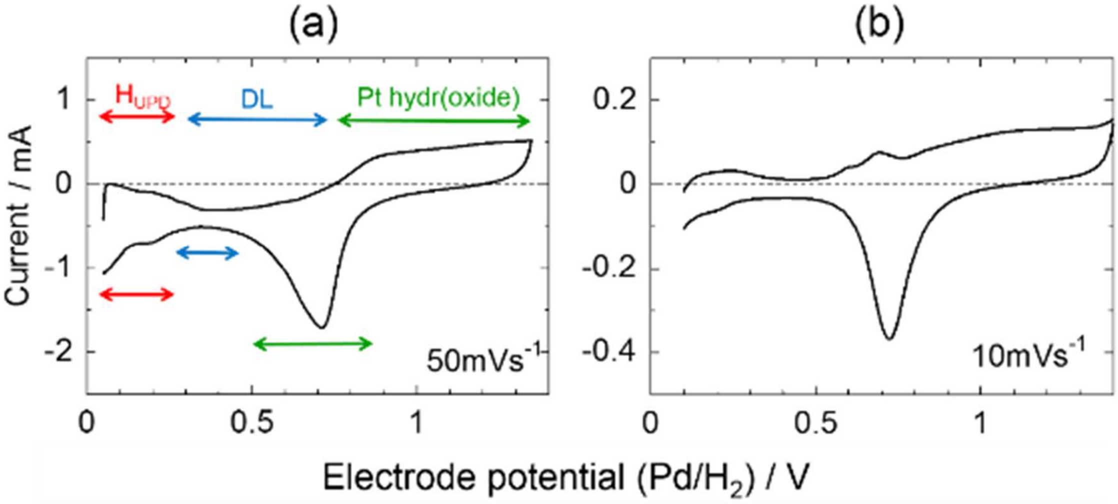

Fig.5.4.2 The CVs obtained with the solid cell at the scan rates of (a) 50 mVs^{-1} and (b) 10 mVs^{-1}.

The H_{upd} peak is dulled and additional minor peaks appear between 0.5 – 0.8 V at a lower scan rate, 10 mVs^{-1}, as shown in Fig. 5.4.2b, and these behaviors implicate the presence of organic impurities. Although the impurity effect could be weakened by increasing the scan rate, the SEIRAS measurements were carried out at the lower scan rate, 10 mVs^{-1}, to enhance the signal-to-noise ratio by increasing the number of interferograms to be coadded to a spectrum.

SEIRA spectra

Figure 5.4.3 shows the SEIRA spectra for the Nafion-coated Pt film in the solid-state cell collected during a potential sweep from 0.05 to 1.35 and back to 0.05 V (vs. Pd/H_2), where the spectrum at 0.05 V was used as the reference. Positive and negative bands, which quasi-reversibly grow and decay during the potential sweep, are observed in the spectral regions of A - D. As shown in Section 5.4.4, a bare Pt film in an aqueous electrolyte to which Nafion aqueous solution was dispersed, showed similar SEIRA spectra, although the band B was not observed with the Nafion dispersion.

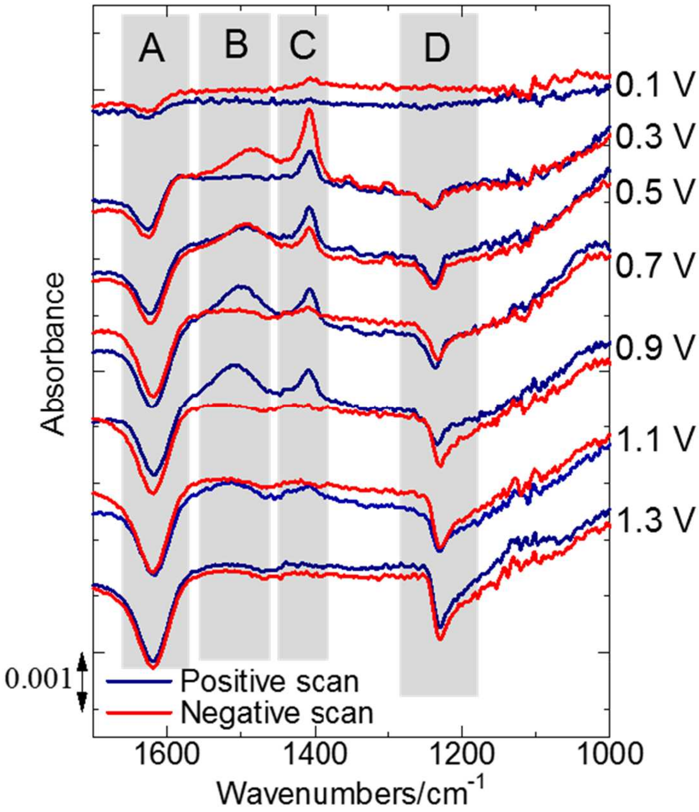

Fig.5.4.3 SEIRA spectra for the Nafion-coated Pt film in the solid-state cell collected during a potential sweep from 0.05 to 1.35 and back to 0.05 V (vs. Pd/H_2), where the spectrum at 0.05 V was used as the reference. The potential labeled at the right hand of each spectrum denotes the average potential where the spectrum was collected (*e.g.* the top two spectra labeled 0.1 V were obtained during the potential sweep between 0.05 – 0.15 V).

5.4.3 Discussion (Assignments)

Figure 5.4.4 shows the SEIRA spectrum for the Nafion-coated Pt film in the solid-state cell at 0.7 V, where the bands A – D are clearly seen. Reported frequencies of the bands for bulk Nafion, water and SiO_2 are indicated by gray zones as the benchmarks for band assignments [8, 31-33].

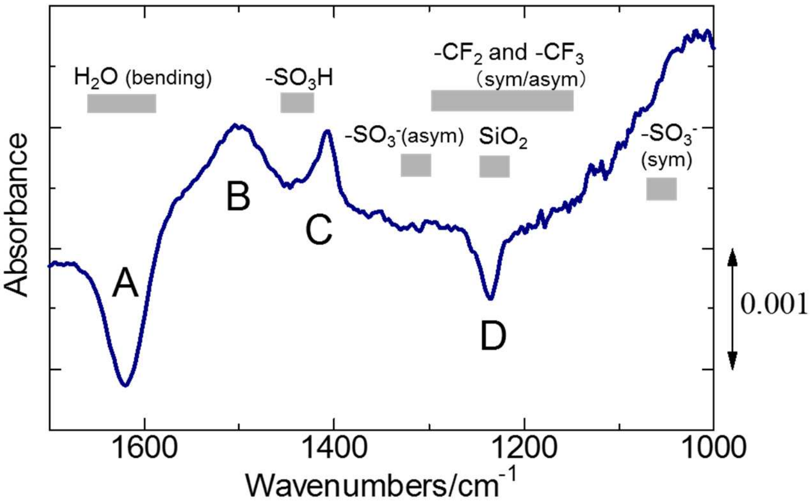

Fig.5.4.4 The SEIRA spectrum for the Nafion-coated Pt film in the solid-state cell at 0.7 V in the positive scan, where the spectrum at 0.05 V was used as the reference. Reported frequencies of the bands for bulk Nafion, water and SiO_2 are indicated by gray zones.

The band A is assigned to the bending mode of H_2O. Its negative growth with the increase in the electrode potential (Fig.5.4.3) implicates the starvation of water or the orientations of water molecules to less IR-active states at the Pt/Nafion interface. The band D can be ascribed to perfluorinated parts in Nafion molecule. However, since it only grows negatively against the spectrum at 0.05 V (Fig.5.4.3), where Pt surface is almost covered by H_{upd} and therefore any other species should not be adsorbed on the Pt surface, the perfluorinated parts do not seem to be adsorbed on Pt surface at any electrode potentials. Those frequency-based assignments, unfortunately, cannot be applied to the bands B and C, since their frequencies do not match any modes related to bulk Nafion, water and SiO_2. In the following, the origins of the bands B and C are discussed from the potential dependence of band intensity.

Figure 5.4.5 shows the integrated intensity of the band C, which was observed both with the solid cell (Fig. 5.4.3) and with the Nafion dispersion (see Section 5.4.4), as a function of the electrode potential. (The shape of the CV is also shown for comparison.) In the positive sweep, the intensity is increased with the oxidative removal of H_{upd}, reaches a plateau in the double layer region, and is decreased with the formation of Pt (hydr)oxide. In the negative sweep, the intensity is increased with the reduction of Pt (hydr)oxide, reaches a maximum at the end of the (hydr)oxide reduction, and is decreased with the formation of H_{upd}. This type of potential dependence has been also observed in SEIRAS analyses of the adsorption of sulfate anion on Pt surface [34, 35] and is a typical behavior for

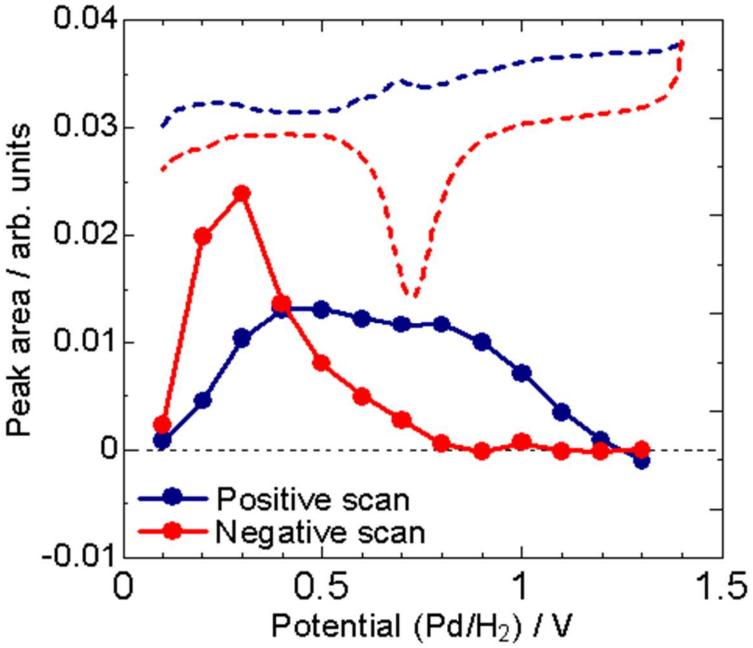

Fig.5.4.5 The peak area of the band C with the solid cell as a function of the electrode potential (solid line). The shape of the CV is also shown for comparison (dashed line).

the adsorption of any type of anions on Pt electrode, in which the adsorption reaction should compete with the formations of H_{upd} and Pt (hydr)oxide. In addition, voltammetric analyses with Pt single crystals have indicated that sulfonate anion of Nafion is adsorbed on the Pt surfaces in the double layer regions in previous studies [2, 4, 5, 7, 8, 19] and in Section 5.4.4. Thus, the behavior of the band C can be well-explained if it is assigned to adsorbed sulfonate anion. The band B grew and decayed in a similar way to the band C (Fig.5.4.3), and therefore is seemingly related to the adsorption of sulfonate anion. However, the band B was not observed in the SEIRA spectra with the Nafion dispersion (see Section 5.4.4), and further investigations are needed for clarifying its origin.

The frequency for the band C (1409 cm^{-1}) is significantly higher than that for sulfonate anion in the bulk Nafion (1320cm^{-1}) as shown in Fig.5.4.4. Therefore the adsorption reaction presumably causes a significant blue-shift of the anion band.

To further support this hypothesis, SEIRAS measurements were carried out using low-molecular-weight perfluoro-sulfonic acids of trifluoromethane sulfonic acid (CF_3SO_3H) and nonafluorobutane sulfonic acid ($C_4F_9SO_3H$) as discussed in Section 5.4.4 (see Fig. 5.4.9 and the corresponding text). As a result, however, the blue-shift has not yet been confirmed because the chosen model compounds were found not adsorptive on Pt surface. The tests with other types of low-molecular-weight perfluoro-sulfonic acids are underway and the results will be presented in the near future.

In the following sections, other possibilities for the assignment of the band C are discussed.

Possibility of undissociated sulfonic acid

In a past analysis of a Pt/Nafion interface with an Infrared Reflection Absorption Spectroscopy (IRRAS), Lipkowski et al also observed a peak at *ca*. 1400 cm^{-1} and assigned it to S=O stretching mode of undissociated form of sulfonic acid [36]. Indeed the frequency for the undissociated form of sulfonic acid is close to that for the band C (Fig. 5.4.4), but the applicability of this assignment to the present study is questionable, since our measurements were carried out under fully humidified conditions and all the acid groups should be dissociated [37].

Possibility of ORR intermediates

In the previous SEIRAS study on ORR mechanisms using the solid cell, the configuration of which is similar to that of the present cell, Kunimatsu et al. observed a peak at *ca*. 1400 cm^{-1} under O_2 saturated condition and ascribed it to reaction intermediates in ORR [30]. However, our measurements were carried out under the inert condition (saturated with Ar) and therefore, the band C is not due to ORR intermediates.

Possibility of acetate

In a past SEIRAS study on the oxidation of ethanol on Pt, Adzic et al. observed a band at *ca*. 1400 cm^{-1} and assigned it to the OCO symmetric stretching mode of acetate, a reaction intermediate (acetate is not further oxidized in the potential range examined) [38]. Alcohols are possible impurities from the Nafion chemicals used in the present study, and in fact, the CV during the SEIRAS measurement (Fig. 5.4.2b) implicates the presence of organic impurities. Thus, there is a concern that the band C is also due to intermediates of acetates during the oxidations of alcoholic impurities. For clarifying this point, further investigations (*e.g.* measurements with the intentional addition of ethanol) are underway.

5.4.4 Analyses in liquid systems

Analyses with Nafion dispersion

The behaviors of Nafion molecules at Pt electrode surface were also analyzed through voltammetry with a Pt (111) single crystal and the SEIRAS measurements with a bare Pt film using Nafion aqueous dispersion as electrolytes with a conventional liquid cell. The chemical was from Aldrich (10 wt% aqueous dispersion, EW: 1100 $g \cdot mol^{-1}$) and cleansed through boiling after the addition of H_2O_2 (to be 3 wt%) to oxidatively remove organic impurities. In the case of the SEIRAS measurements, the electrolyte of the Nafion dispersion was further cleansed by potential-cycling overnight with the working electrode after the assembling of the liquid cell.

Figure 5.4.6 shows the CV of a bare Pt (111) in the Nafion dispersion with the concentration of 10 meq./L (10 mM for sulfonic acid group) with the addition of $Ba(OH)_2$ (to be 2 mM for precipitating a possible impurity of sulfate anion as discussed in the next section, “Measurements with low-molecular-weight model compounds”). The CVs of Pt (111) surfaces with and without solid Nafion film in 0.1 M $HClO_4$ are also shown for comparison. The voltammogram in the Nafion dispersion shows reduction current due to residual oxygen and ill-defined features probably due to impurities. The Pt (111)-like H_{upd} plateau is, however, seen between 0.07 – 0.4 V and an anodic peak

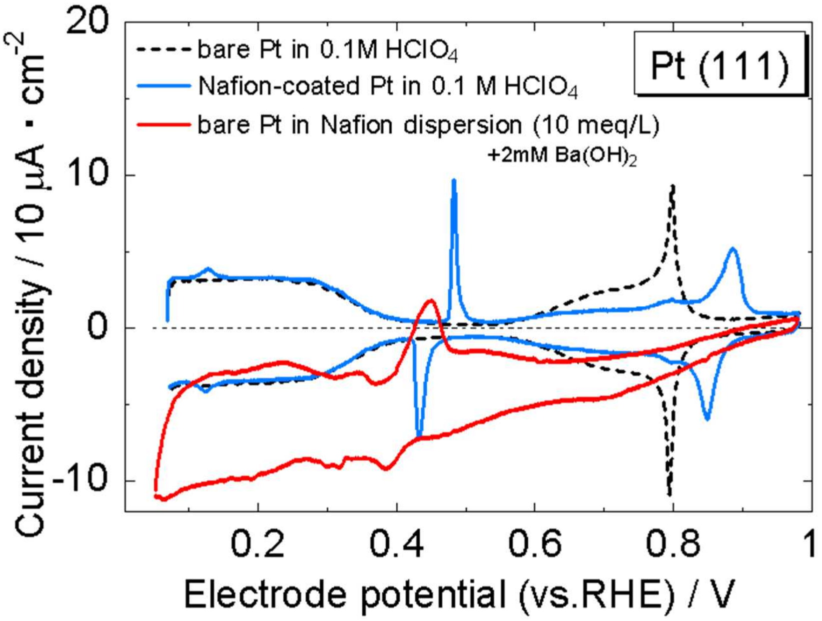

Fig.5.4.6 The CV of a bare Pt (111) in the Nafion dispersion with the concentration of 10 meq./L (10 mM for sulfonic acid group) with the additive of $Ba(OH)_2$ (red solid curve) . The CVs of Pt (111) surfaces with and without solid Nafion film in 0.1 M $HClO_4$ are also shown for comparison (blue solid and black dashed curves, respectively).

is observed at 0.43 V. The peak potential is close to that for sulfonate anion adsorption observed with the solid Nafion film (see the blue line and Section 5.1.2), and therefore the anodic peak in the Nafion dispersion is also ascribed to the sulfonate anion adsorption.

Figure 5.4.7 shows the SEIRA spectra for the bare Pt film in the Nafion dispersion during a potential sweep. The three bands A, C and D are again observed although the relative intensities of the three bands are different from those with the solid cell shown in Fig. 5.4.3. Figure 5.4.8 shows the peak area of the band C for the Nafion dispersion as a function of the electrode potential and the corresponding CV. Note that the CV does not show an anodic peak in the double layer region, which was observed in the solid cell and ascribed to organic impurities (Fig. 5.4.5), and implicates that the SEIRA spectra with the Nafion dispersion have not been interfered from impurities. The band intensity for the Nafion dispersion is maximized in the double layer regions as in the case of the results for the solid state cell (Section 5.4.3). Therefore, the band C is likely due to adsorbed sulfonate anion as suggested by the adsorption peak in the CV for Pt (111) surface (Fig. 5.4.6).

Measurements with low-molecular-weight model compounds

The hypothesis of the blue-shift for the anion band was tested using low-molecular-weight perfluoro-sulfonic acids. Because the most basic perfluorinated sulfonic acid, CF_3SO_3H (trifluoromethane sulfonic acid, TFMSA), has already been reported to be non-adsorbing electrolyte from voltammetries using Pt single crystal electrodes by Berná et al. [39], and the result was also reproduced in our

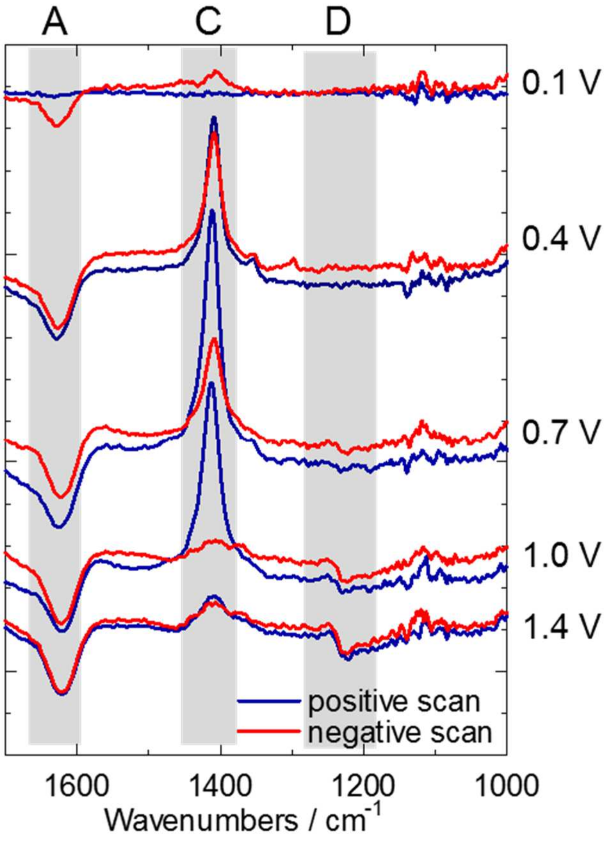

Fig.5.4.7 SEIRA spectra for the bare Pt film in the Nafion aqueous dispersion during a potential sweep, where the spectrum at 0.05 V was used as the reference. Blue line: positive scan. Red line: negative scan.

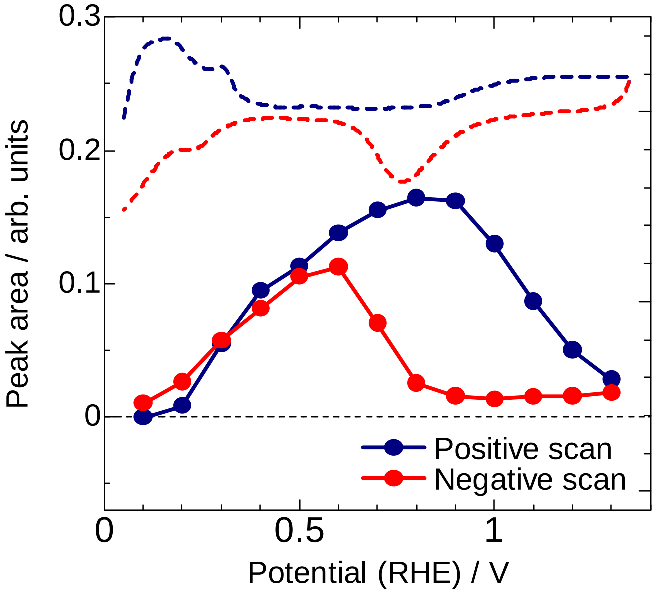

Fig.5.4.8 The peak area of the band C for the Nafion dispersion as a function of the electrode potential (solid line). The shape of the CV is also shown for comparison (dashed line).

laboratory (Fig. 5.4.9a), a larger perfluorinated sulfonic acid, $C_4F_9SO_3H$ (nonafluorobutane sulfonic acid, NFBSA) was chosen as the model compound in the present study.

Figure 5.4.9b shows the CVs for a Pt (111) single crystal electrode in 0.1 M NFBSA (Tokyo Chemical Industry, 98.0 %) and in 0.1 M $HClO_4$, the latter of which is already known to be non-adsorbing electrolyte. A small amount of $Ba(OH)_2$ has been added to be 2 mM to precipitate, as $BaSO_4$,

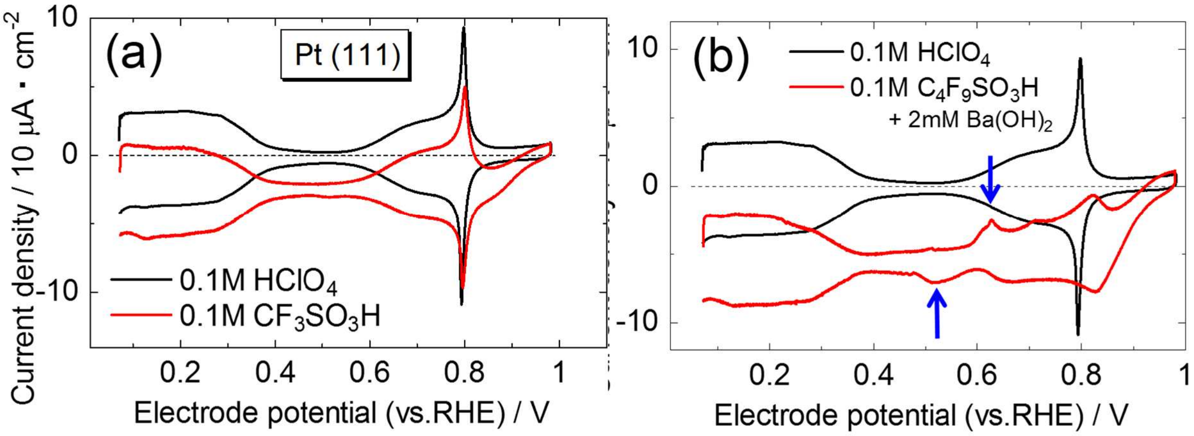

Fig. 5.4.9 The CVs of a bare Pt (111) in (a) 0.1 M TFMSA and (b) 0.1 M NFBSA with the additive of $Ba(OH)_2$ (red solid curves) . The CV in 0.1 M $HClO_4$ is also shown for comparison (black solid curves).

an impurity of sulfate anions, which was found to be contained with non-negligible concentration, <3000 ppm (corresponding to <1 mM for the 0.1 M NFBSA) in this type of chemical. (The validity of this precipitation treatment is discussed in Fig. 5.4.10 and its caption.) As shown by the blue arrows in Fig. 5.4.9b, small peaks are observed at 0.6 V in the positive sweep and at 0.5 V in the negative sweep, and can be ascribed to the adsorption and desorption of either the NFBSA anion, $C_4F_9SO_3^-$, or the impurity of sulfate anion that could not be precipitated by the addition of $Ba(OH)_2$.

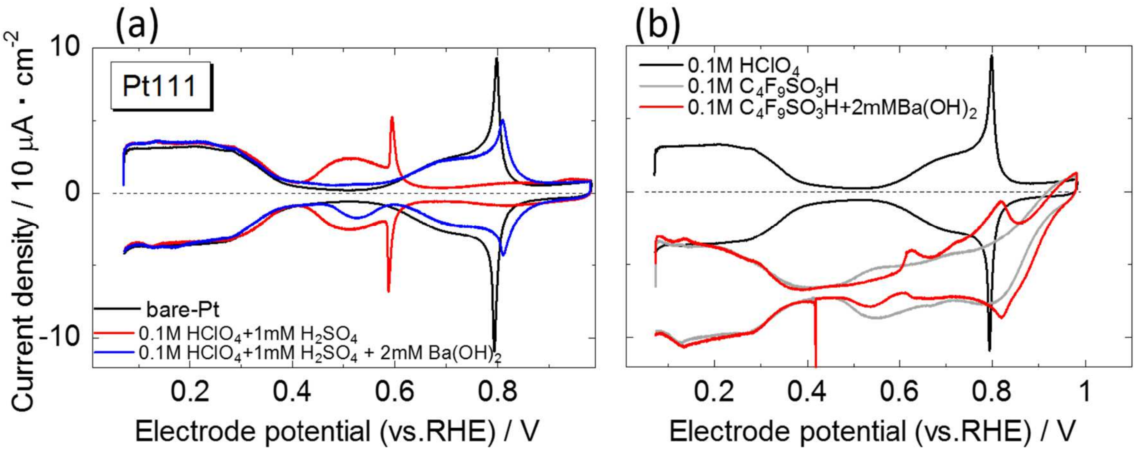

Fig. 5.4.10 The effect of the addition of Ba cation for precipitating the impurity of sulfate anion. (a) Sulfate anion with the concentration of 1 mM is significantly adsorbed on Pt (111) as shown by the appearance of sulfate-derived butterfly peaks between 0.4 – 0.6 V and the disappearance of hydroxide-derived ones between 0.6 -0.85 V in the red curve. With the addition of 2 mM of $Ba(OH)_2$, the sulfate-derived butterfly peaks attenuate and the hydroxide-derived ones re-appear. The suppression of the adsorption of sulfate anions is surely due to precipitation of sulfate anion with Ba cations. (b) The CV of Pt (111) in 0.1 M NFBSA without the additive of $Ba(OH)_2$ (gray solid curve) shows broad peaks between 0.5 – 0.8 V and the disappearance of the hydroxide-derived butterfly peaks. The broad peak is attenuated by the addition of $Ba(OH)_2$ (red solid curve) and therefore ascribed to the impurity of sulfate anion.

Figure 5.4.11a shows the SEIRA spectrum in 0.1 M NFBSA. Several positive bands with various intensities are observed above 0.3 V. The profiles (frequency, potential dependency of the intensity) of the bands at 1100 and 1200 cm^{-1} (gray-shaded regions) are quite similar to those for adsorbed sulfate on Pt [34] and therefore indicate that sulfate anion still exists as impurity in the electrolyte despite the precipitation treatment. The small peaks at 0.5 - 0.6 V in the CV of Pt (111) is likely to be ascribed to the impurity of sulfate anion as well, and because no other anion-related peaks are observed in the CV, NFBSA as well as TFMSA is likely a non-adsorbing species. In this case, the other positive bands at 1066, 1140, 1250 and 1350 cm^{-1} can be ascribed to the orientations of NFBSA molecules to more IR-active states, not to their adsorptions on the Pt surface. (Positive bands even for non-adsorbing species are exemplified by SEIRA spectra for TFMSA (Fig. 5.4.11b).) Therefore, the possibility of the adsorption-induced blue shift cannot be discussed using this model compound.

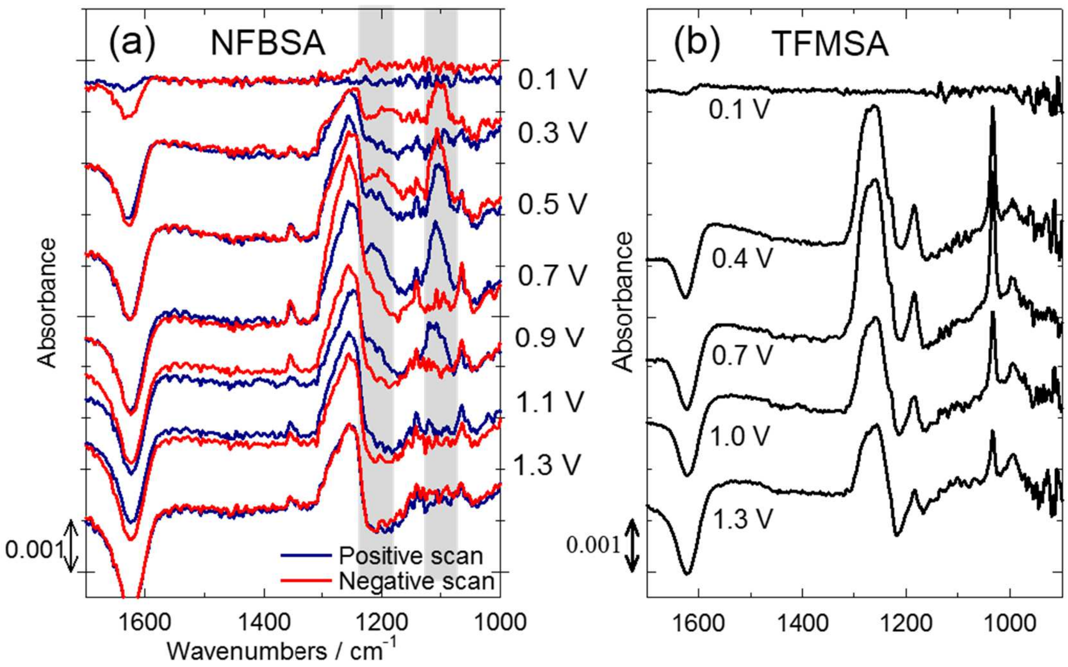

Fig.5.4.11 SEIRA spectra for the Pt film in (a) 0.1 M NFBSA and in (b) 0.1 M TFMSA collected during potential sweeps, where the spectrum at 0.05 V was used as the reference.

5.4.5 Conclusions

A Pt/Nafion interface was analyzed with SEIRAS using a solid-state electrochemical cell and band assignments in the spectra were discussed. A new band was observed at *ca.* 1400 cm^{-1} and the potential dependency of the band intensity suggests that it is due to adsorbed sulfonate anion in Nafion molecule on the Pt surface. Perfluorinated parts, in contrast, do not seem to be adsorbed on Pt.

5.5 References

[1] N.M. Markovic, P.N. Ross, *Surf. Sci. Rep.*, **45** (2002) 121 .

[2] R. Subbaraman, D. Strmcnik, A.P. Paulikas, V.R. Stamenkovic, N.M. Markovic, *ChemPhysChem*, **11** (2010) 2825 .

[3] D.S. Strmcnik, D.V. Tripkovic, D. van der Vliet, K.C. Chang, V. Komanicky, H. You, G. Karapetrov, J. Greeley, V.R. Stamenkovic, N.M. Markovic, *J. Am. Chem. Soc.*, **130** (2008) 15332 .

[4] M. Ahmed, D. Morgan, G.A. Attard, E. Wright, D. Thompsett, J. Sharman, *J. Phys. Chem. C*, **115** (2011) 17020 .

[5] R. Subbaraman, D. Strmcnik, V. Stamenkovic, N.M. Markovic, *J. Phys. Chem. C*, **114** (2010) 8414 .

[6] B.D. Cahan, H.M. Villullas, *J. Electroanal. Chem.*, **307** (1991) 263 .

[7] K. Kodama, R. Jinnouchi, T. Suzuki, H. Murata, T. Hatanaka, Y. Morimoto, *Electrochem. Commun.*, **36** (2013) 26 .

[8] A.M. Gómez-Marín, A. Berná, J.M. Feliu, *J. Phys. Chem. C*, **114** (2010) 20130 .

[9] A.J. Bard, L.R. Faulkner, *Electrochmical methods, Fundamentals and Applications, 2nd ed.*, Wiley, (2001) .

[10] A. Parthasarathy, C.R. Martin, S. Srinivasan, *J. Electrochem. Soc.*, **138** (1991) 916 .

[11] V.I. Basura, P.D. Beattie, S. Holdcroft, *J. Electroanal. Chem.*, **458** (1998) 1 .

[12] A.E.S. Sleightholme, A. Kucernak, *Electrochim. Acta*, **56** (2011) 4396 .

[13] W. Paik, T.E. Springer, S. Srinivasan, *J. Electrochem. Soc.*, **136** (1989) 644 .

[14] A. Björling, E. Ahlberg, J.M. Feliu, *Electrochem. Commun.*, **12** (2010) 359 .

[15] T.A. Zawodzinski, M. Neeman, L.O. Sillerud, S. Gottesfeld, *J. Phys. Chem.*, **95** (1991) 6040 .

[16] T. Yoda, T. Shimura, B. Bae, K. Miyatake, M. Uchida, H. Uchida, M. Watanabe, *Electrochim. Acta*, **54** (2009) 4328 .

[17] T. Yoda, T. Shimura, B. Bae, K. Miyatake, M. Uchida, H. Uchida, M. Watanabe, *Electrochim. Acta*, **55** (2010) 3464 .

[18] T. Omata, M. Tanaka, K. Miyatake, M. Uchida, H. Uchida, M. Watanabe, *ACS Applied Materials & Interfaces*, **4** (2012) 730 .

[19] K. Kodama, A. Shinohara, N. Hasegawa, K. Shinozaki, R. Jinnouchi, T. Suzuki, T. Hatanaka, Y. Morimoto, *J. Electrochem. Soc.*, **161** (2014) F649 .

[20] A. Shinohara, K. Kudo, M. Kawasumi, Y. Morimoto, N. Hasegawa, *ECS Transactions*, **58** (2013) 253 .

[21] N.M. Markovic, R.R. Adzic, B.D. Cahan, E.B. Yeager, *J. Electroanal. Chem.*, **377** (1994) 249 .

[22] I. Kendrick, D. Kumari, A. Yakaboski, N. Dimakis, E.S. Smotkin, *Journal of the American Chemical Society*, **132** (2010) 17611 .

[23] T. Masuda, H. Fukumitsu, T. Kondo, H. Naohara, K. Tamura, O. Sakata, K. Uosaki, *The*

Journal of Physical Chemistry C, **117** (2013) 12168 .

[24] D. Damasceno Borges, A.A. Franco, K. Malek, G. Gebel, S. Mossa, *ACS Nano*, **7** (2013) 6767 .

[25] D. Damasceno Borges, K. Malek, S. Mossa, G. Gebel, A.A. Franco, *ECS Transactions*, **45** (2013) 101 .

[26] T. Masuda, K. Ikeda, K. Uosaki, *Langmuir*, **29** (2013) 2420 .

[27] T. Masuda, F. Sonsudin, P.R. Singh, H. Naohara, K. Uosaki, *J. Phys. Chem. C*, **117** (2013) 15704 .

[28] M. Osawa, *Bull. Chem. Soc. Jpn.*, **70** (1997) 2861 .

[29] Y. Ayato, K. Kunimatsu, M. Osawa, T. Okada, *J. Electrochem. Soc.*, **153** (2006) A203 .

[30] K. Kunimatsu, T. Yoda, D.A. Tryk, H. Uchida, M. Watanabe, *Phys. Chem. Chem. Phys.*, **12** (2010) 621 .

[31] C.K. Byun, I. Sharif, D.D. DesMarteau, S.E. Creager, C. Korzeniewski, *J. Phys. Chem. B*, **113** (2009) 6299 .

[32] N. Idupulapati, R. Devanathan, M. Dupuis, *J. Phys. Chem. A*, **114** (2010) 6904 .

[33] S.M. Hu, *J. Appl. Phys.*, **51** (1980) 5945 .

[34] M. Osawa, M. Tsushima, H. Mogami, G. Samjeske, A. Yamakata, *J. Phys. Chem. C*, **112** (2008) 4248 .

[35] R. Jinnouchi, T. Hatanaka, Y. Morimoto, M. Osawa, *Phys. Chem. Chem. Phys.*, **14** (2012) 3208 .

[36] D. Malevich, V. Zamlynny, S.G. Sun, J. Lipkowski, *Z. Phys. Chem*, **217** (2003) 513 .

[37] M. Laporta, M. Pegoraro, L. Zanderighi, *Phys. Chem. Chem. Phys.*, **1** (1999) 4619

[38] M.H. Shao, R.R. Adzic, *Electrochim. Acta*, **50** (2005) 2415 .

[39] A. Berná, J.M. Feliu, L. Gancs, S. Mukerjee, *Electrochem. Commun.*, **10** (2008) 1695 .

Chapter 6

General conclusions and outlook

The effects of the three types of adsorbed or near-surface species on Pt electrode, oxygenated species, hydrated cations and specifically adsorbed anions, on the kinetics of various electrocatalytic reactions related to polymer electrolyte fuel cells, were studied.

The study started with the analyses of simple systems of interfaces between Pt and aqueous electrolytes, focusing on oxygenated species, which are also practically called the Pt (hydr)oxide. In particular, the kinetics of oxide formation reaction and the roles of reaction intermediates in ORR are analyzed on the model surface of Pt (111). Oxide formation reaction current density on Pt (111) was estimated by time-differentiating oxide growth curves at different constant potentials and the oxide coverage below 0.35 ML. The Tafel slope was 18 - 24 mV·decade^{-1} under the condition where the Tafel plot is on a straight line. The reaction mechanism accounting for this small slope was proposed, in which the oxide formation process is assumed as a combination of a fast electron transfer step and a following slow step. The reaction order of ORR on Pt (111) was experimentally estimated as a function of the electrode potential in an acid and in an alkaline electrolytes. The reaction order is approximately 1 over the range of the electrode potential of 0.82 - 0.96 V (RHE) in acid, while it is significantly lower than 1 in alkaline. The first-order kinetics in acid indicates that oxygenated species as reaction intermediates are not accumulated with the increase in O_2 concentration and the ORR kinetics can be discussed on the basis of coverage with spectator species (including adsorbed anion and Pt oxide formed from water).

The effects of cations on several types of electrochemical reactions were investigated in alkaline solution. Traditionally, alkali (earth) cations have been regarded as non-influential species on Pt surface because they are stably hydrated and do not form covalent bonding with Pt. However, they were found to strongly affect some types of electrochemical reactions by non-covalent interactions between OH_{ad} and $M^+(H_2O)_x$. The effect increases in the same order as the hydration energies of the included cations ($Li^+ >> Na^+ > K^+(> Cs^+)$) as indicated by the inverse trend in the reaction rates ($((Cs^+) > K^+ > Na^+ >> Li^+)$) for the oxidation of methanol as well as ORR and HOR, which can be explained by higher concentration of OH_{ad}-$M^+(H_2O)_x$ clusters as spectators near the electrode surface for cation with larger hydration energy. For investigating the relationship between the coverage of OH_{ad} and the effect of non-covalent interaction, the cation effect on bulk CO oxidation on Pt surface in alkaline solution was investigated. The non-covalent effect of the added cations was not observed when the surface is highly covered with CO_{ad}, because of lowered OH_{ad} coverage by CO_{ad}. Once the CO_{ad} layer was stripped by oxidation, electrode surface was available for adsorption of OH_{ad}, and interaction with cations from the solution; bulk CO oxidation was promoted in the presence of Li^+ and Ba^{2+}, and the non-covalent interaction effect was demonstrated. Thus OH_{ad} coverage seems to play an important role in the formation of the OH_{ad}-hydrated cation clusters. As a new topic of CO-oxidation catalyst with high activity, trace levels of Cu^{2+} were found to dramatically increase the rate of the reaction through an oxidized form of copper on the Pt surface; the oxidation potential is shifted roughly 0.5 V more negative, to 0 V vs. RHE, by providing the necessary sites for the adsorption of OH as reactant.

The interface between ionomer and Pt, where anions in the ionomer molecule always exist, was investigated as a more practical research for developing PEFCs. The effect of Nafion coating on ORR on Pt (111) was quantitatively analyzed on a Pt (111) surface uniformly covered by a Nafion thin film. Sulfonate anions in the Nafion molecules are adsorbed on the electrode surface above 0.5 V (RHE) with a coverage of 0.07 monolayer. The ORR kinetic current is decreased by 73 % at 0.82 V and by 54 % at 0.90 V by the Nafion coating ("poisoning effect"). For studying the ionomer effects under more realistic conditions, the anion adsorption property on Pt (111) in various hydration states of Nafion was analyzed in a newly-developed solid-state electrochemical cell. With dehydration of the ionomer, peaks for adsorption and desorption of the sulfonate anions in the cyclic voltammogram (CV) showed significant shifts to lower potentials, which indicate the increase in the anion adsorptivity. As another promising ionomer, the catalyst poisoning property of a novel ionomer, NBC4, which has two sulfonimide acid groups in its side chain ended with a perfluorobutane, was compared with that of Nafion. The CVs and ORR polarization curves on Pt (111) showed weaker anion adsorption and higher ORR activity by *ca*. 50 % at 0.82V (RHE) for NBC4 than for Nafion. The electrode surface is, however, still poisoned by NBC4, as shown by a significant suppression of the kinetic current caused by the NBC4 coating. For elucidating the Pt/ionomer interface structure in a molecular scale, surface enhanced infrared absorption spectroscopy (SEIRAS) was applied. A new band was observed at *ca.* 1400 cm^{-1} and the potential dependency of the band intensity suggests that it is due to adsorbed sulfonate anion in Nafion molecule on the Pt surface. Perfluorinated parts, in contrast, do not seem to be adsorbed on Pt.

As a conclusion, the spectators that affect electrochemical reactions can be classified into either covalently bonded species such as oxygenated species (Chapter 3) and specifically adsorbed anions (Chapter 5), or non-covalently bonded species such as hydrated cations (Chapter 4). Those spectator species usually block the accesses of reactants to the electrode surface (Fig. 6.1) and therefore suppress most reactions, except for some special cases including the oxidation of CO in low coverage, which is promoted by the non-covalent interaction between adsorbed OH and hydrated cations. These comprehensive understanding of the interface will provide a foundation for more practical researches such as an appropriate tuning of the properties of Pt/ionomer interface in PEFCs.

In the developments of proton-exchange-type PEFCs, oxygenated species and anions of ionomer molecules play significant roles at the Pt/ionomer interfaces. In the studies following this thesis, further investigations of characters of those species will be conducted to find the strategies for maximizing the electrocatalytic performance.

The next stages in the studies of Pt (hydr)oxide are the analyses on real catalysts of Pt nanoparticles, where the oxophilicities of low-coordinated Pt atoms at the edges are different from those of facet Pt atoms [1, 2]. In this respect, the analyses on model surfaces with steps (high-index single crystals) will be also informative [3, 4]. The studies of oxygenated species as ORR intermediates are also critically important not only from scientific interests but also for the development of high-performance electrolcatalyst. A recent study using ambient pressure X-ray photoelectron spectroscopy showed that the types of adsorbed hydroxyl during ORR is not unique and were classified into hydrated

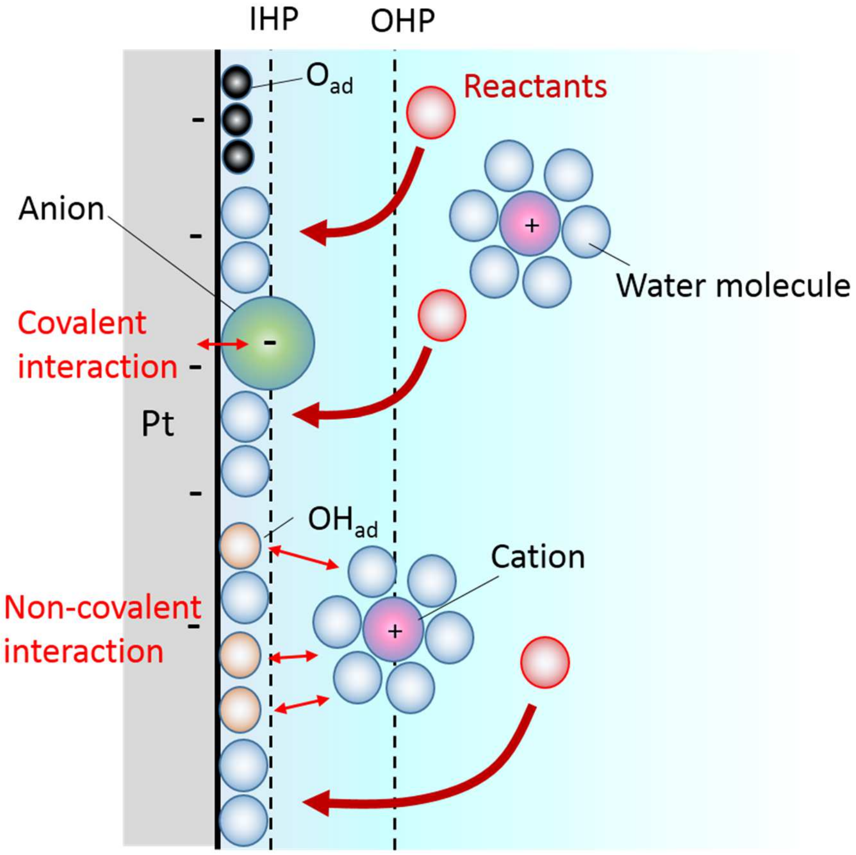

Fig. 6.1 The overview of the interface between Pt and electrolyte.

OH_{ad} and non-hydrated OH_{ad}, the latter of which requires smaller overpotentials for the reduction reaction [5]. This result indicates that tuning the hydration states of the intermediates can significantly improve the ORR kinetics and therefore, that it is important to modify not only the property of electrode side but also that of electrolyte side.

In the studies of Pt/ionomer interface, whether perfluorinated parts in ionomer molecule are adsorbed on Pt surface and block ORR or not still remains elusive. SEIRAS is a promising method to clarify this point as described in Section 5.4. In addition to those analytical studies, developmental researches such as the measurements of catalyst poisoning properties of novel ionomers are also important since the proposed less-adsorptive ionomer, NBC4 (Section 5.3), was found to still suppress ORR and further improvements of the ionomer performance are required.

References

[1] M.H. Shao, A. Peles, K. Shoemaker, *Nano Lett.*, **11** (2011) 3714 .

[2] F.J. Perez-Alonso, D.N. McCarthy, A. Nierhoff, P. Hernandez-Fernandez, C. Strebel, I.E.L. Stephens, J.H. Nielsen, I. Chorkendorff, *Angew. Chem.-Int. Edit.*, **51** (2012) 4641 .

[3] R. Jinnouchi, K. Kodama, Y. Morimoto, *J. Electroanal. Chem.*, **716** (2014) 31 .

[4] A.S. Bandarenka, H.A. Hansen, J. Rossmeisl, I.E.L. Stephens, *Phys. Chem. Chem. Phys.*, **16** (2014) 13625 .

[5] H.S. Casalongue, S. Kaya, V. Viswanathan, D.J. Miller, D. Friebel, H.A. Hansen, J.K. Norskov, A. Nilsson, H. Ogasawara, *Nat. Commun. 4*, (2013) .

Appendix

A. Estimation of reaction order of ORR

A.1 Derivation of Eq. 3.2.3

A mass balance is maintained at the electrode surface under the stationary condition (Fig. A1);

$$\frac{i}{nF} = \dot{r} = j \qquad \text{(A1)}$$

where n is the number of electrons for the reduction of one O_2 molecule, F is the Faraday constant and j is the flux of O_2 into the interface from the electrolyte.

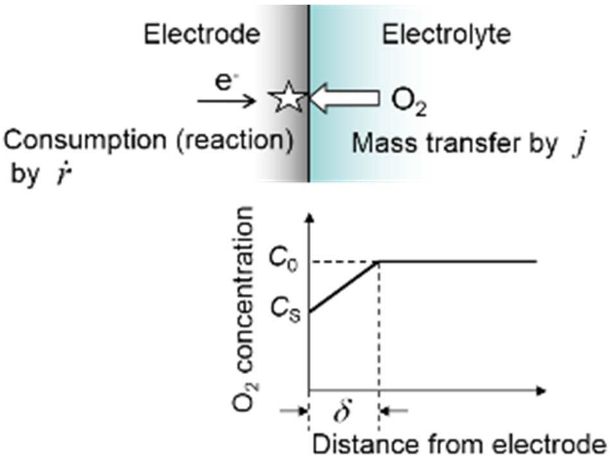

Fig. A1 A mass balance at the interface.

$\dot{r}$ can be described by the rate equation in the form including the reaction order:

$$\dot{r} = k' C_S^{\gamma} \qquad \text{(A2)}$$

, where k' is reaction rate constant for the γ.- included form (not identical to k in Eq. 3.2.2).

The flux is proportional to the concentration gradient in the diffusion layer in the electrolyte:

$$j = D\frac{C_0 - C_S}{\delta} \qquad \text{(A3)}$$

where D is the diffusion coefficient of O_2 in the electrolyte, C_0 the bulk concentration of O_2 in the electrolyte, C_S the concentration of O_2 at the electrode surface and δ the thickness of the diffusion layer.

Equation A3 can be rewritten as,

$$C_S = C_0\left(1 - \frac{j}{j_d}\right) \qquad \text{(A4)}$$

where j_d is defined as DC_0/δ and equals to the mass flux under the diffusion limiting condition.

j/j_d equals to i/i_d when the number of electron in ORR in the kinetics-effective region (region III in Fig. 3.2.3) is equal to that in the diffusion limiting region (region II in Fig.3.2.3); this has been found to be true from studies using rotating ring-disk electrode technique [1]. Therefore,

$$C_\mathrm{S} = C_0\left(1 - \frac{i}{i_\mathrm{d}}\right) \qquad \text{(A5)}$$

Substituting Eq. A5 into Eq. A2 and using Eq. A1,

$$i = nFkC_0^{\ \gamma}\left(1 - \frac{i}{i_\mathrm{d}}\right)^{\gamma} \qquad \text{(A6)}$$

This equation can be rewritten as,

$$i = nFkC'_0{}^{\gamma}\left\{\left(\frac{C_0}{C'_0}\right)\left(1 - \frac{i}{i_\mathrm{d}}\right)\right\}^{\gamma} \qquad \text{(A7)}$$

in which C'_0 is the standard bulk concentration of O_2 in the electrolyte. C_0/C_0 is equal to $i_\mathrm{d}/i'_\mathrm{d}$ when the electrode rotation rate is equal to that in the standard concentration of O_2 (and hence the thickness of the diffusion double layer is equal to that in the standard concentration of O_2) as in the case in the present analysis.

$$\frac{i_\mathrm{d}}{i'_\mathrm{d}} = \frac{nFDC_0/\delta}{nFDC'_0/\delta} = \frac{C_0}{C'_0} \qquad \text{(A8)}$$

Therefore (A7) can be rewritten as

$$i = nFkC_0^{\ \gamma}\left\{\left(\frac{i_\mathrm{d}}{i'_\mathrm{d}}\right)\left(1 - \frac{i}{i_\mathrm{d}}\right)\right\}^{\gamma} \qquad \text{(A9)}$$

Taking the logarithm of the equation (A9),

$$\ln i = \gamma \ln\left\{\left(\frac{i_\mathrm{d}}{i'_\mathrm{d}}\right)\left(1 - \frac{i}{i_\mathrm{d}}\right)\right\} + \ln nFkC_0^{\ \gamma} \qquad \text{(A10)}$$

The terms of $\{i_\mathrm{d}(1 - i/i_\mathrm{d})/i'_\mathrm{d}\}$ is equal to C_S/C_0, the ratio of O_2 concentration at the electrode surface to the standard O_2 bulk concentration, the latter of which is constant through the present analysis, and therefore is the non-dimensional form of the O_2 concentration at the electrode surface described by current density. The term of $nFkC_0^{\ \gamma}$ is the current density if the concentration of O_2 at the interface was equal to the standard bulk concentration, the so-called "kinetic current density i'_k" in the standard concentration, which only depends on the electrode potential. Thus Eq. 3.2.3 was derived.

A.2 Illustration of analysis

A.2.1 Subtraction of CV

Voltammograms of ORR current densities were obtained by subtracting the current density of the CV in the positive scan from the current densities of LSVs of ORR (see Eq. (3.2.4)). The results in the potential region between 0.92 - 1.00 V is shown in Fig. A2.

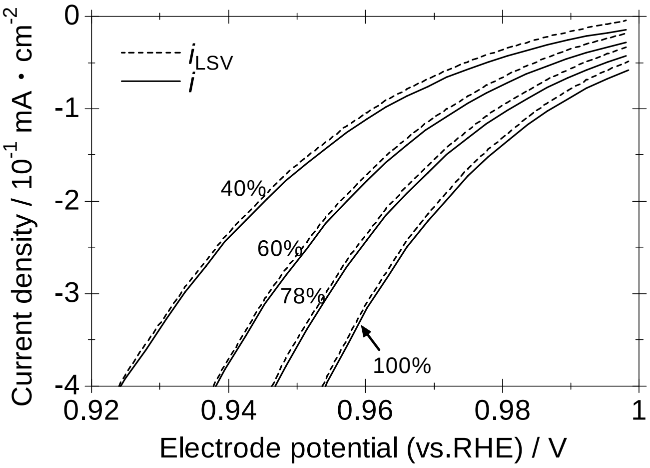

Fig. A2 The subtraction of CV from LSVs of ORR in 0.1M $HClO_4$.

A.2.2 Data sampling

We read the values of the voltammograms of the ORR current densities at a certain potential (Fig. A3). i_d is the current density of each LSV in the potential region II in Fig. 3.2.3.

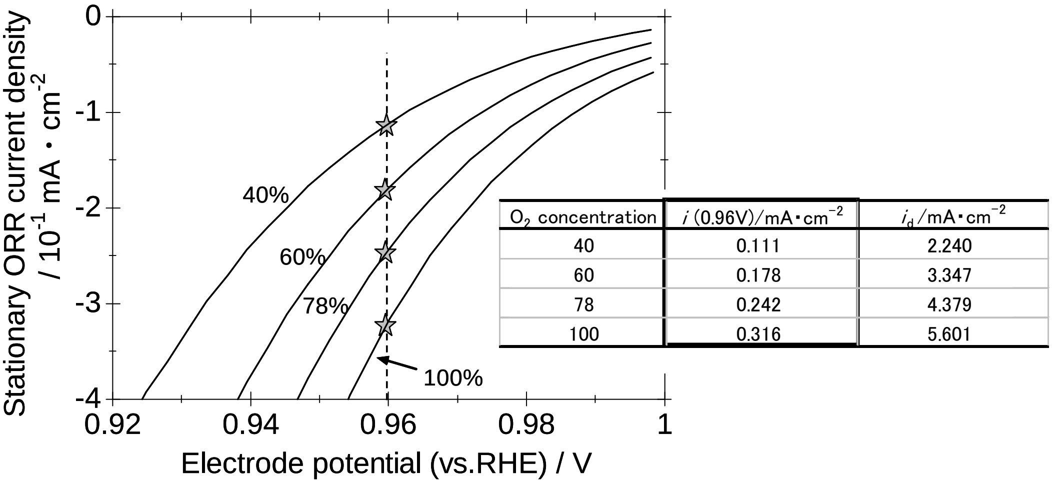

O_2 concentration	i (0.96V)/mA・cm^{-2}	i_d /mA・cm^{-2}
40	0.111	2.240
60	0.178	3.347
78	0.242	4.379
100	0.316	5.601

Fig. A3 The illustration of a data sampling. We read the values of ORR current densities at the points marked with the stars as the data at the electrode potential of 0.96 V in 0.1M $HClO_4$.

A.2.3 Fitting

Fig. A4 shows the plots $\ln i$ *vs.* $\ln\{i_d(1-i/i_d)/i'_d\}$ at the electrode potential of 0.96 V in 0.1 M $HClO_4$ and the fitting straight line for these plots. In this way, the reaction order at the electrode potential of 0.96V was obtained from the slope of this fitting line.

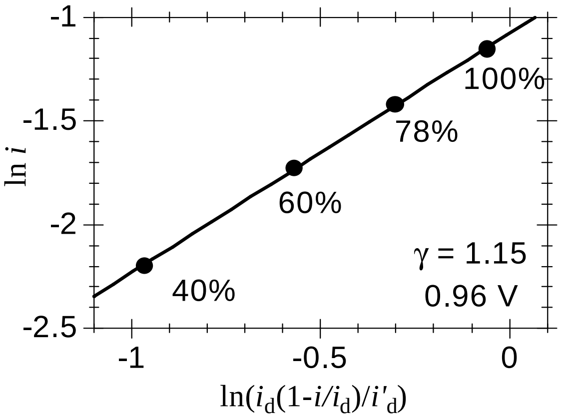

Fig. A4 The illustration of fitting. The slope of the fitting straight line is equal to the reaction order γ.

B. Key points for forming the uniform ionomer film

The key points for forming the uniform ionomer film on Pt electrode (Section 5.1) are discussed in the following.

B.1 DMF

Fig. B1 shows the effect of the addition of DMF to the Nafion solution on the film uniformity. The Nafion film is significantly segregated and the uniformity is very poor without DMF (Fig. B1a). By adding DMF (Fig. B1b), the surface becomes more widely covered with Nafion (The covering is still not perfect because the amount of the dropped solution is smaller than the case in Fig. 5.1.1).

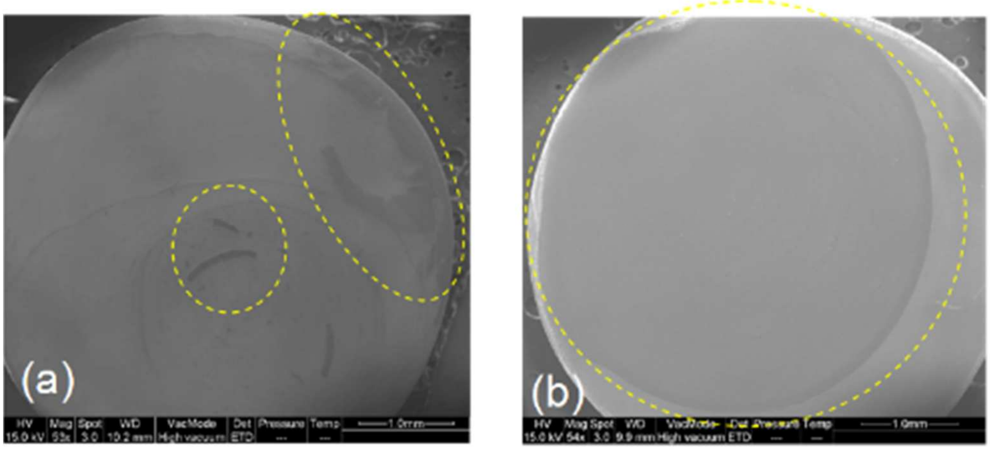

Fig. B1 The effect of the addition of DMF to the Nafion solution. (a): without DMF, (b): with DMF. The Nafion flims are seen in the dashed circles. The dropping amount of the 0.005 wt % Nafion solution is 10 μL.

B.2. Drying temperature

Fig. B2 shows the SEM image of a Nafion-coated Pt (111) surface where the Nafion solution was dried at 390 K, 12 K higher than the case in Fig. B1b. The Nafion film wrinkled probably because the drying of the Nafion solution was too quick.

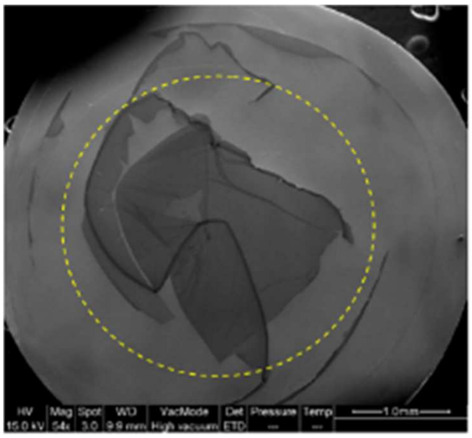

Fig. B2 SEM image of a Nafion–coated Pt (111) surface where the Nafion solution was dried at 390 K.

B.3. Heat treatment

Fig. B3 shows the SEM image of a Nafion–coated Pt (111) surface after the electrochemical measurement where the film was not heat-treated after the drying process. The film is seriously removed probably because the physico-mechanical stability of the film is not sufficient without the heat-treatment at the temperature above the glass-transition point of Nafion.

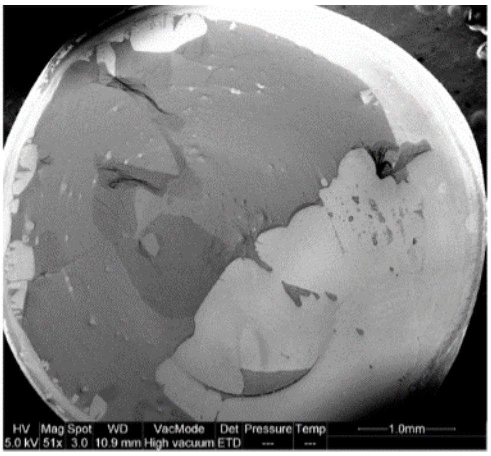

Fig. B3 SEM image of a Nafion–coated Pt (111) surface after the electrochemical measurement where the Nafion film was not heat-treated after the drying process.

B.4. Hanging meniscus configuration

Fig. B4 shows the SEM images of a Nafion–coated Pt (111) surface (a) before and (b) after the procedure for assembling an embedded form of RDE, not HM-RDE. Several parts of the Nafion film were scraped after the assembling procedure, where the Nafion-coated surface is placed face down and pressed on a polypropylene film (Fig. 2.2.4) [2].

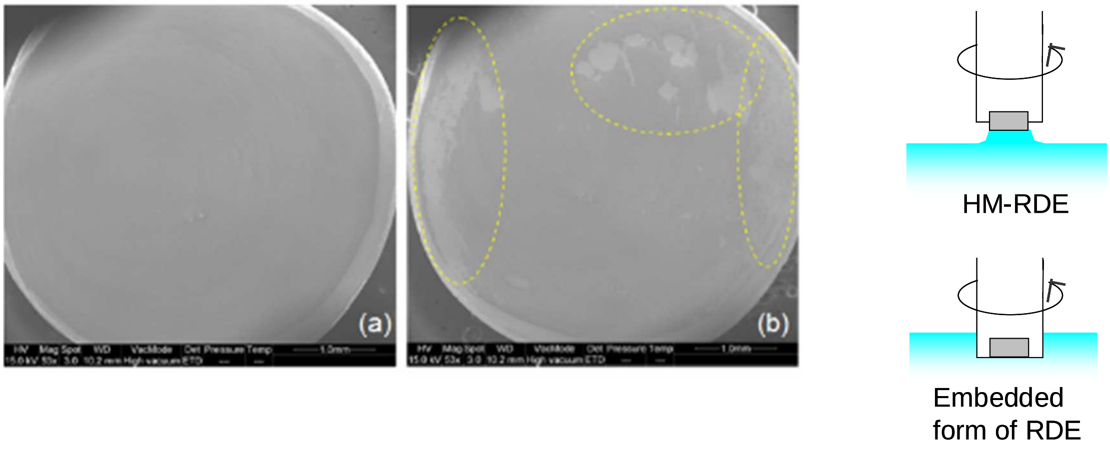

Fig. B4 SEM images of a Nafion–coated Pt (111) surface (a) before and (b) after the procedure for assembling an embedded form of RDE. The scraped parts are seen in the dashed circles. (10μL dropping of 0.005 wt % Nafion solutions.)

B.5 Amount of Nafion

The Nafion film is reproducibly extended to the almost entire region of the electrode surface when the dropping amount of the 0.005 wt % Nafion solution is 20 μL.

B.6 HER cleaning

Fig. B5 shows the CVs of the Nafion-coated Pt (111) surface before and after the electrochemical cleaning with hydrogen evolution reaction (HER) described in Section 5.1.1. The shape of H_{upd} peak before the cleaning is far from that for a clean Pt (111) and thus, the surface is seriously contaminated. With the HER cleaning, H_{upd} peak recovers and thus the contamination can be removed.

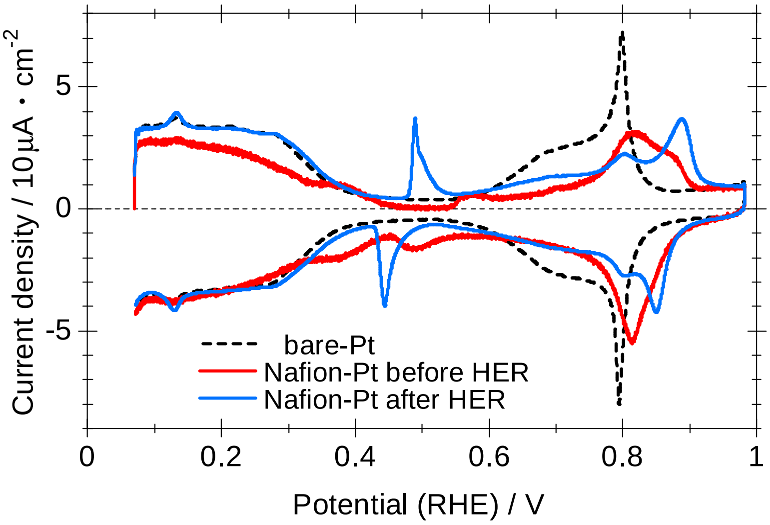

Fig. B5 CVs of the Nafion-coated Pt (111) surface before (red solid) and after (blue solid) the HER cleaning. CV of a bare-Pt (111) surface is also shown for comparison.

References

[1] N. Markovic, H. Gasteiger, P.N. Ross, *J. Electrochem. Soc.*, **144** (1997) 1591 .

[2] N.M. Markovic, H.A. Gasteiger, P.N. Ross, *J. Phys. Chem.*, **99** (1995) 3411 .

Acknowledgements

I appreciate Prof. Osawa in Hokkaido University advising me in various stages in summarizing my works as the Ph.D thesis and supervising the work with the surface enhanced infrared spectroscopy.

I would like to thank to Dr. Markovic in Argonne National laboratory leading me to learn electrochemical method with the highest quality in this field and supervising all my works in ANL. Dr. Strmknick, the group member in Argonne, concretely taught me techniques for the experiments using Pt single crystals and how to design effective electrochemical measurements. I would like to thank to Dr. Stamenkovic, technical leader in Argonne, kindly coaching me for my works in Argonne.

I am grateful for Dr. Morimoto in Toyota Central R&D Labs. Inc. because my foundation as an engineer was built by his coaching. I would also like to thank to Mr. Hatanaka managing and supporting my works for fuel cells in the company. Dr. Jinnouchi discussed the results and coached me for the theoretical parts of the thesis. Dr. Shinohara synthesized the new ionomer and discussed the results. I thank to Mr. Suzuki, Dr. Murata, Dr. Hasegawa and Dr. Takeuchi for their managing and supporting my works in TCRDL.

Dr. Motobayashi, the assistant Professor in Hokkaido Univ. taught me detailed procedures for the SEIRAS experiments, discussed the results, and looked after me during my staying in Hokkaido.

I am grateful my family for their great support.

This work was financially supported by NEDO (New Energy and Industrial Technology Development Organization), University of Chicago, Argonne, U.S. Department of Energy and Toyota Central R&D Labs.